INTEGRATION AND CHARACTERIZATION OF MICROMACHINED OPTICAL MICROPHONES

A Thesis
Presented to
The Academic Faculty

by

Mohammad Kamran Jeelani

In Partial Fulfillment
of the Requirements for the Degree
Master of Science in the
School of Mechanical Engineering

Georgia Institute of Technology
December 2009

INTEGRATION AND CHARACTERIZATION OF MICROMACHINED OPTICAL MICROPHONES

Approved by:

Dr. Levent Degertekin, Advisor
School of Mechanical Engineering
Georgia Institute of Technology

Dr. Peter Hesketh
School of Mechanical Engineering
Georgia Institute of Technology

Dr. Daniel Baldwin
School of Mechanical Engineering
Georgia Institute of Technology

Date Approved: November 10th, 2009

ACKNOWLEDGEMENTS

I would like to express my sincere gratitude to everyone who contributed to the following work. My time at Georgia Tech has been a learning experience in many ways, and I am fortunate to have had the opportunity to be a part of this world-class institution. It was a privilege to work under the direction Dr. Levent Degertekin and I am thankful for his guidance and support throughout this exciting project. Aside from serving on my Thesis Reading Committee, Dr. Peter Hesketh and Dr. Daniel Baldwin also deserve recognition for their contributions. I learned a great deal from Dr. Hesketh through his courses in MEMS, and Dr. Baldwin served as a consultant during the initial phase of this project.

The work presented in this thesis was funded by the National Institutes of Health (NIH) and is part of a joint effort by research teams at Georgia Tech, SUNY Binghamton, and The University of Illinois at Urbana-Champaign (UIUC). Special thanks are due to the members of the Microacoustic Sensors Laboratory at Binghamton University, led by Dr. Ron Miles. Dr. Miles' innovative work on directional biomimetic MEMS microphones provided the basis for this project, and his research team has been a valuable partner throughout the project.

I have truly enjoyed being a part of the MiST research group. It was a pleasure interacting with such a talented and friendly group of people. Dr. Neal Hall was a particularly vital resource throughout all stages of the project. He was directly involved in the development of the prototype test bed presented in Chapter 2, and the simulated optical intensity profiles presented in Chapter 3 are based on software which he

developed. Baris Bicen was also a valuable research partner, contributing a great deal of time to the characterization experiments detailed in Chapters 2 and 5. The miniature photodiode arrays implemented in this work were designed to specification by Shakeel Qureshi, and these devices proved to be extremely reliable constituents of the integrated hearing aid microphone. Recognition is also due to Caesar Garcia and Dr. Wook Lee, both of whom I enjoyed working with as part of the Microphone Team.

My immediate family has provided me with immeasurable support throughout my life. Above all, I must thank my parents Dr. Shaik Jeelani and Mrs. Ruqia Jeelani. My father's life story is an inspirational example of hard work and dedication, and my mother's love and support stands unwavering. Finally I thank my wife Lindy, whose impact on my life cannot be expressed in words.

TABLE OF CONTENTS

LIST OF TABLES

LIST OF FIGURES

SUMMARY

The focus of this study is the optoelectronic integration of a micro-optical displacement detection architecture with a biomimetic MEMS microphone membrane based on the directional hearing mechanism of the parasitic fly Ormia Ochracea. The micromachined microphones feature optical interferometric displacement detection achieved using a commercially available Vertical Cavity Surface Emitting Laser (VCSEL) coupled with a custom designed silicon photodiode array. This design is shown to have significant advantages over conventional hearing aid microphones, which employ capacitive detection.

A Multi-Chip Module (MCM) optoelectronic package is designed to integrate the biomimetic membrane with the optical displacement detection electronics in order to produce a fully integrated acoustic sensor. The modular package components, which are fabricated using high resolution stereolithography apparatus (SLA) equipment, provide accurate optical alignment of the optoelectronic components and allow complete device integration in a package with a total volume under 0.5cc.

Characterization of the integrated microphones is described in detail, including measurements of sensitivity, noise floor and directivity. A displacement resolution of 3.5×10^{-13} m/$\sqrt{\text{Hz}}$ was measured between 4kHz and 16kHz in an anechoic test chamber, corresponding to a dynamic range of 115dB for the optical detection architecture. The total noise SPL of the device is 35.9dBA. Unlike capacitive microphones with similar noise levels, the device developed in this work exhibits first order dipole directivity patterns between 250Hz-1kHz, with an ideal Directivity Index of 4.8dB @ 1kHz and

directional attenuation exceeding 25dB. With these results the optoelectronic package presented in this work demonstrates the viability of the integrated optical biomimetic microphones in compact, low power applications, specifically directional hearing aids.

CHAPTER 1

INTRODUCTION

An estimated 31.5 million people in the United States suffered from hearing loss in 2004, only 11.1 million of whom used hearing aids. An additional 1.4 million hearing impaired individuals owned a hearing aid but did not use it [1]. Among the factors influencing this trend are the limitations in conventional hearing aid microphone technology, which is currently dominated by capacitive microphones. Conflicting design parameters render capacitive microphones unfavorable for miniaturization, which is the dominant trend in hearing aid instruments [2].

Noisy environments are particularly challenging for hearing aid microphones [3, 4]. A study published in 2005 reported that only 51% of hearing aid users were satisfied with the performance of their hearing instruments in noisy environments [5]. In such situations, it is desirable for the microphone to exhibit a directional response in order to cancel unwanted background noise. Techniques exist for realizing a directional response using conventional capacitive membrane structures. While a variety of directional response patterns can be achieved using these techniques, the sensitivity and SNR of the device are necessarily sacrificed in the process.

The challenges associated with conventional hearing aid technology demonstrate the need for a highly sensitive miniaturized directional microphone with a low internal noise level. Optical interferometric displacement detection is a proven method which has the potential to replace capacitive displacement detection in a variety of applications. The following work demonstrates the viability and advantages of optical detection in

directional hearing aid microphones. The focus of this study is the integration of a micro-optical detection architecture with a novel biomimetic directional MEMS microphone membrane in order to realize a highly sensitive directional hearing aid microphone with low internal noise.

Capacitive MEMS Hearing Aid Microphones

A capacitive microphone is essentially a parallel plate capacitor in which one of the plates is a compliant membrane designed to undergo displacement as a result of acoustic pressure. The compliant membrane is separated from a conductive backplate electrode by a gap g. The capacitance is given by

$$C = \frac{\varepsilon A}{g} \tag{1.1}$$

where A is the area of overlap between the plates and ε is the permittivity of the medium between them. The dependence of the capacitance on the gap g is the basis of the transduction mechanism. Operation of the device requires a constant charge Q maintained by the application of a bias voltage V across the terminals of the device. The behavior of this system is governed by the static equation

$$Q = CV\ . \tag{1.2}$$

The following relation can then be derived from equations 1.1 and 1.2.

$$\Delta V = \frac{Q}{\Delta C} = \frac{Q\Delta g}{\varepsilon A} \tag{1.3}$$

From this simplified analysis it can be seen that a change in the gap g results in a corresponding change in the voltage at the terminals [6,7].

Integrated Circuit fabrication technology has yielded techniques which enable the fabrication of electronic devices with minimum feature sizes on the order of 100nm. This

has allowed for the miniaturization of a variety of sensors and transducers, including microphones. Microscale electromechanical devices which are fabricated using IC fabrication techniques are known as Microelectromechanical Systems (MEMS). The process of fabricating these devices, often referred to as micromachining, allows for the construction of electromechanical devices in the sub-millimeter range [8]. These exacting tolerances, combined with the ability to integrate directly with signal processing electronics, are driving interest in MEMS microphones [6]. Batch fabrication and tight control over processing parameters offer high yields. As result, MEMS technology has the potential to reduce not only the size but also the fabrication cost for a wide array of products. Capacitive devices currently dominate the MEMS microphone market, which includes consumer devices such as cellular phones and hearing aids.

Limitations of Capacitive Detection

The design of MEMS capacitive microphones is complicated by several conflicting design factors [9, 10]. Capacitive detection does not scale well for miniaturization as the active capacitance of the device is proportional to the surface area of the membrane. Capacitive sensitivity is also proportional to bias voltage and inversely proportional to gap height. These conditions are in conflict, however, as a high bias voltage leads to collapse of the membrane due to electrostatic pull-in, which occurs when the membrane is displaced by 1/3 of the gap. This phenomenon is better understood through a static analysis of the parallel plate model of a capacitor, illustrated in figure1.1.

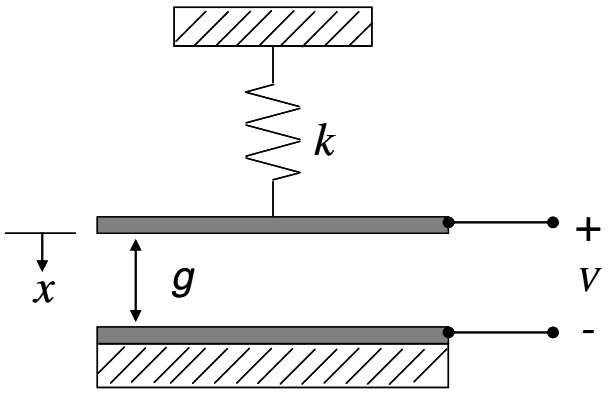

Figure 1.1 Parallel plate capacitor model

The compliant microphone membrane is represented by the top plate of the capacitor with a linear spring constant *k*. *V* is the voltage across the plates of the capacitor, and *x* is the displacement of the top plate. Voltage applied across the terminals results in an attractive electrostatic force between the plates given by

$$F_{es} = \frac{\varepsilon A V^2}{2g^2} \tag{1.4}$$

where A is the area over which the plates overlap. This force results in a displacement *x* of the top plate. This displacement in turn results in a reactive elastic force given by

$$F_k = kx = k(g_0 - g) \tag{1.5}$$

where g_0 is the initial gap. As *g* is reduced due to the application of increasing voltage, the magnitude of the elastic force increases linearly, while the electrostatic force is inversely proportional to g^2. At a certain voltage the electrostatic force overcomes the elastic force, leading to the collapse of the membrane onto the backplate. This phenomenon is known as pull-in. The pull-in voltage is defined as the point when the net force on the top plate is 0, as given by equation 1.6.

$$F_{net} = F_{es} - F_k = 0 \tag{1.6}$$

Substitution for F_{es} and F_k yields equation 1.7.

$$\frac{\varepsilon A V^2}{g^2} - k(g_0 - g) = 0 \tag{1.7}$$

Stability of the system below pull-in requires that

$$\frac{\delta F_{net}}{\delta g} \leq 0 . \tag{1.8}$$

Substitution for F_{net} leads to

$$\frac{\varepsilon A V^2}{g^3} - k \leq 0 \ . \tag{1.9}$$

Equations 1.7 and 1.9 can be solved simultaneously for g and V, which leads to the following expressions for the pull-in gap and voltage [11].

$$g_{PI} = \frac{2}{3} g_0 \tag{1.10}$$

$$V_{PI} = \sqrt{\frac{8 k g_0^3}{27 \varepsilon A}} \tag{1.11}$$

While sensitivity is maximized as g and V approach these values, operation of the device near collapse results in non-linear behavior and limited dynamic range.

Another issue of major concern in the design of capacitive microphones is the acoustic resistance of the backplate, which can result in high thermal noise levels associated with passive damping. As the gap is decreased, the rise in thermal noise exceeds the rise in sensitivity. This results in a fundamental limit on the SNR of capacitive MEMS microphones [6]. Backplates can be perforated in order to reduce

resistance, but this technique decreases sensitivity due to the decrease in effective sensing area.

Diffraction-Based Optical Microphones

The concept of an optical microphone has existed since at least 1881 when the Photopone was patented by A.G. Bell [12, 13]. Optical Interferometry is a widely used displacement detection technique which offers shot noise limited displacement resolution [14]. Micromachined diffraction-based optical microphones with a displacement resolution of 2.4x 10^{-12}m$\sqrt{\text{Hz}}$ have been demonstrated [15], however integration difficulties prove challenging for microscale implementation of this technique [12].

This work deals specifically with interferometric phase modulated optical microphones. This optical detection method implemented in these devices is based upon the phase sensitive diffraction grating, illustrated in figure 1.2.

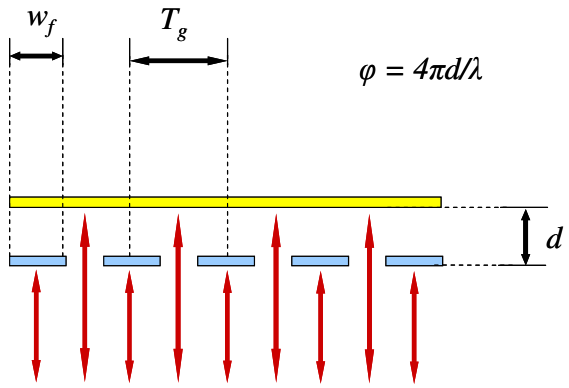

Figure 1.2 Phase sensitive diffraction grating

A periodic array of reflective fingers with period T_g is separated from a reflective surface by a distance d. The grating is illuminated from below using a coherent light source with a wavelength λ. Light that passes between the fingers is reflected by the top reflector and

travels an additional path length of $2d$, accruing a phase of $4\pi d/\lambda$ relative to the light that is reflected by the grating fingers. The superimposed fields interfere and result in the generation of an intensity field with spatially distributed reflected and diffracted orders, as illustrated in figure 1.3.

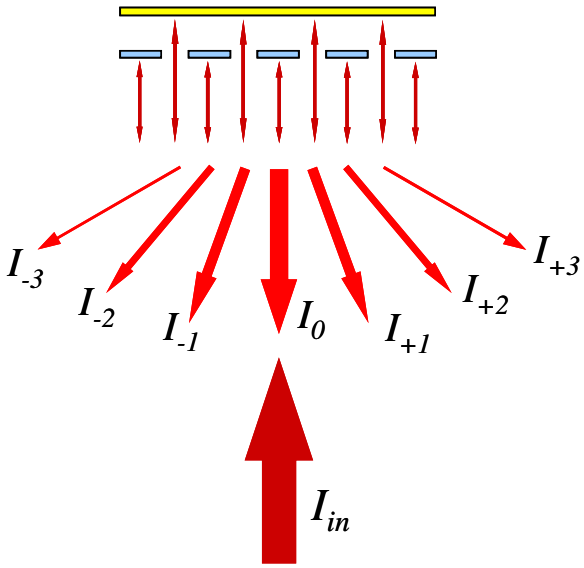

Figure 1.3 Diffraction pattern created by illumination of phase sensitive diffraction grating

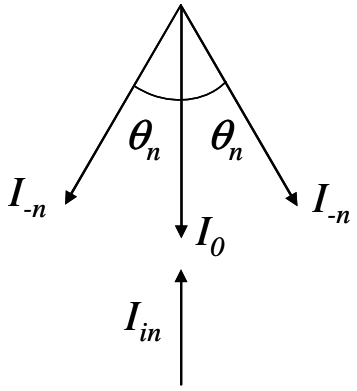

Figure 1.4 Geometry of diffracted orders

The far-field approximation for the angle θ_n between the incident beam and the nth diffracted order (figure 1.4) is given by

$$\theta_n = \sin^{-1}\left(\frac{n\lambda}{T_g}\right) \tag{1.12}$$

where n is the order number, T_g is the period of the diffraction grating, and λ is the wavelength of the incident light.

While the angles of the diffracted orders are constant for a given wavelength, the intensities of these beams vary as a function of d. This is the key to the interferometric displacement detection architecture. A change in the distance between the grating and reflector can be detected by measuring the intensities of the 0th or higher orders. The majority of the light power is returned in the 0th and ±1st orders, the intensities of which are approximated in the far field as

$$I_0 = I_{in}\cos^2\left(\frac{2\pi d}{\lambda}\right) \tag{1.13}$$

$$I_{\pm 1} = \frac{4}{\pi^2} I_{in}\sin^2\left(\frac{2\pi d}{\lambda}\right) \tag{1.14}$$

where I_{in} is the intensity of the incident light. Plotting these intensities as a function of d results in the optical intensity curves, shown in figure 1.5

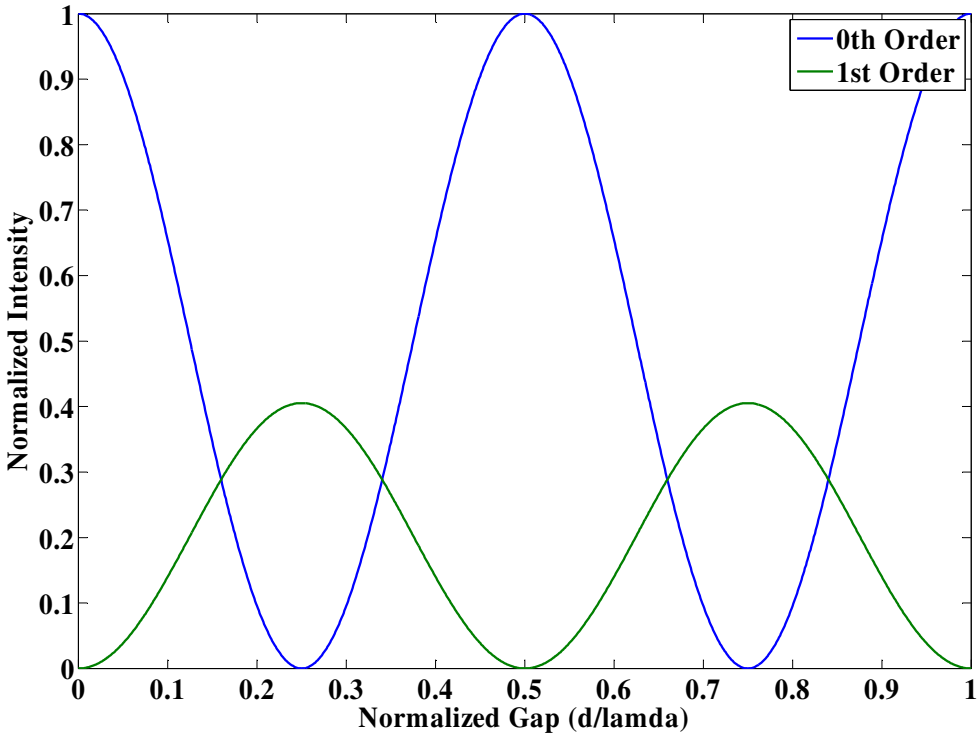

Figure 1.5 Ideal optical intensity curves

It is evident from these curves that there are multiple domains over which the intensity of the diffracted orders can be accurately approximated as a linear function of the displacement of the membrane.

The displacement sensitivity of the optical detection architecture is proportional to the first derivative of the optical intensity curve. The points of maximum sensitivity d_n are found at the zeroes of the second derivative, i.e. odd multiples of $\lambda/8$. This is expressed mathematically by equation 1.15.

$$d_n = \frac{\lambda}{8} + \frac{n\lambda}{4} \tag{1.15}$$

The intensities of the 0^{th} and 1^{st} orders are typically measured using photodiodes. These semiconductor devices transduce the light intensity into an electrical current which in

turn is converted to a voltage signal using a transimpedance amplifier(TIA). The maximum electrical sensitivity of the device can be approximated using a two-term Taylor expansion about d_n [16]. The resulting electrical sensitivity is given by

$$S_e = \frac{2\pi V_{pp}}{\lambda} \tag{1.16}$$

where *Vpp* is the peak to peak amplitude of the amplified optical intensity curve in units of volts and λ is the wavelength of the incident light. This yields an electrical sensitivity value with units of V/μm. The total sensitivity of the device in units of V/Pa is then given by

$$S = S_e X S_m \tag{1.17}$$

where S_m is the mechanical sensitivity of the membrane, which is equivalent to its compliance.

The upper limit of the dynamic range of the device is given by inspection of the optical intensity curve. When the device is operated at an initial gap given by one of the points d_n, the absolute maximum peak to peak displacement that can be measured without clipping is $\lambda/4$, where λ is the optical wavelength of the light. The miniature light sources implemented in this work have an optical wavelength of 850nm, which results in a maximum linear displacement of 212.5nm. The lower end of the dynamic range is theoretically limited by shot noise, the calculation of which is detailed in Chapter 5.

Directional Hearing Aid Microphones

The directivity of a microphone refers to the acoustic response of the device as a function of angle of incidence of sound waves. Conventional capacitive microphone diaphragms measure scalar acoustic pressures. These devices are therefore

omnidirectional, responding equally regardless of the direction of the acoustic source. In hearing aid applications it is advantageous to for the microphone to exhibit a directional response in order to ignore unwanted background noise. Directional microphones have been available for use in hearing aids since at least the early 1970s [17].

A directional response in hearing aid microphones is conventionally achieved in one of two ways [18]. One of these is the two-port microphone, in which the acoustic pressures from the two ports act on opposite sides of a membrane, resulting in a net deflection of the membrane. Capacitive detection of this deflection yields an electrical signal that represents the difference in pressures between the two ports. A fixed acoustic filter built into the device is used to tune the delay between the two signals in order to obtain the desired directional response [6, 17].

Another way in which a directional microphone can be realized is by differencing the output signals from two adjacent omnidirectional microphones. In this case the phase-shifting filter is applied in the electrical domain. The characteristics of this filter can be controlled by DSP circuitry in order to obtain different directional patterns. Implementation of this technique in hearing aid microphones allows selection of multiple preset patterns by the user or DSP program based on the environment. This idea can be extended to actively adapt the directional pattern in order to maximize the SNR in a changing environment [17].

While both of these methods produce a directional response, the sensitivity of the device is sacrificed in the differencing process. This effectively reduces the SNR of the device, especially at low frequencies [6, 17]. This poses a significant design challenge for directional microphone arrays.

SUNY Biomimetic Directional MEMS Microphone

A promising alternative to conventional directional microphones is suggested by nature in the directional hearing system of the parasitic fly Ormia Ochracea. Spatial source localization by biological organisms is typically accomplished by sensing minute differences in the intensity and arrival time of acoustic signals as measured by two distinct tympana, or eardrums. For large animals, the distance between the mechanically decoupled ears is significant compared to the wavelength of the acoustic signal, and the interaural time and intensity variations can be measured by the central nervous system. In smaller animals, however, the interaural time and intensity variations between the ears are extremely small. In the case of Ormia Ochracea, the tympana are only 500μm apart. This results in an interaural time of less than 2μs, which is insufficient for neural encoding of the directional information. Ormia is able to localize sources due to the mechanical coupling of its tympana by a cuticular membrane, illustrated in figure 1.6 [19].

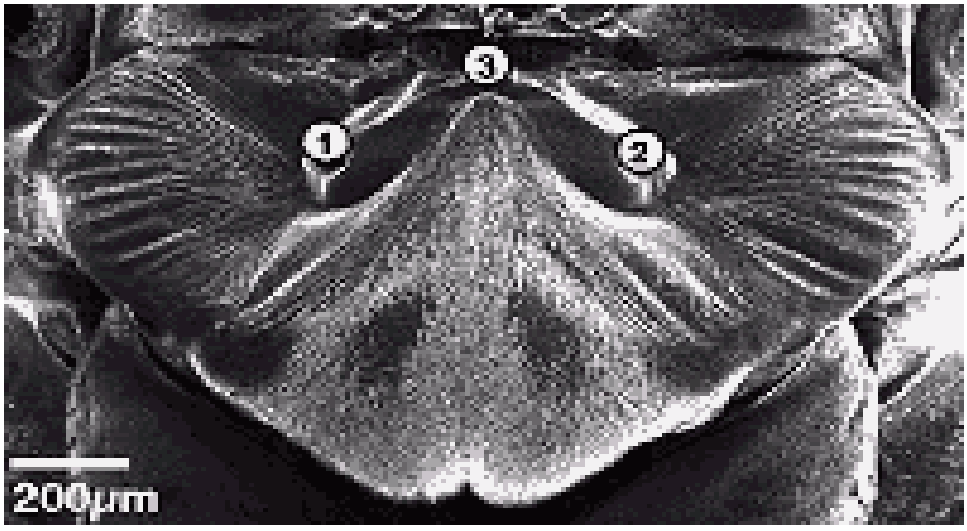

Figure 1.6 Mechanically coupled tympana of Ormia Ochracea [19]

The directional response of this unique mechanism has been mimicked in order to develop a directional MEMS microphone membrane which consists of a single moving element, as illustrated in figure1.7

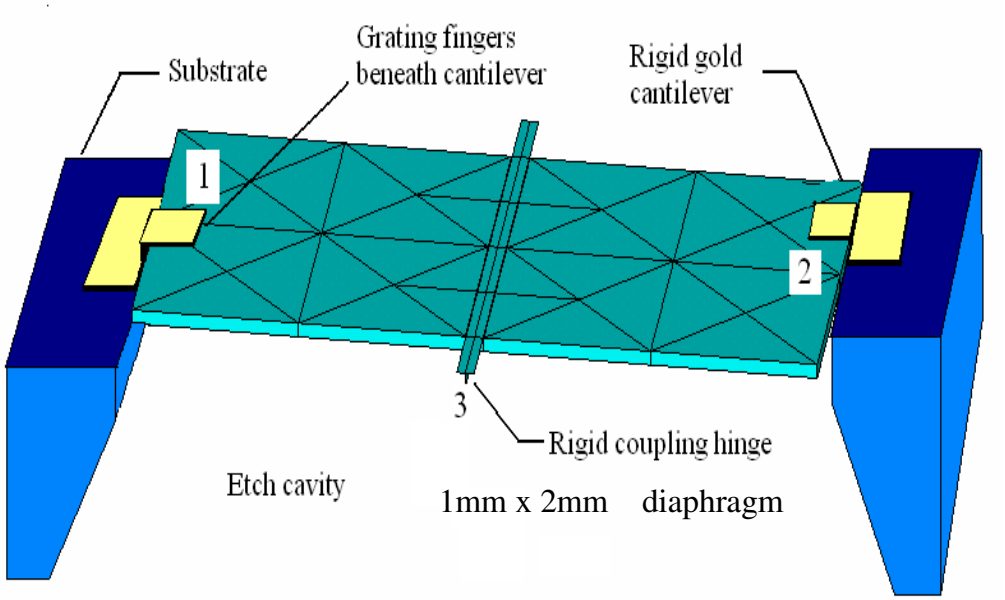

Figure 1.7 Biomimetic MEMS microphone membrane

This biomimetic membrane consists of a 1mm x 2mm diaphragm with a centrally located hinge, mimicking the coupled tympana of Ormia Orchacea. Reinforcement ribs add stiffness to the diaphragm, increasing the stiffness to mass ratio and effectively attenuating unwanted resonant modes [20].

Displacement detection is achieved by implementation of the optical diffraction-based detection architecture described previously. Rigid gold cantilevers anchored to the substrate serve as reflectors. These gold reflectors are suspended over optical gratings etched into the membrane, shown in figure 1.8.

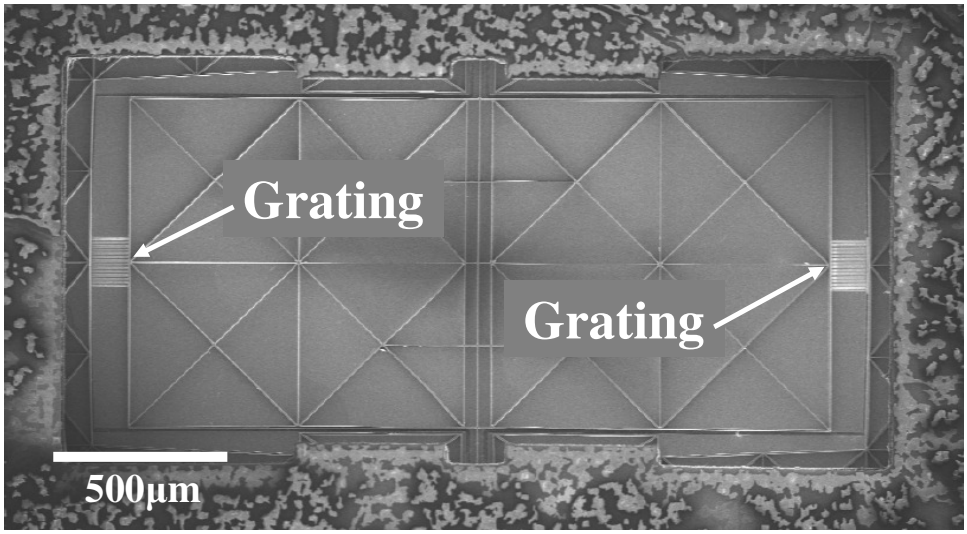

Figure 1.8 Scanning Electron Micrograph of underside of biomimetic membrane

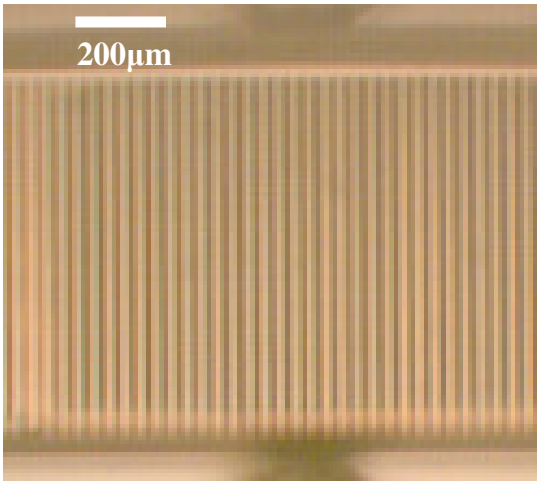

Figure 1.9 Image of grating fingers

The grating fingers, shown in figure 1.9, measure 100µm long by 2µm wide and are spaced at a fixed period of 4µm. Note that the finger width is half of the grating period. An interesting artifact of this particular geometry is the elimination of the higher even orders in the diffraction pattern [14]. This situation is illustrated schematically in figure1.10.

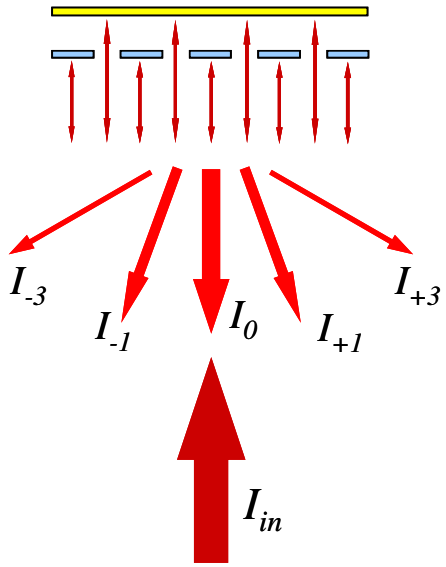

Figure 1.10 Diffraction pattern with suppressed higher even orders

The gratings are located at the ends of the membrane because these points undergo maximum deflection for a given pressure gradient. Measuring the displacement at these locations thereby results in greater displacement sensitivity. The devices are batch fabricated in dies, each which contains two of the biomimetic membranes along with an omnidirectional membrane. A fabricated die is shown in figure 1.11

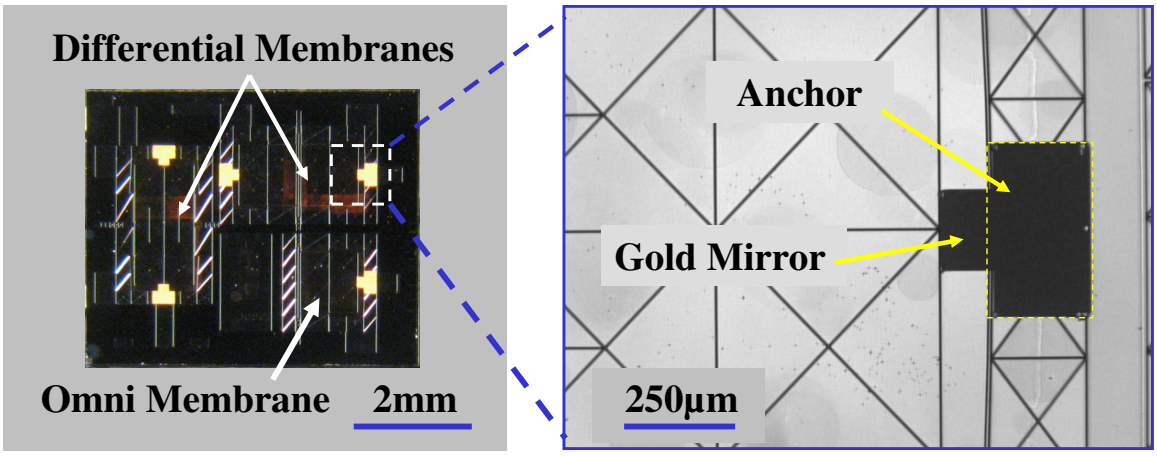

Figure 1.11 Biomimetic MEMS microphone membrane chip

The devices are oriented in this manner for the purpose of developing advanced signal processing algorithms as detailed in [21].

Electrostatic Actuation

The biomimetic SUNY device features electrostatic actuation capabilities which are decoupled from the detection optics. This makes it possible to tune the initial displacement of the membrane in order to maximize sensitivity (and hence the SNR). The initial deflection of the membrane can be adjusted by applying a bias voltage across the membrane and mirror, both of which are conductive. The resulting electrostatic force was quantified as a function of bias voltage in equation1.4. Using this capability, the initial deflection of the membrane is set to one of the maximum sensitivity points given by equation 1.15.

Fabrication of SUNY Biomimetic Microphone Membrane

An overview of the fabrication of the SUNY membrane is instructive in understanding the design and operation of the device. A schematic illustration of the fabrication process flow is shown in figure1.12 [20].

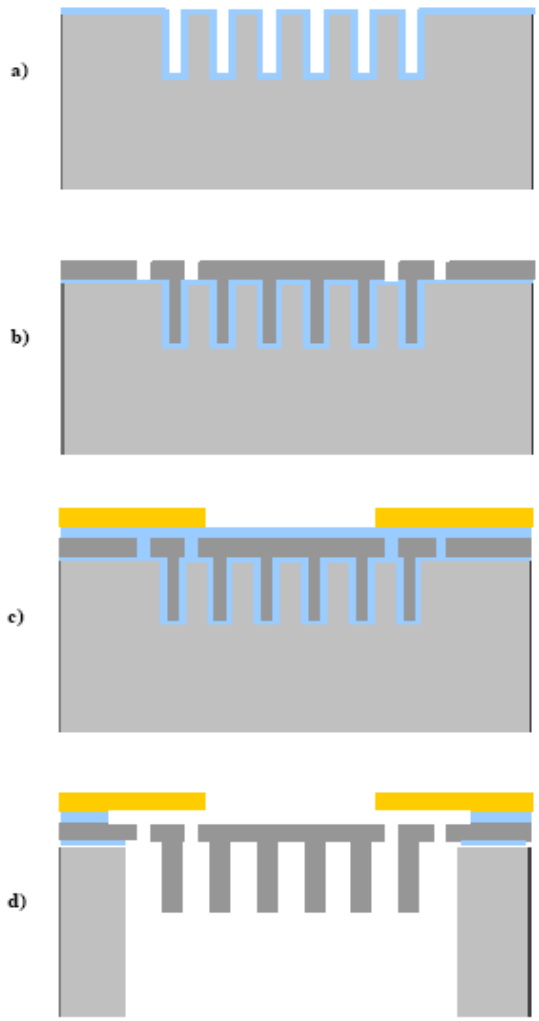

Figure 1.12 Fabrication process flow for biomimetic MEMS microphone membrane [20]

The first step in the process is a reactive ion etch (RIE) which creates trenches in the 4" silicon wafer. These trenches serve as a mold for the membrane stiffeners. The RIE etch is followed by the deposition of a 1μm thick oxide layer which serves as an etch stop for a subsequent backside RIE. The oxide layer is colored blue in figure 1.12a. Polycrystalline silicon is deposited to fill the trenches and form a 1μm thick layer on the surface. The poly-silicon layer is then etched to define the outline of the membrane and create the optical grating as illustrated in figure 1.12b. A second oxide layer is deposited

to a thickness of 5μm. This serves as a sacrificial layer that defines the spacing between the mirror and the membrane. A chrome and gold seed layer is deposited via evaporation, followed by the plating of a 5μm thick gold layer. The gold layer is patterned to form the gold mirrors suspended above the gratings (figure 1.12c). A deep reactive ion etch (DRIE) is then performed to create the backside cavity beneath the membrane. Finally, the oxide layers are etched in order to release the membrane and mirror structures, as shown in figure 1.12d [20].

Quantifying Microphone Directivity

An established standard for measuring the directional response of a microphone is the *free field method* [22, 23]. The microphone is placed in a free field and its response to a moving acoustic source is measured at discrete intervals. The source is rotated in a spherical pattern with constant radius in the far field of the microphone.

In hearing aid applications it is commonly assumed that the device under test exhibits a symmetrical response in a particular plane. If this is assumed, the acoustic source need only be rotated in a circular pattern about the device under test in order to measure directivity in the plane of interest. The response of the microphone to the fixed frequency acoustic source is plotted vs. angle of incidence in a polar plot know as a Spatial Directivity Pattern (SDP) [22]. The directional biomimetic membrane is intended to perform as a first order dipole. The SDP for this type of device follows the form of $\text{Cos}(\theta)$ [7], as illustrated in figure 1.13.

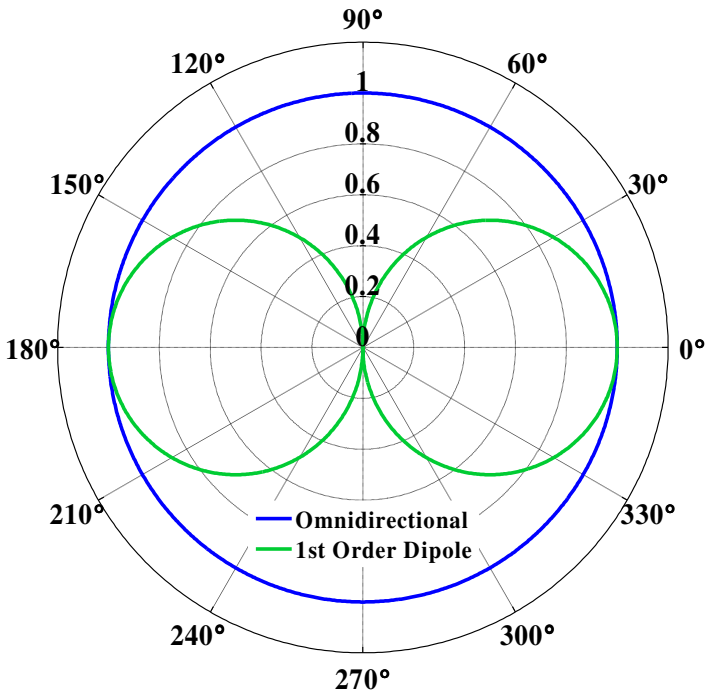

Figure 1.13 Ideal linear Spatial Directivity Patterns

Also shown in this figure is the SPD for an omnidirectional microphone, the response of which is independent of the angle of incidence of the measured acoustic signal.

A standard metric for quantifying the directional attenuation capabilities of a microphone is the Directivity Index (DI), defined as

$$DI(f) = 10Log_{10}\left[\frac{4\pi|p_{ax}|^2}{\int_0^{2\pi}\int_0^{\pi}|p(\varphi,\theta)|^2|\sin(\varphi)|d\varphi d\theta}\right] \tag{1.18}$$

where p_{ax} is the on-axis sound pressure response of the microphone and $p(\varphi,\theta)$ is the pressure response to a diffuse sound field as a function of angle of incidence [22, 24]. The variables φ and θ are angular measurements relative to the sensitive axis in the planes of interest of the microphone. These should not be confused with the phase and diffraction angles associated with the phase sensitive diffraction grating presented

previously. The quantity within the brackets of the logarithm is referred to as the directivity factor Q. For discrete data measurements of $p(\varphi,\theta)$, the integrals in the denominator of Q become summations and the DI is calculated as

$$DI(f) = 10Log_{10}\left[\frac{4\pi|p_{ax}|^2}{\sum_{m=1}^{2\pi/\Delta\theta}\sum_{n=1}^{\pi/\Delta\theta}|p(\varphi_n,\theta_m)|^2|\sin\varphi|\Delta\varphi\Delta\theta}\right] \tag{1.19}$$

where $\Delta\theta$ and $\Delta\varphi$ are the angular increments between measurements taken at points (r,φ_n, θ_m) and r is a fixed radius in the far field of the microphone. Symmetry is often assumed in one of the planes of the microphone, in which case equation1.19 is reduced accordingly.

The DI for an omnidirectional microphone is 0dB, indicating that the response of the device is independent of angle of incidence. The DI for an ideal dipole is 4.8dB. Detailed measurements of the integrated SUNY microphone's directional response are presented in Chapter 5.

The Challenge

The challenge addressed in this work is the fusion of the directional biomimetic membrane with the diffraction-based optical detection technique in order to produce a low noise direction hearing aid microphone with significant advantages over conventional capacitive hearing aid devices. A robust package is designed and implemented to integrate these technologies in a minimal footprint that can be easily implemented in a standard hearing aid form factor. The following chapters present

design, modeling and fabrication of the microphone packages, along with the integration and characterization of the biomimetic hearing aid microphone.

CHAPTER 2

INITIAL WORK: PROTOTYPE TEST BED

The diffraction-based optical displacement architecture requires a robust platform that provides optical alignment tolerances on the order of 10μm. Prior to designing the microscale package for the hearing aid microphone, a macroscale prototype test bed was designed and constructed in order to prove the validity of the optical detection technique and establish baseline performance metrics for the biomimetic microphone.

Design & Modeling of Prototype Test Bed

A 3D CAD model of the prototype test bed is shown in figure 2.1.

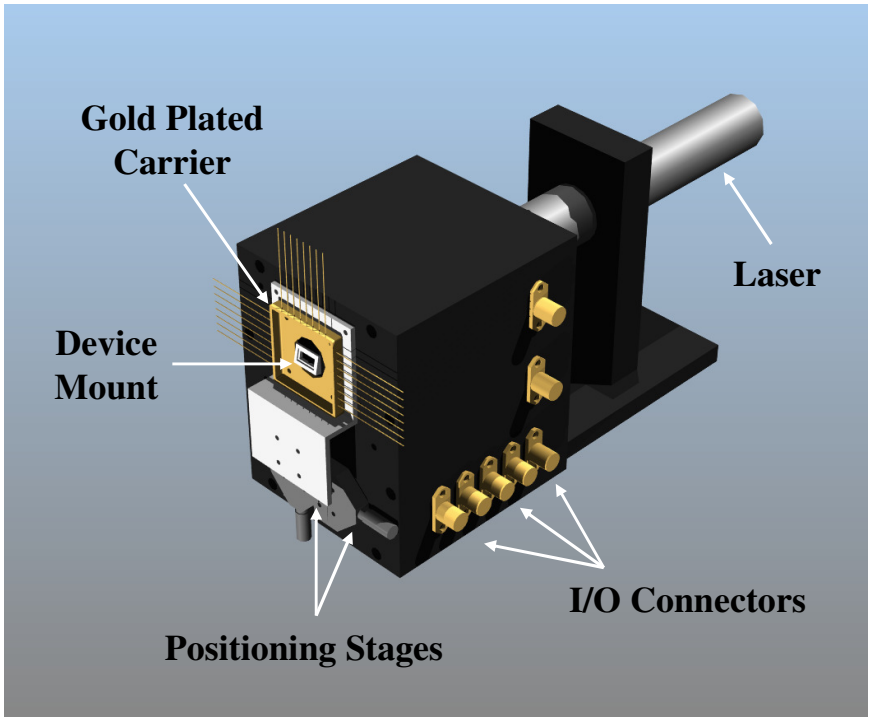

Figure 2.1 CAD model of prototype test bed

A 638nm laser diode with an output power of 5mW [25] is focused to a beam spot size of 50µm on the grating plane using a spherical lens mounted inside of the test bed, as illustrated in figure 2.2.

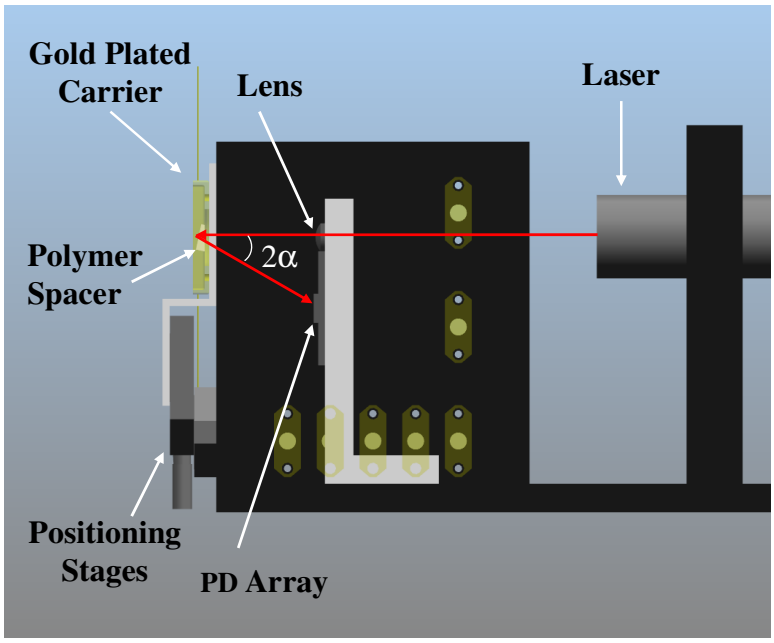

Figure 2.2 Side view of prototype test bed

The device under test is mounted to a gold-plated chip carrier via a custom fabricated polymer spacer. A glass slide suspends the spacer over an optical aperture drilled into the carrier. The chip carrier is mounted to a pair of positioning stages which proved the high level of alignment accuracy required to align the beam spot with the 100µm grating. The electrostatic actuation ports on the membrane are interfaced through I/O pins on the chip carrier. These pins are then connected to an SMA connector which can be interfaced by the test electronics.

The device under test is mounted to the test bed at an angle α in order to direct the diffracted beams onto a commercial photodiode array. The incidence of light on the

photodiodes induces photocurrents which are proportional to the intensities of the 0^{th} and $\pm 1^{st}$ orders. The architecture of the prototype test bed is further illustrated in the auxiliary view shown in figure 2.3.

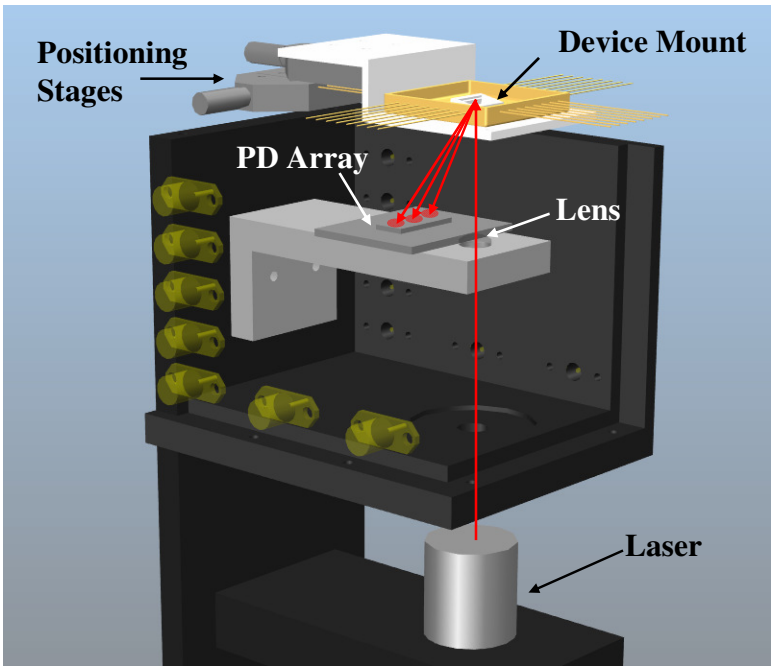

Figure 2.3 Auxiliary view of prototype test bed

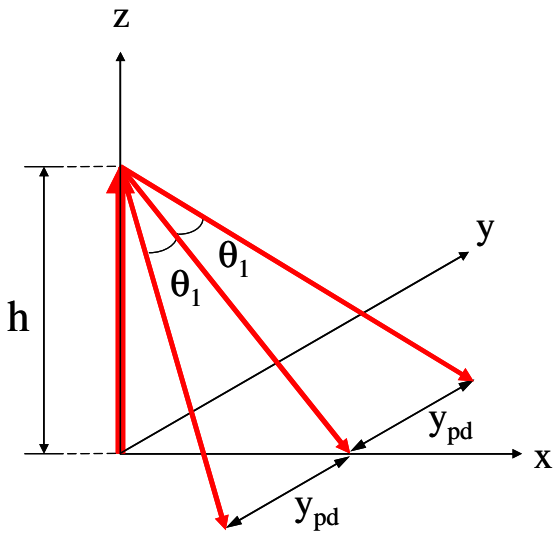

Figure 2.4 Optical beam geometry

The geometry of the optical beams is illustrated in figure 2.4. The XY plane represents the photodiode plane and *h* is the distance between the photodiode array and the microphone grating. The projection of the beam pattern on the XZ and YZ planes is shown in figure 2.5

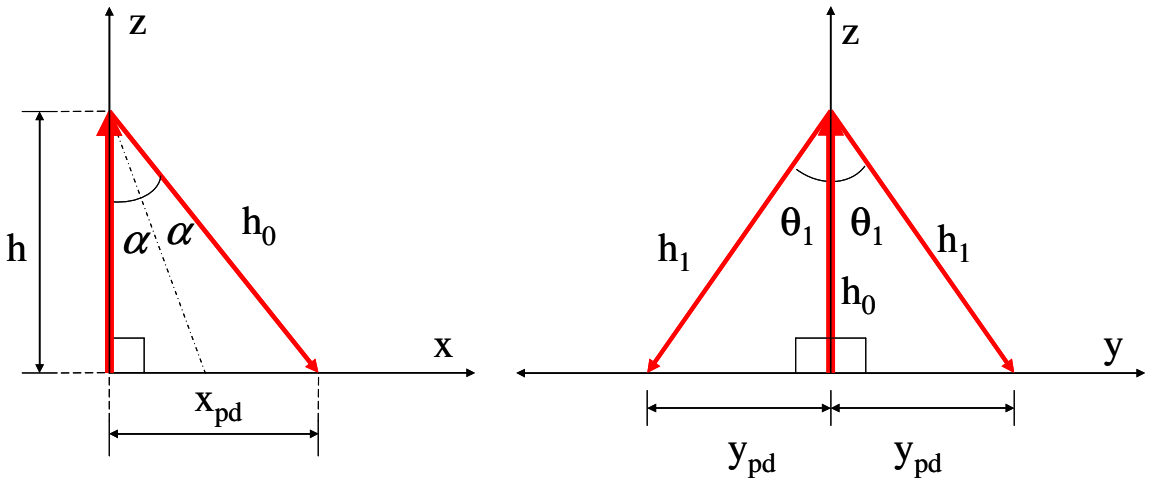

Figure 2.5 Geometry of projected beam patterns

The angle α is given by the tilt of the grating relative to the test bed. The x-location of the photodiode array is labeled x_{pd}. The distance between the projections of the 0th and ±1st orders on the photodiode plane is denoted by y_{pd}. θ_1 is calculated using equation 1.12. Expressions for x_{pd} and y_{pd} are then given by equations 2.1 and 2.2, respectively.

$$x_{pd} = h\tan(2\alpha) \tag{2.1}$$

$$y_{pd} = \frac{h\tan\left[\sin^{-1}\left(\frac{\lambda}{d}\right)\right]}{\cos(2\alpha)} \tag{2.2}$$

The values of λ and d are defined by the parameters of the laser and grating, respectively. The value of h is determined by the focal length of the lens. Minimization of the coupled variables α and x_{pd} is limited by the sum of the lens radius and the width of the photodiode array in the x direction. The value of y_{pd} is limited by the length and pitch of the photodiode array. These factors were used to define the exact dimensions of the prototype test bed. The fabricated test bed is shown in figure 2.6

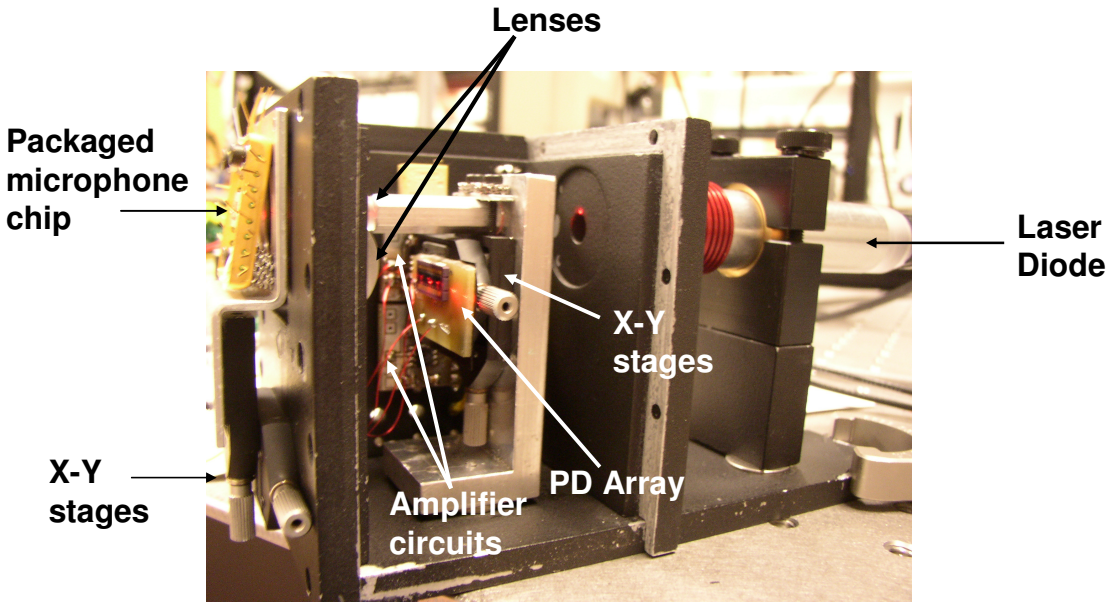

Figure 2.6 Fabricated prototype test bed

The photodiode array is mounted to a second pair of positioning stages which enable accurate alignment of the diffracted beams and the photodiode cells. A cylindrical lens is positioned between the diffraction grating and the photodiode array in order to focus the diffracted orders on the photodiode plane. The projection of the 0^{th} and $\pm 1^{st}$ order beams on the photodiode array can clearly be seen in figure 2.7

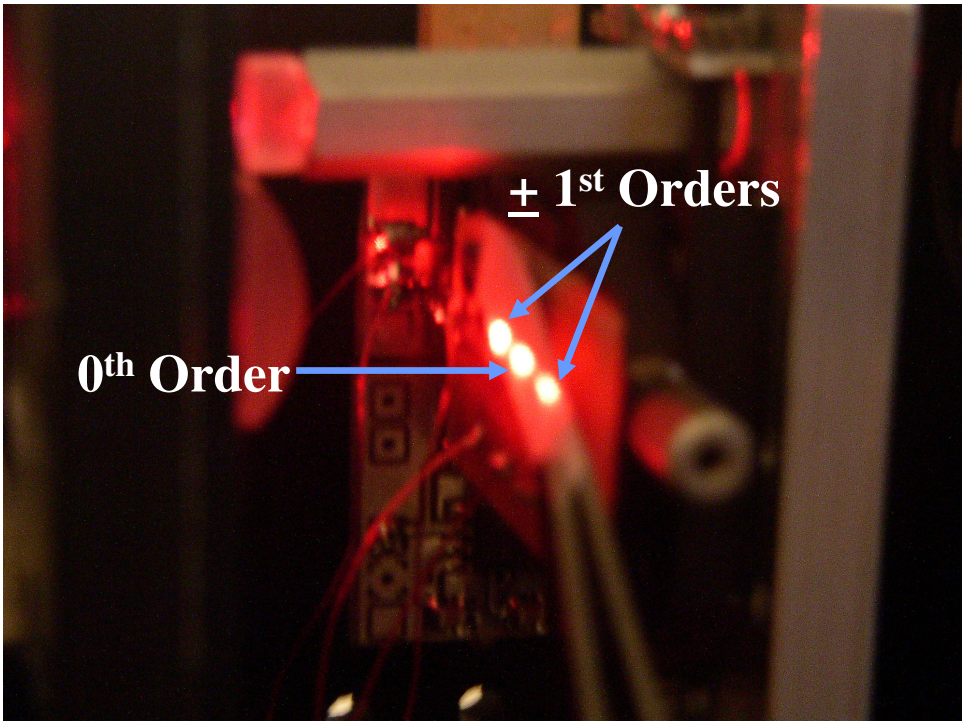

Figure 2.7 Diffraction pattern on photodiode plane

The test bed is equipped with dual Trans-Impedance Amplifiers (TIAs) which output voltages proportional to the photocurrents generated by the 0^{th} and 1^{st} order photodiodes. The gain of the TIAs can be adjusted by changing the resistance of potentiometers which serve as feedback resistors in the amplifier circuitry. 9V Batteries provide a clean power source for the TIAs. SMA connectors are used to interface the test bed electronics with external testing equipment. These connectors provide ports for the output signals, amplifier power, and electrostatic actuation of the membrane.

Initial Characterization of Biomimetic MEMS Microphone

The prototype test bed was used to perform initial characterization of the biomimetic microphone. Tests were conducted to measure the optical intensity curves,

frequency response, and noise floor. In order to minimize reflections and ambient noise, the acoustic tests were conducted inside an anechoic chamber which has a measured noise floor of 16dBA. This facility is part of the Integrated Acoustics Laboratory (IAL) at Georgia Tech. BNC Cables route the I/O signals between the prototype test bed and the test equipment located outside of the chamber. The performance measurements are presented in the following sections.

Optical Intensity Curves

The test setup for measurement of the optical intensity curves is illustrated in figure 2.8. A low frequency (10Hz) voltage ramp signal is applied to the electrostatic actuation ports using a function generator. The 0^{th} and 1^{st} order intensities resulting from the applied bias values are measured as a voltage signal at the output of the amplifier. The output signals are then graphed as a function of bias voltage in figure 2.9.

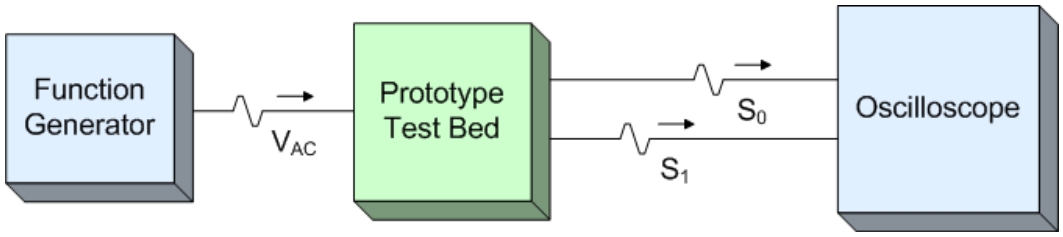

Figure 2.8 Test setup for measurement of optical intensity curves using prototype test bed

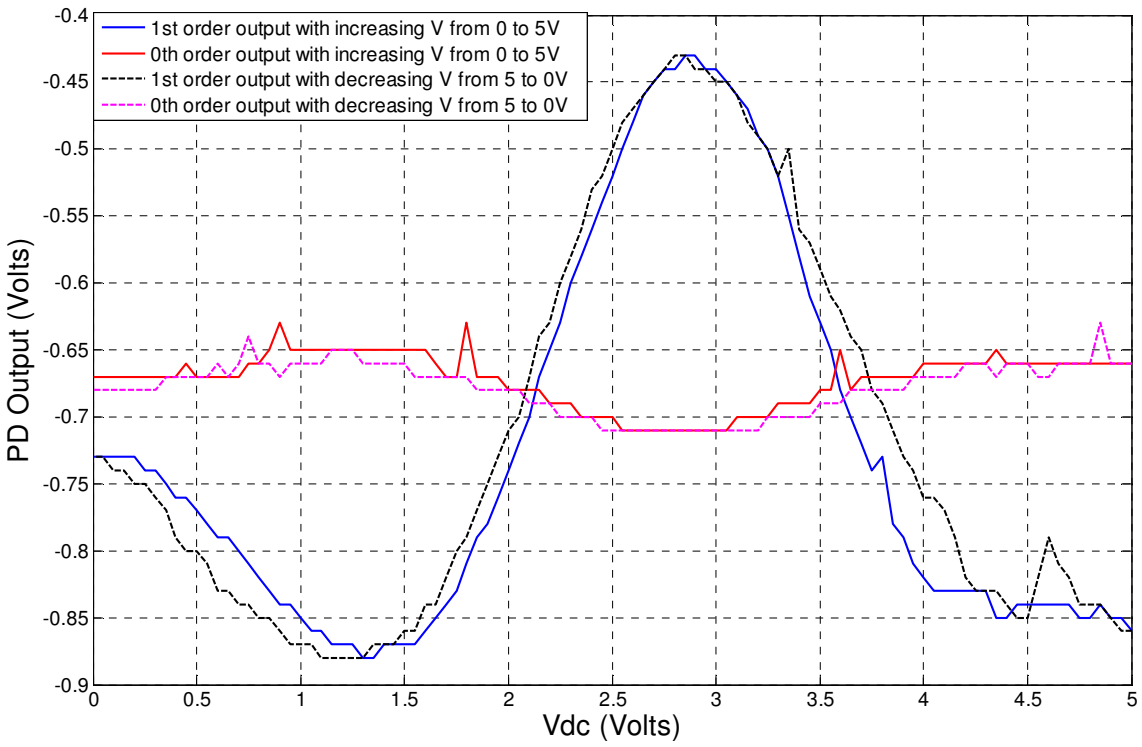

Figure2.9 Optical intensity curves measured using prototype test bed

The measured values are negative due to inversion of the signal by the TIA circuitry. The 0^{th} and 1^{st} order signals are out of phase as expected. The amplitude of the 0^{th} order is expected to be significantly larger that the 1^{st} order, as dictated by equations 1.13 and 1.14. This is not the case in the measured data because the 1^{st} order TIA was set to a significantly higher gain than the 0^{th} order TIA. The intensity curve data is used to calibrate the position of the membrane to the point of maximum sensitivity for subsequent measurements of frequency resoponse and noise floor. The maximum displacement sensitivity of the device is 4.5V/μm, as calculated from the 1^{st} order intensity curve using equation 1.16.

Frequency Response

The frequency response to both acoustic and electrostatic actuation was measured in an anechoic test chamber using the prototype test bed. The test setup for measurement of the electrostatic frequency response is illustrated in figure 2.10.

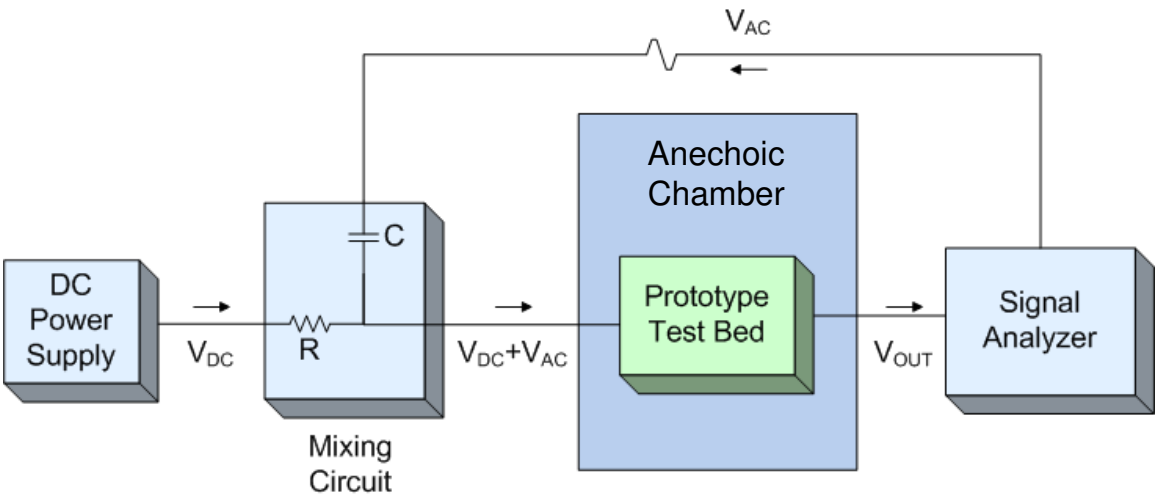

Figure 2.10 Test setup for measurement of electrostatic frequency response using prototype test bed

A chirp signal is generated using a Stanford Research Systems (SRS) SR785 dynamic signal analyzer. This signal is combined with the DC bias voltage using a mixing circuit. The combined signal is then applied to the electrostatic actuation ports on the microphone. The resulting microphone output signal is measured by the signal analyzer which calculates the frequency response, shown in figure 2.11.

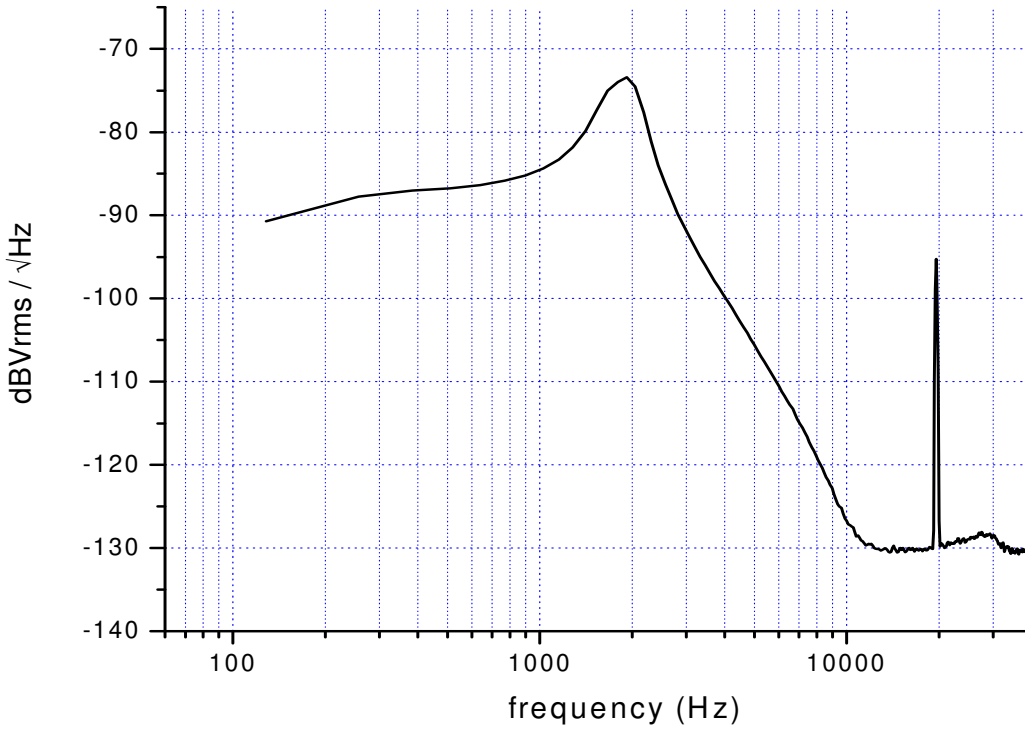

Figure 2.11 Electrostatic frequency response measured using prototype test bed

The rotational (rocking) mode resonance of the device can be seen just below 2kHz. The peak at 29kHz is the translational (flapping) mode resonance of this particular device. The sharp peak at 19.6kHz is unaccounted for by the dynamics of the membrane. Because this peak is also measured by a Larson Davis 2541 ½" calibration microphone, it was assumed to be the result of an external source in the environment.

The test setup for measurement of the acoustic frequency response is illustrated in figure 2.12.

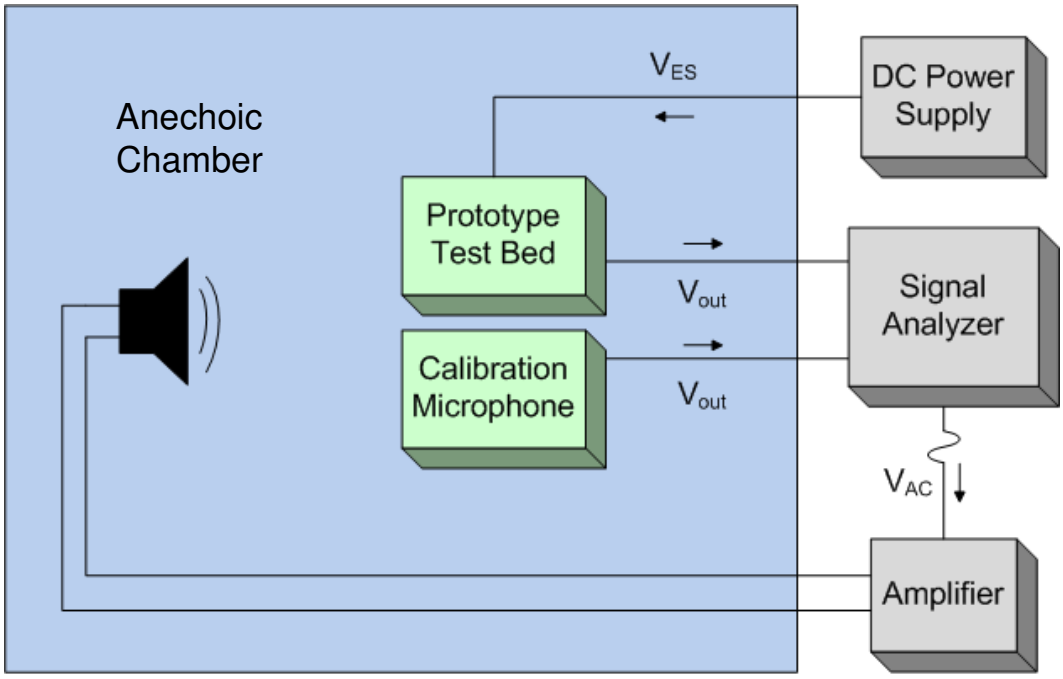

Figure 2.12 Test setup for measurement of acoustic frequency response using prototype test bed

A chirp signal is generated using the SRS dynamic signal analyzer. This signal is then amplified and fed to a Yamaha NS-6490 3-way speaker. A DC power supply is used to bias the membrane to the point of maximum sensitivity as determined from the optical intensity curves. The output of the microphone is recorded by the signal analyzer. A ½" Larson Davis model 2541 microphone, which has a relatively flat response and a known sensitivity of 0.04V/Pa, is used to measure the acoustic input signal. The data recorded by the prototype microphone is then divided by the Larson Davis calibration data in order to calculate the acoustic sensitivity in units of V/Pa, as shown in figure 2.13.

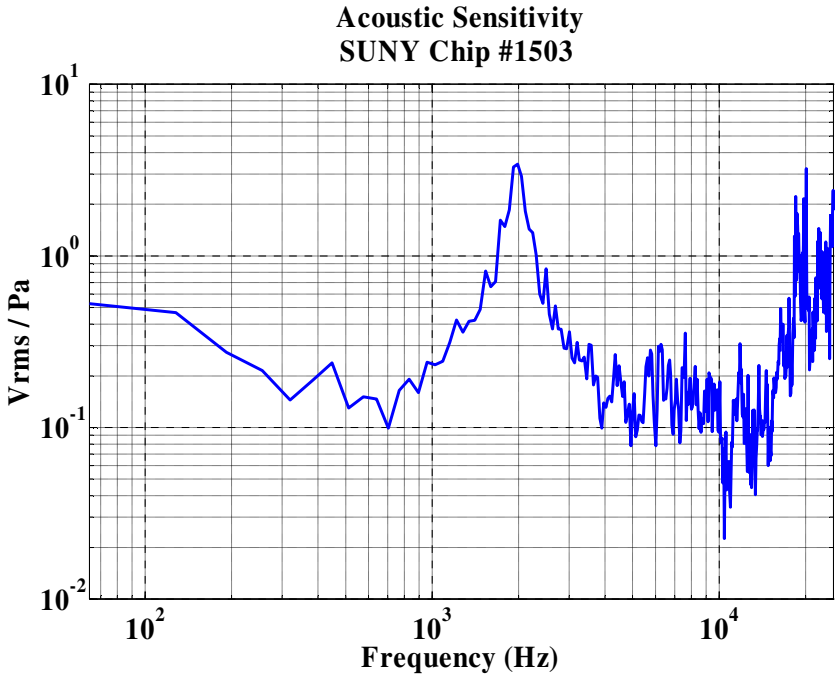

Figure 2.13 Acoustic frequency response measured using prototype test bed

It can be seen from this data that the device has a minimum sensitivity of around 0.1V/Pa across much of the frequency range. The sensitivity exceeds 3V/Pa at 2kHz, corresponding to the rotational mode resonance of the membrane. The increased sensitivity at the upper range of the spectrum is due in part to the flapping mode resonance of the device, which peaks at 28kHz. The location of the resonance peaks was verified by independent laser vibrometer measurements taken by the fabrication team.

Noise Measurements

Noise measurements are conducted using the same experimental setup as the acoustic frequency response test depicted in figure 2.12. For the noise tests, however, the amplifier, speaker, and calibration microphone are not used. The voltage noise spectrum of the biomimetic microphone is measured in the absence of acoustic input using the SRS signal analyzer**.** This data is shown in figure 2.14. Division of the voltage noise

spectrum by the acoustic sensitivity (figure 2.9) yields the pressure noise spectrum, shown in figure 2.15.

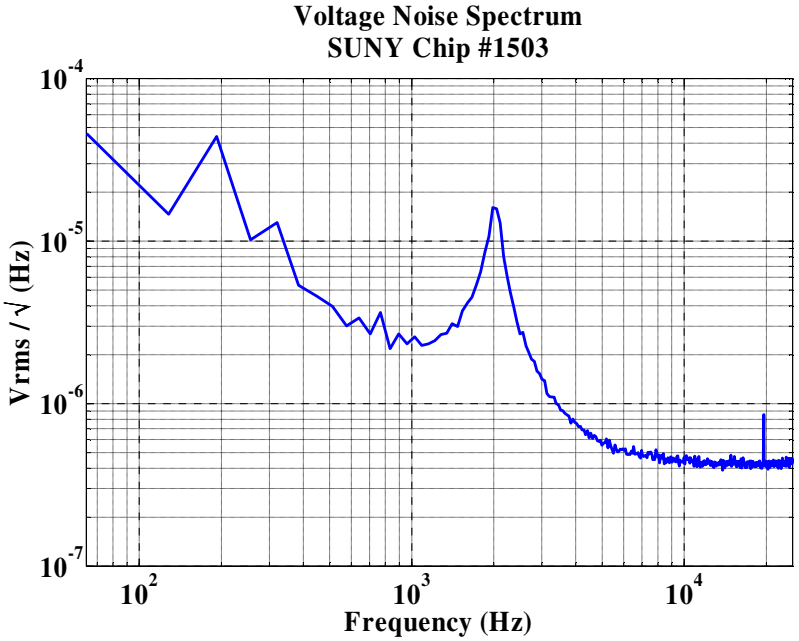

Figure 2.14 Voltage noise spectrum measured using prototype test bed

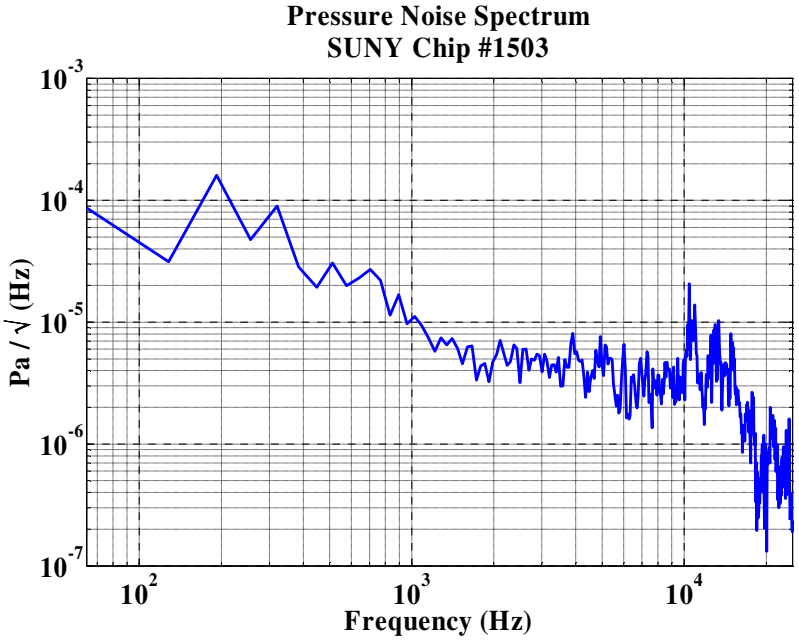

Figure 2.15 Pressure noise spectrum measured using prototype test bed

The pressure noise spectrum can be used to calculate the noise Sound Pressure Level (SPL) of the device, quoted in dBA. This metric quantifies the overall noise performance of the device across the audio spectrum. In order to calculate the noise SPL, the pressure noise spectrum (figure 2.15) is scaled by the standard A-weighting filter, which approximates the sensitivity of the human ear. The A-weighting filter is shown in figure 2.16. The resulting A-weighted pressure noise power spectrum is shown in figure 2.17.

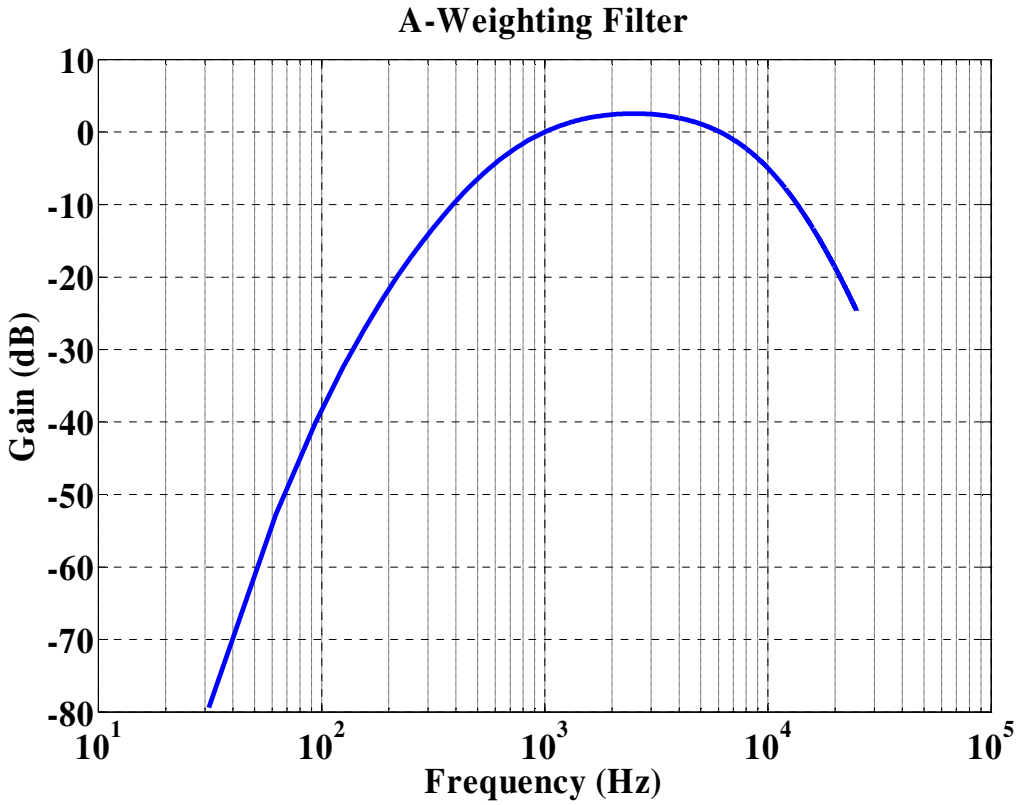

Figure 2.16 A-weighting filter applied to pressure noise spectrum

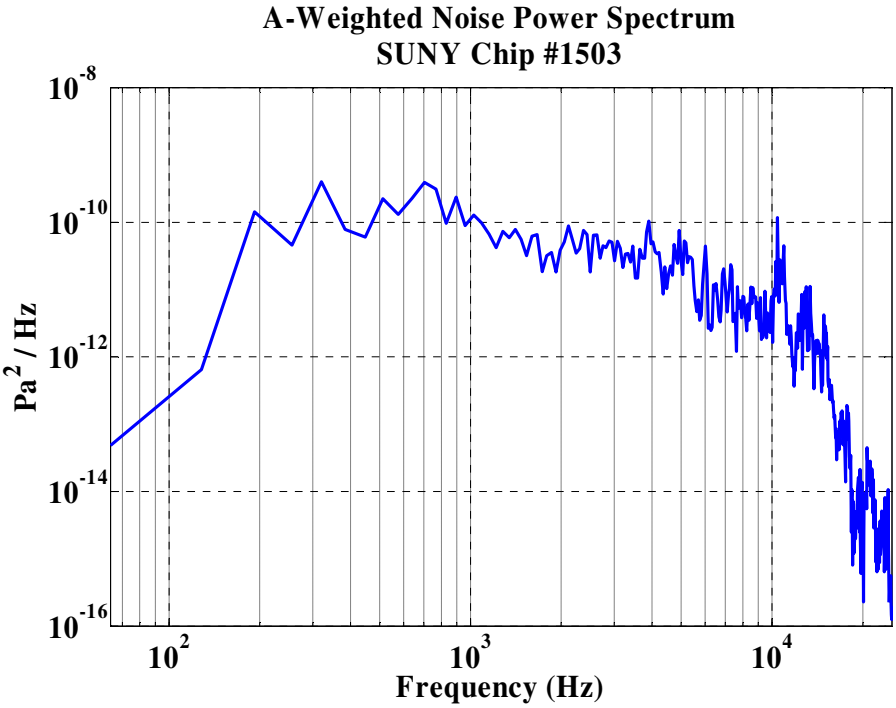

Figure 2.17 A-weighted pressure noise spectrum measured using prototype test bed

Integration of the data in figure 2.17 results in a Noise SPL of 30.2dBA, which is comparable with conventional omnidirectional hearing aid microphones. In light of the 1st order dipole directivity expected by the device, this is a significant result. Directivity tests were not conducted using the prototype test bed due to the obstruction it imposes in the field. The goal of the remainder of this work is to realize a low noise microscale implementation of the optical microphone architecture that demonstrates 1st order dipole directivity patterns. The development and characterization of such a device is presented in the following chapters.

CHAPTER 3

DESIGN, MODELING AND FABRICATION OF MICROPHONE PACKAGES

The results presented in Chapter 2 demonstrate the potential for implementation of optical displacement detection in microphone applications. In order adapt this technology for hearing aids, however, it is necessary to miniaturize the optical detection architecture such that the entire device fits within in a standard hearing aid shell form factor, as depicted in figure 3.1.

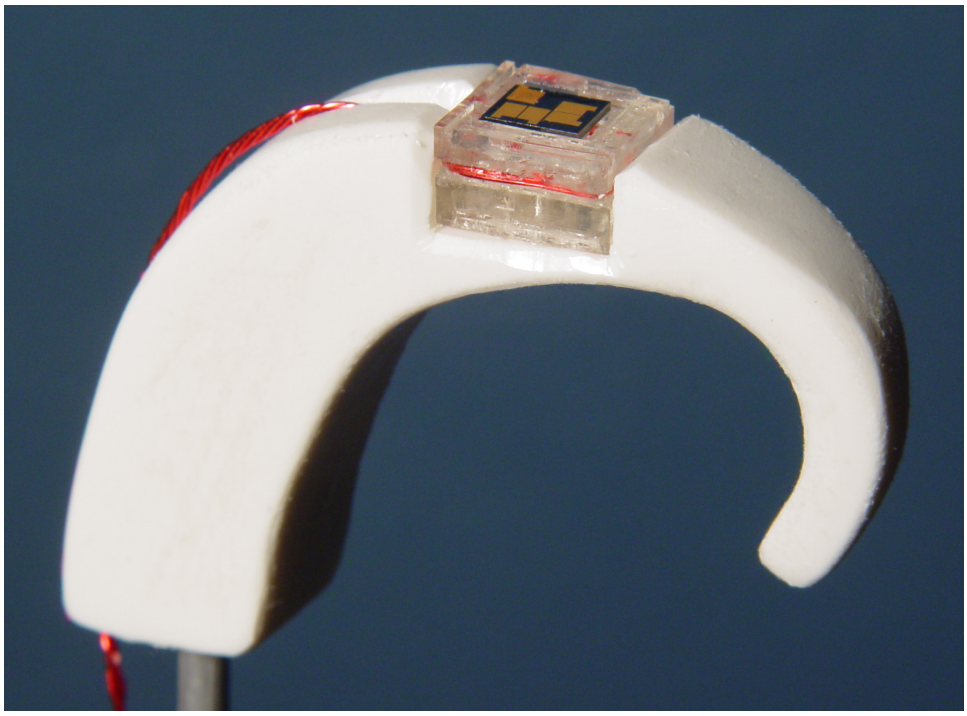

Figure 3.1 Model of integrated microphone mounted in hearing aid shell

The miniaturization of the optical detection architecture is presented in this chapter, followed by the design, modeling, and fabrication of the miniaturized microphone packages.

Miniaturization

A major constituent in the realization of the integrated hearing aid microphone was the replacement of the detection optics in the prototype test bed with microfabricated optoelectronic devices. A survey of available technologies led to the selection of a Vertical Cavity Surface Emitting Laser (VCSEL) to replace the diode laser. The commercial photodiode array was replaced by a custom designed miniature photodiode array. This provided a great deal of design flexibility because the locations of the photodiodes could be arranged in configurations not available in commercial arrays. A schematic of the micro-optical detection architecture is shown in figure 3.2.

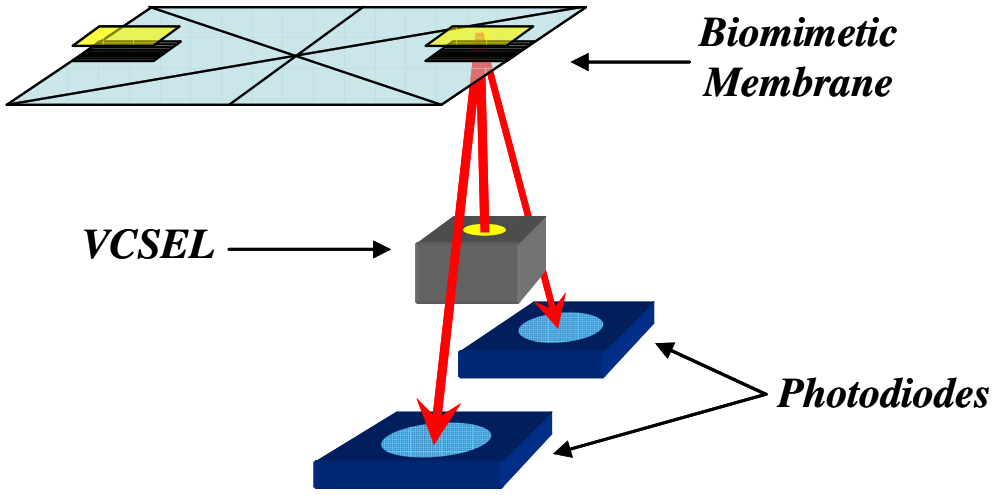

Figure 3.2Micro-optical detection architecture

Vertical Cavity Surface Emitting Lasers

A Vertical Cavity Surface Emitting Laser (VCSEL) is a microfabricated laser conventionally employed in fiberoptic telecommunications systems. These devices can be fabricated in the sub-mm range, making them ideal for integration in the micro-optical detection architecture. VCSELs are available in both multimode and singlemode varieties. Although multimode VCSELs can be purchased for a fraction of the cost, singlemeode VCSELS are preferred due to their Gaussian beam profiles and inherently lower noise levels.

Unlike the diode laser implemented in the prototype test bed, VCSELs have a relatively large divergence angle, often exceeding 30° (FWHM). Large divergence angles can potentially decrease the SNR of the detection architecture, as discussed in the following chapter. This is not an issue if the VCSEL is coupled with the appropriate lens. However, the inclusion of standard lens significantly increases the spatial requirements of the detection optics and complicates the package design. At the time of this work, commercial VCSELs with integrated lenses were not widely available, and the cost for such a component was not justified by the performance gain. A survey of existing technologies led to the selection of two models of singlemode VCSELs with relatively small divergence angles. These devices are illustrated in figure 3.3.

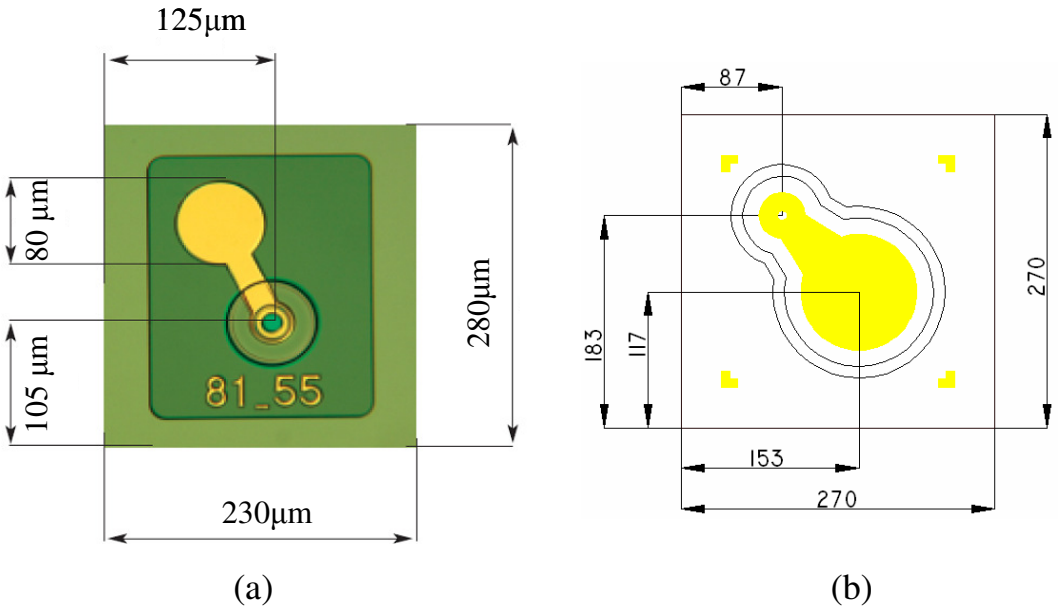

Figure 3.3 Commercial VCSELs implemented in micro-optical detection architecture [26,27]

The device in figure 3.3(a) was manufactured by Avalon Photonics, Ltd. This device has an optical wavelength of 850nm, an optical power output of 1.25mW, and a divergence angle of 10° (FWHM). The dimensions of the die are 230µm x 280µm [26]. A second device manufactured by LaserMate Group, Inc. was implemented in later devices (figure 3.3b). This device has an optical wavelength of 850nm, an optical power output of 2mW, and a divergence angle of 8° (FWHM). The dimensions of the die are 270µm x 270µm x 130µm [27]. Both of these devices require a current injection in order to produce the desired 850mn Gaussian beam. The cathode pads of the VCSELs are located on the bottom of the substrate. A gold bond pad on the surface of the chip provides the anode connection.

Photodiode Arrays

CAD schematics of the two photodiode configurations implemented in this work are illustrated in figure 3.4.

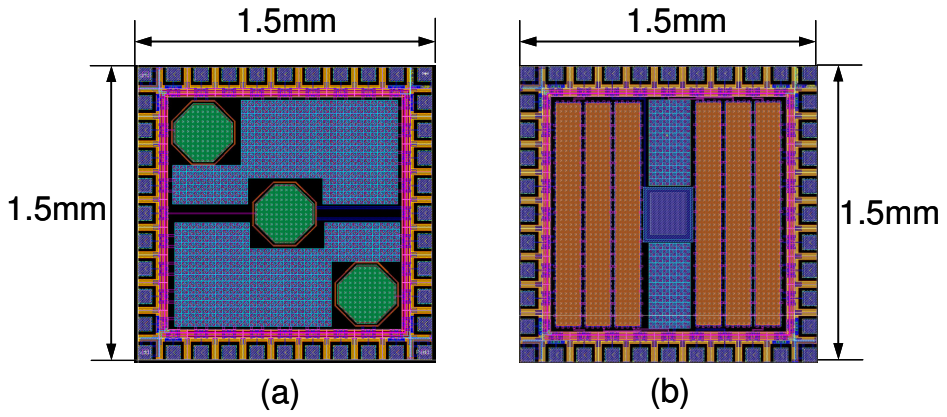

Figure 3.4 Schematics of photodiode arrays

Both of these devices measure 1.5mm x 1.5mm, making them ideal for integration in the micro-optical detection architecture. Initial devices were integrated with the 3-element array shown in figure 3.4a. The green octagons represent the active areas of the photodiodes, each of which measures the intensity of one of the 0^{th}, 1^{st}, and -1^{st} orders. The 6-element photodiode array shown in figure 3.4b was later implemented in order to capture more light and increase the optical alignment tolerance of the detection scheme. The six brown rectangles in this schematic represent the active photodiode areas. This configuration allows measurement of intensity levels at three consecutive locations for each of two orders being measured. The array produces a separate photocurrent for each photodiode, resulting in six signals which can be amplified and measured independently.

3-Layer Microphone Package Design

A miniaturized optoelectronic package was designed to house, optically align, and electrically interface the biomimetic membrane chip and the microscale optoelectronic components. Figure 3.5 illustrates the basic configuration of the 3-layer polymer package.

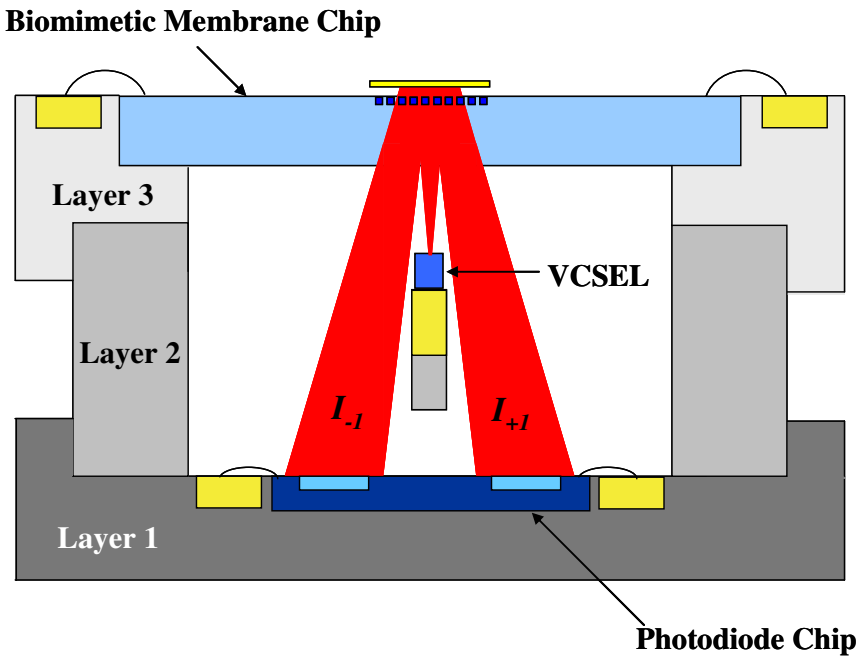

Figure 3.5 Schematic of 3-layer microphone package design

Each layer houses one of the three main components of the microphone: Layer 1 houses the photodiode chip, Layer 2 houses the VCSEL chip, and Layer 3 houses the biomimetic diaphragm (SUNY) chip. The three package layers represent polymer components fabricated using high-resolution Stereolithography Apparatus (SLA) equipment.

The yellow rectangles in figure 3.5 represent gold-plated copper leads embedded in the SLA parts after fabrication. Wire bonds can be made directly to the surface of these leads, which serve as both bond pads and electrical interconnections. Layer 1 requires one ground connection and one additional connection for each photocurrent that will be measured. Layer 2 requires two leads: one ground and one power connection for the VCSEL. Layer 3 requires two connections in order to electrostatically actuate the membrane.

One caveat that should be noted is that the VCSEL cathode connection is on the bottom of the substrate. In order to accommodate this connection, the VCSEL is mounted directly on top of a 250um wide gold-plated lead embedded in Layer 2. This lead is suspended directly above the center of the photodiode array by a thin polymer bridge in order to minimize the disruption of the field. Because the VCSEL obstructs the 0^{th} order, the $\pm 1^{st}$ orders are used for detection.

The modular 3-Layer package design streamlines the assembly process because each layer can be assembled and tested independently. This also facilitates the replacement of failed components in the event of a device malfunction. Because the microphone will be assembled manually, the package is designed with alignment features which accurately position and orient the optoelectronic components relative to one another. The results of the optical calculations presented in the following sections were used to determine the critical dimensions of the package components.

Optical Modeling

In the preliminary phases of design, the relative locations the optoelectronic components were based on the far field approximation for the diffraction angle given by equation 1.12. This approximation is only valid in the far field, which means that it applies at distances much greater than the Rayleigh distance of the beam, given by

$$z_r = \frac{\pi w_0^2}{\lambda} \tag{3.1}$$

where λ is the optical wavelength and w_0 is the beam waist. The beam waist of commercial VCSELs is not typically quoted by the manufacturer. For Gaussian beams, this parameter can be approximated as

$$w_0 = \frac{\lambda}{\pi\gamma} \tag{3.2}$$

where γ is the VCSEL beam divergence angle. The VCSELs utilized in this work have divergence angles of 8° and 10° (FWHM), which translate to beam waists of 1.94μm and 1.55μm, respectively. Substitution of these values into equation 3.1 results in Rayleigh distances of 13.9μm and 8.9μm. As the minimum propagation distance in the microphone packages is ~100 times greater that this, it can be concluded that the far-field approximation is valid.

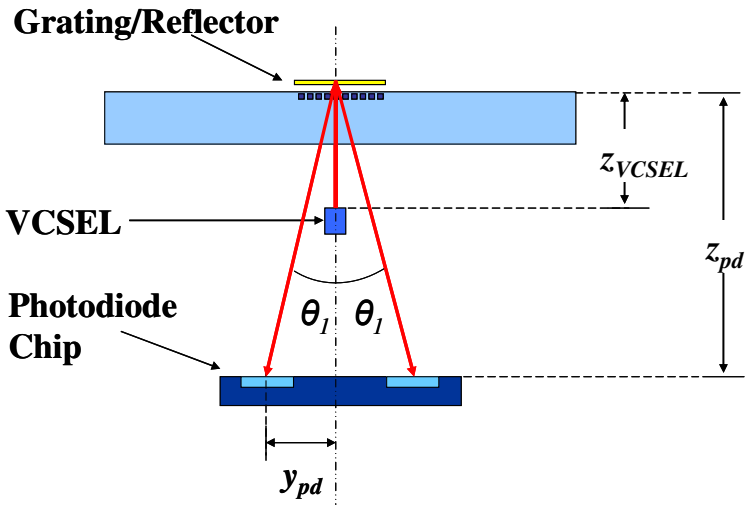

Figure 3.6 Relative geometry of optoelectronic components

The basic package geometry is illustrated in figure3.6. For a grating period of 4μm and an optical wavelength of 850nm, the diffraction angle given by equation 1.12 is 12.27°. Order separation in the x direction is limited by the pitch of the photodiode array, which is 587.5μm for the array in figure 3.4a. This design constraint results in a distance Z_{pd} of 2701μm between the grating and photodiode planes. The VCSEL is elevated above the photodiode plane in order to reduce the spot size of the beam on both the grating and

photodiode planes. This can potentially increase the electrical sensitivity of the device because more light power will ultimately be converted into photocurrent for a given VCSEL power and membrane deflection. The distance between the VCSEL and grating was therefore minimized to 1.2mm.

The 3-element configuration provides limited tolerance for optical misalignment, which is likely to occur in manually assembled prototypes. A VCSEL chip tilted off-axis, for example, could significantly shift the projection of the diffracted orders on the relatively small active photodiode areas. Initial devices implementing this design exhibited very poor performance in terms of sensitivity and noise floor.

While the analysis presented above accurately calculates the far field diffraction angle, it does not account for the divergence of the incident beam. This was not an issue in the case of the prototype test bed due to the negligible divergence of the beam. Beam divergence can causes complications in the detection scheme, particularly when the divergence angle of the incident beam is larger than the diffraction angle. In such cases, the adjacent orders overlap each other, resulting in unwanted interference which degrades the desired optical signal. Because the even and odd orders are 180° out of phase, overlap of the 0^{th} and ±1st orders results in a net increase in the DC level of the optical signal. As laser intensity noise is directly related to the DC signal level, overlap of the diffracted beams results in an increase in the noise floor of the device and a corresponding decrease in the signal to noise ratio (SNR). In order to optimize the quality of the optical signal, the photodiodes must be located in regions with as little beam overlap as possible. A more detailed optical analysis was therefore necessary to better understand the optical field. This is the subject of the following section.

Optical Simulations

An existing computer simulation was used to calculate the 2-dimensional optical intensity profile at the photodiode plane for various optical and geometric configurations in order to better understand the effects of beam overlap and use this information to enhance the package design. The simulation algorithm calculates a discrete approximation of the Fresnel-Kirchhoff diffraction integral, defined in equation 3.3.

$$u(x_n, y_n) = \frac{1}{i\lambda} \int_{-\infty}^{\infty} \int_{-\infty}^{\infty} G(x) \frac{e^{-ikr}}{r} dydx \tag{3.3}$$

This analytical expression, which is derived using the principles of scalar diffraction theory, relates the field intensity $u(x_n,y_n)$ in the viewing plane(X_n,Y_n, Zn) to an aperture function *G(x)*. The variable k is the wave number, and r is the distance between a point (x,y) in the aperture plane (X,Y,Z) to a point (x_n,y_n) in the viewing plane. The corresponding expression for r is

$$r = \sqrt{z_n^2 + (x - x_n)^2 + (y - y_n)^2 + z_n^2} \tag{3.4}$$

where z_n is the distance between the origins of the aperture plane and viewing plane.

In the case of the integrated microphone, the aperture plane is the grating plane and G(x) is defined by the geometry of the diffraction grating. The grating is simulated in the software as a complex function. For the 4μm simple grating implemented in this work, the magnitude of this function is always one, assuming no light is lost at the grating. The phase shift induced by the phase sensitive diffraction grating is represented by a square wave with period T_g, finger width w_f, and amplitude φ, where φ is the phase accrued by light passing through the grating fingers. The phase of the grating function is illustrated in figure 3.7.

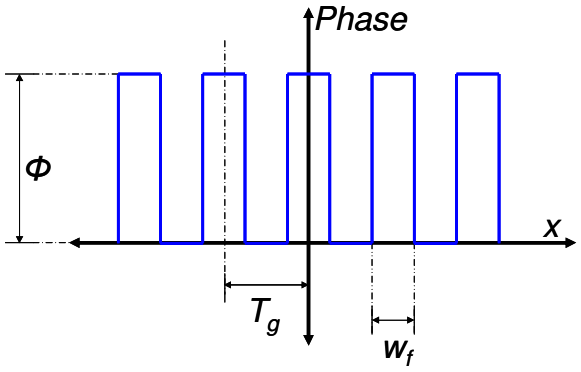

Figure 3.7 Phase of complex grating function

Analytical computation of the integral in equation 3.3 is exceedingly difficult for all but the simplest of aperture functions. For this reason, the integral is computed using the Fresnel Approximation, given by

$$u(x_n, y_n, z_n) = \left[\frac{1}{i\lambda z_n} e^{ik\left(z_n + \frac{x_n^2 + y_n^2}{2z_n} \right)} \right] \text{ x } \mathcal{F}\left\{ G(x,y) e^{ik\left(\frac{x^2+y^2}{2z^2} \right)} \right\} \tag{3.5}$$

where $\mathcal{F}$ is the Fourier Transform[14, 16, 28, 29]

The simulation computes this approximation numerically in MATLAB. The input parameters include package geometry, diffraction grating geometry, VCSEL wavelength, VCSEL power, and VCSEL beam waist. Using these parameters, the algorithm simulates the propagation of light from the VCSEL to the phase sensitive diffraction grating and then subsequently to the photodiode plane in the form of reflected and diffracted orders, ultimately yielding the intensity field at the photodiode plane for a given membrane deflection.

Using this simulation, 2D intensity profiles were calculated for the package geometry presented in the previous section. The intensity profiles for three values of φ

are shown in figure 3.8. These simulations correspond to a 2mW VCSEL with a beam divergence angle of 8° (FWHM).

The top plot in figure 3.8 is the intensity profile at the photodiode plane when φ=0. This is essentially a pure reflection of the incident beam, and represents the maximum intensity of the 0^{th} order beam. At this phase the intensity of all of the odd orders is zero. The bottom plot in figure 3.8 is the intensity profile when $\varphi=\pi$. This represents the maximum intensity of the $\pm1^{st}$ orders and coincides with the minimum value of the 0^{th} order. The middle plot in figure3.8 is the intensity profile when $\varphi=\pi/2$. This case represents the median values of the 0^{th} and $\pm 1^{st}$ orders. The top and bottom plots represent the upper and lower limits of the linear operation range of the implemented detection architecture for a device biased at the point of maximum sensitivity.

Because the diffracted orders are spatially distributed along the x-axis, the intensity at the photodiode plane can better be understood by displaying the 1-dimensional intensity profile along this line. For this reason the simulation plots the intensity profile along the x-axis for the extreme values of φ. The 1D profiles for phase values of 0 and π are superimposed in order to evaluate the overlap of the 0^{th} and $\pm1^{st}$ orders, as shown in figure 3.9.

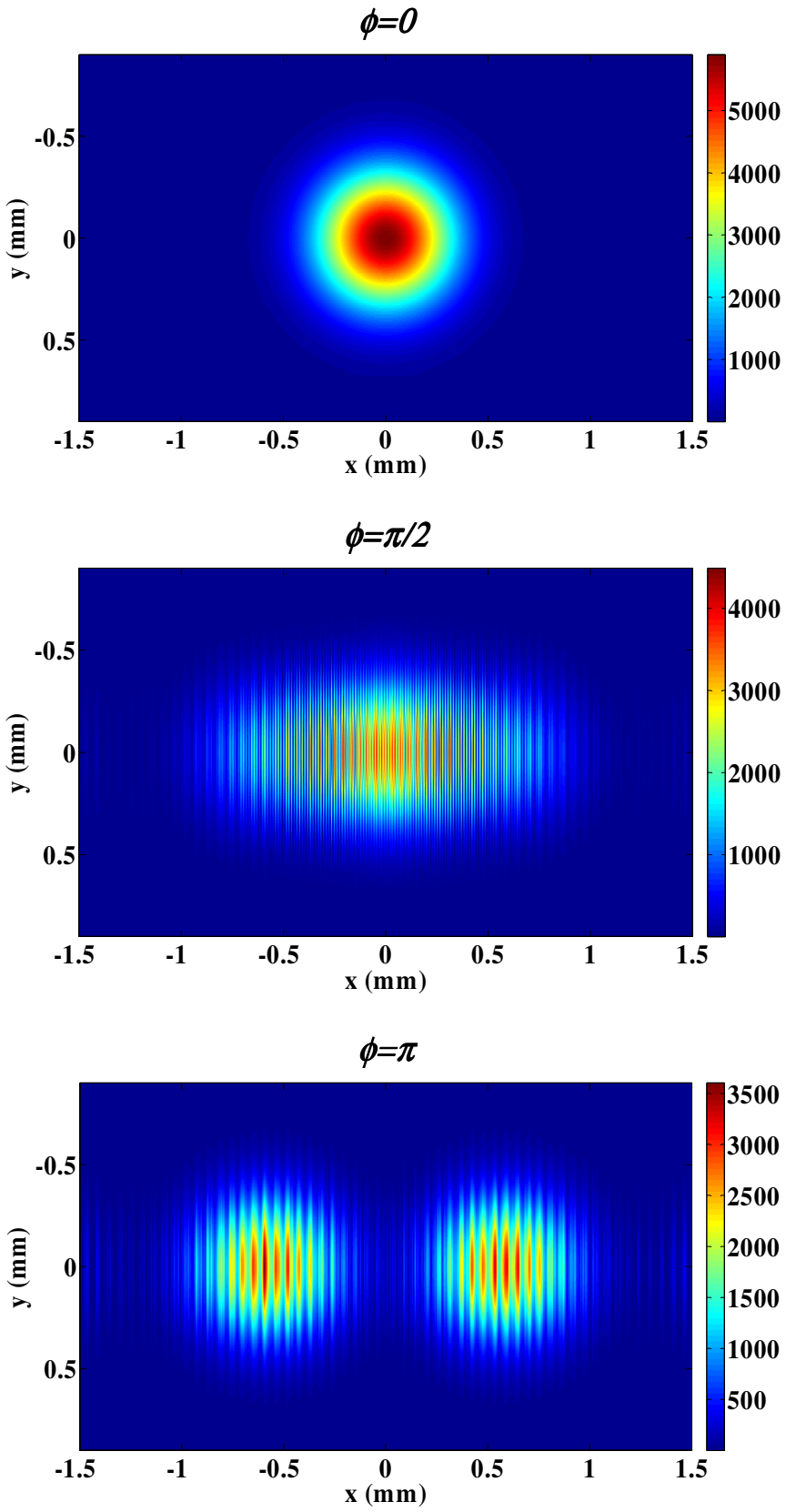

Figure 3.8 Simulated 2D intensity profiles at photodiode plane

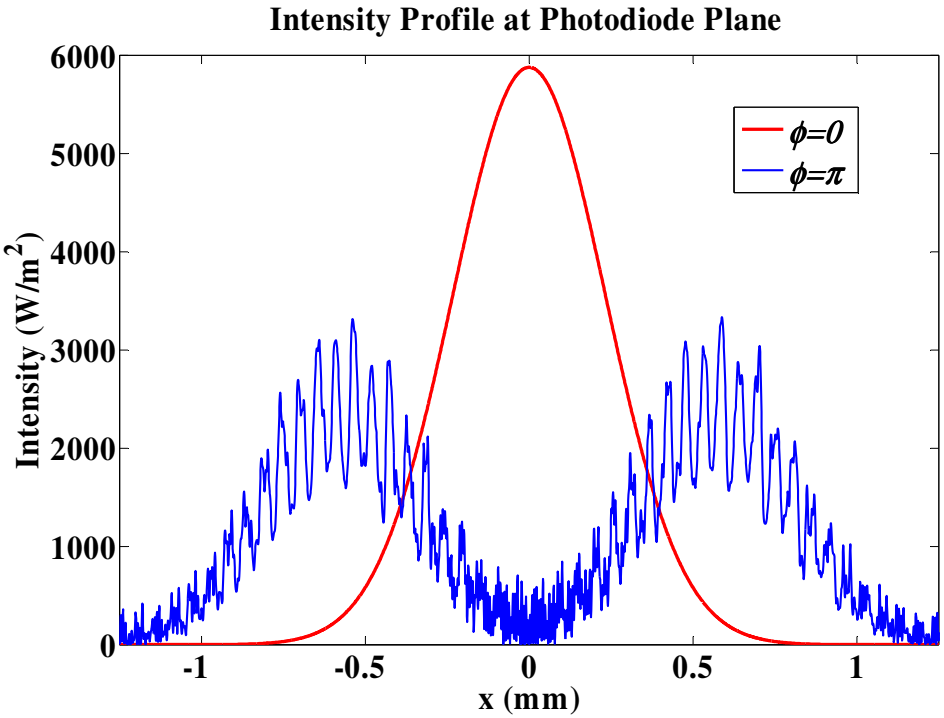

Figure 3.9 Simulated 1D intensity profiles at photodiode plane

The red curve in figure 3.9 represents the 1D intensity profile at the photodiode plane when φ=0. The blue curve represents the intensity profile when $\varphi=\pi$. The locations of the peak intensities of the 0^{th} and $\pm1^{st}$ orders are in agreement with the far-field approximation of the diffraction angle. It is clear, however, that there is a significant amount of overlap between the 0^{th} and $\pm1^{st}$ order beams. The areas where the two curves overlap represent measurement domains which result in nonzero DC signal levels. Note that the particular grating geometry simulated here results in the absence of higher even orders. Thus, all of the orders except the 0^{th} are in phase. As the $+1^{st}$ and -1^{st} orders carry identical signals, only the 0^{th} and 1st orders will be measured by the photodiodes in the implemented design.. The major area of concern is therefore the overlap between the 0^{th} and 1^{st} orders.

Augmentation of Existing Simulation

A metric which can be used to quantify the amount of beam overlap is the *Modulation Efficiency*, defined as

$$\eta_{\text{mod}} = \frac{V_{pp}}{V_{\max}} = \frac{V_{pp}}{V_{DC} + 0.5V_{pp}} = \frac{V_{\max} - V_{\min}}{V_{DC+}0.5(V_{\max} - V_{\min})} \tag{3.6}$$

where V_{pp}, V_{max}, V_{min}, and V_{DC} are the peak-to-peak, maximum, minimum, and DC voltage levels measured in the optical intensity curves, respectively. The modulation efficiency quantifies the percentage of the maximum captured light intensity that can be modulated by deflection of the membrane. The theoretical upper limit is reached as $V_{min} \rightarrow 0$ and $V_{DC} \rightarrow 0.5V_{pp}$. This corresponds to a maximum modulation efficiency of 100%, as embodied by the ideal optical intensity curves. Maximization of the modulation efficiency is therefore achieved by minimizing the DC level of the intensity curve for a given V_{max}. This should theoretically increase the SNR of the device.

In order to incorporate this information, the simulation algorithm was adapted to calculate a 1-D optical intensity curve by iterating over successively increasing values of φ, simulating incremental deflection of the membrane. For each value of φ, the intensity profile is numerically integrated over 100μm intervals spanning the x domain. This approximates the relative amount of light captured by a 100μm wide photodiode array as a function of x. The resulting intensity values at any of the photodiode locations can then plotted as a function of φ, yielding a 1D intensity curve in units of W/m. The modulation efficiency can then be calculated for the given photodiode location using equation 3.6. The algorithm repeats this calculation of modulation efficiency for each interval, effectively spanning the entire length of the calculated field. The simulated

modulation efficiencies are then plotted as a function of photodiode location along the x-axis, as shown in figure 3.10.

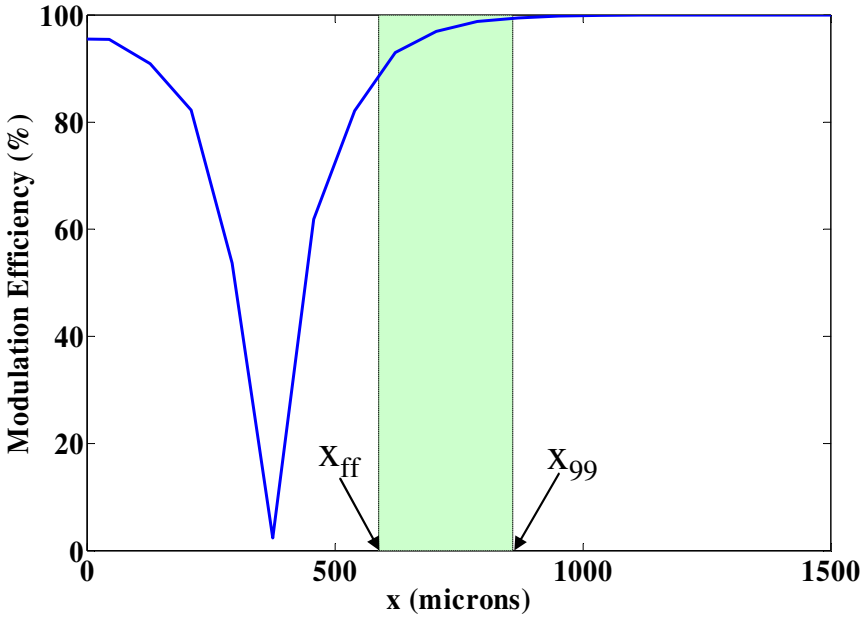

Figure 3.10 Simulated modulation efficiency vs. photodiode location

Because the field is symmetric about x=0, it is only necessary to consider the modulation efficiency for x≥0. Inspection of the modulation efficiency indicates a minimum value at x_{min}=374μm, corresponding to the location of maximum overlap between the 0th and 1st orders. The peak modulation efficiency for the 0th order is 95%, which corresponds with the maximum intensity of the 0th order beam at x=0. This is intuitively the best location for measurement of the 0th order signal.

Above x_{min}, the modulation efficiency increases asymptotically towards a theoretical upper limit of 100% at a point x_{max}. Beyond this point the field consists of only odd orders. In terms of modulation efficiency, the photodiodes measuring the ±1st orders should therefore be placed as far from the origin as possible. This conflicts with

maximization of the sensitivity, however. The maximum intensity of the 1st order is located at x_{ff}=587.5μm. Beyond this peak, the intensity of the 1st order decreases rapidly with increasing x, as indicated by figure 3.9. This corresponds to a drop in the maximum signal level, which in turn results in a drop in the maximum possible sensitivity as given by equation 1.16. Therefore, there is an inverse relationship between modulation efficiency and sensitivity in the region $x_{ff}<x<x_{max}$. It was deduced from this information that there exists a location in this domain at which the balance between modulation efficiency and sensitivity results in a maximum SNR. The design of the microphone package was therefore adapted to implement an array of photodiodes which measures the signal at multiple locations within this domain. For practical purposes, the upper limit of the measurement domain was taken as x_{99}=858μm, which corresponds to 99% modulation efficiency. The 6-cell photodiode illustrated in figure 3.4b was implemented to span the domain $x_{ff}<x<x_{99}$. A scale representation of this array is superimposed on the intensity profile in figure 3.11.

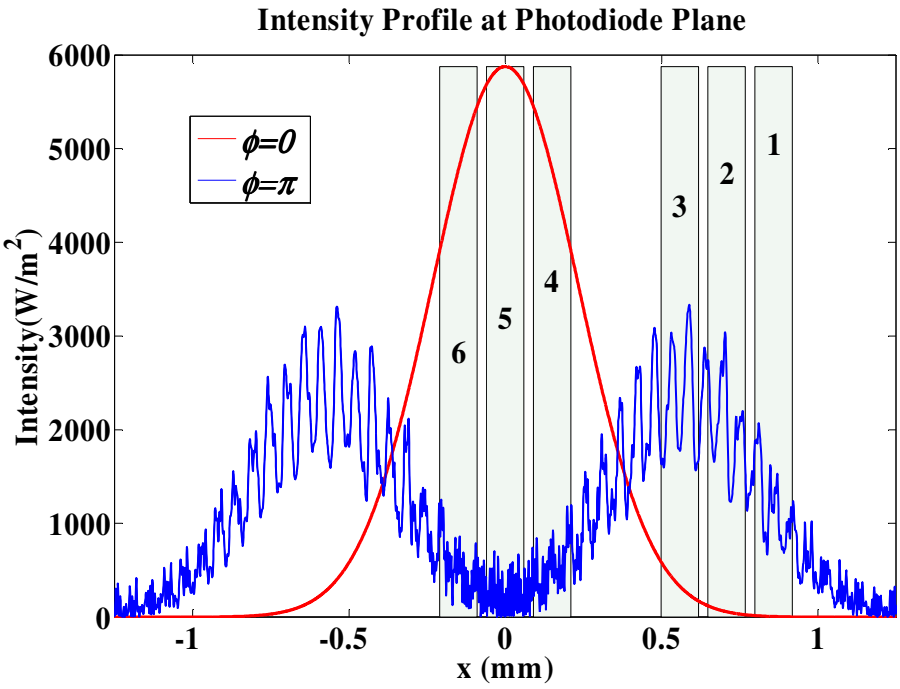

Figure 3.11 Photodiode locations superimposed on simulated 1D intensity profiles

The six rectangles represent the width and location of the photodiodes in the array. The photodiodes labeled 1, 2, and 3 are used to measure the 1st order signal, and those labeled 4, 5, and 6 are used to measure the 0th order signal. Each photodiode produces an independent photocurrent, resulting in three signals for each measured order. The signal with the best SNR can then be identified experimentally and used for measurements.

The 0th order photodiode trio is centered about x=0. This is clearly the best location based on the simulations. It should be noted, however, that the VCSEL partially blocks the 0th order beam, the effects of which are not accounted for. It is assumed that this will necessarily degrade the 0th order signal. For this reason, better measurements are expected from the 1st order photodiodes.

Photodiode 3(referred to as PD3) is positioned at the lower end of the 1st order measurement domain at the location x_{ff} dictated by the farfield approximation for the

location of the 1st order. PD1 is located at the upper end of the measurement domain at x_{99}. PD2 is centered between PDs 1 and 3. The simulated optical intensity curves for these three photodiode locations is shown in figure 3.12

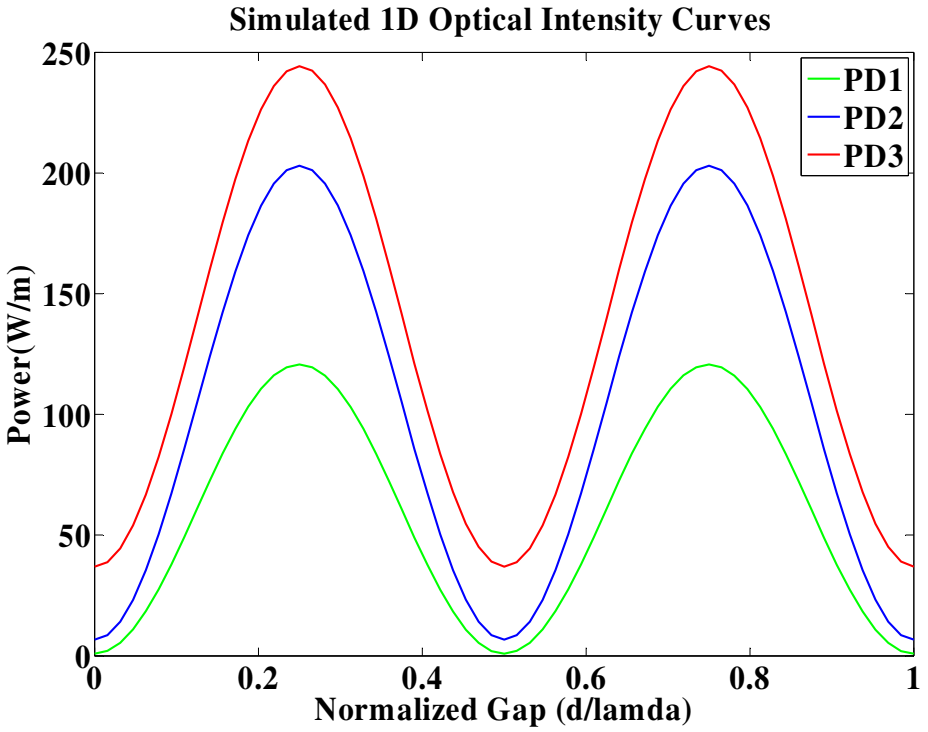

Figure 3.12 Simulated 1D optical intensity curves for three photodiode locations

Table 3.1 Simulated performance metrics for 1st order measurement locations

	S_e (relative)	η_{mod} (%)
PD1	0.58	99
PD2	0.95	97
PD3	1.00	85

The corresponding modulation efficiencies and relative sensitivities for PD1, PD2, and PD3 are listed in table 3.1. The simulated data illustrates the inverse relationship between the displacement sensitivity and modulation efficiency. Based on this trend, it is reasonable to expect that the signal with the best SNR will be measured by PD2. This conclusion is verified by experiment in chapter 5.

A scale outline of the photodiode array is superimposed on the 2D intensity profiles in figure3.13. This schematic illustrates the actual size, location and orientation of the photodiodes in the implemented design. The dimensions of each active photodiode element are 120um x 1122um. The three elements in each sub-array are spaced at a pitch of 150um. The relatively narrow width and pitch of the photodiodes provides significant tolerance for optical misalignment in the x-direction. Because all of the diffracted orders lie along the x-axis, the relatively large y-dimension of the photodiodes increases the overall photocurrent generated for a particular x location and provides tolerance for optical misalignment in the y-direction.

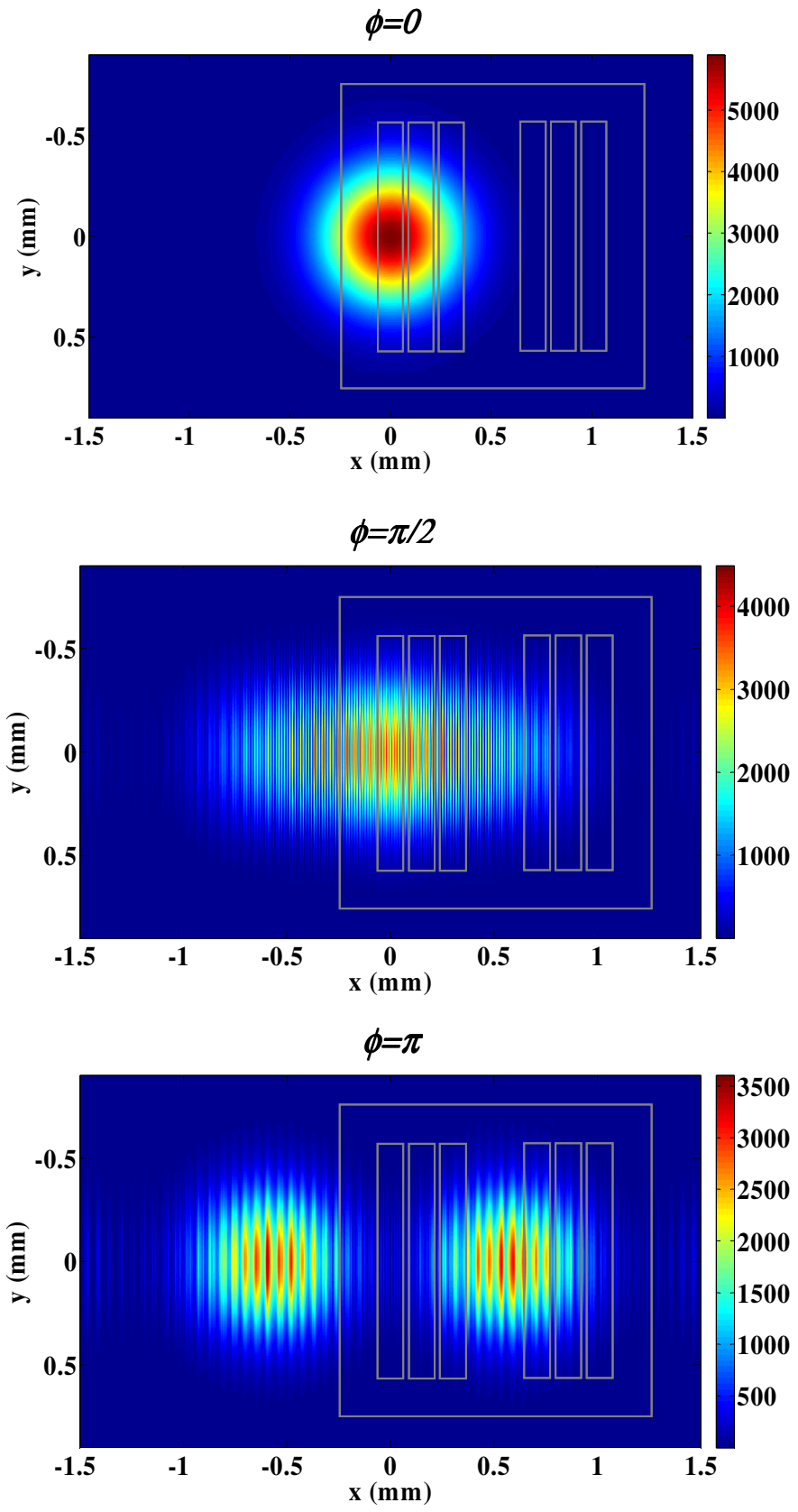

Figure 3.13 Schematic of photodiode array superimposed on 2D intensity profiles

Assumption and limitations of the optical simulations should be noted at this point. First, the simulations assume an infinitely long grating with perfect reflectivity which returns all of the incident light as 0^{th} and higher orders. As the actual gratings have finite measurements of approximately 120um x 100um, there is a substantial region surrounding the gratings which is also illuminated. In reality, light projecting outside of the grating region is either lost or returned as unwanted interference. Light is also lost to the grating fingers and reflectors themselves as a result of transmission and absorption. The second limitation regards the simulated optical intensity curves. These calculations are based on a one-dimensional integration of the simulated intensity profile along the x-axis and do not take into account variation in the y-direction. While the simulation does not yield exact calculation of the actual intensities and modulation efficiencies that would be measured, it provides relative measures of comparison for different device specifications and package geometries.

Solid Modeling of Microphone Package

The results of the simulations were used to define the critical dimensions of the integrated microphone package. The polymer package components were designed to be fabricated using Stereolithography Apparatus (SLA) technology, which is discussed in the following section. A 3D CAD model of the assembled SLA package is depicted in figure3.14, along with an exploded view in figure 3.15. The three layers fit together to form an integrated package with a total volume less than 0.5cc, satisfying the size requirements for hearing aid applications. The overall dimensions of the package are indicated in figure 3.16. The specific features of each layer are detailed in the following sections.

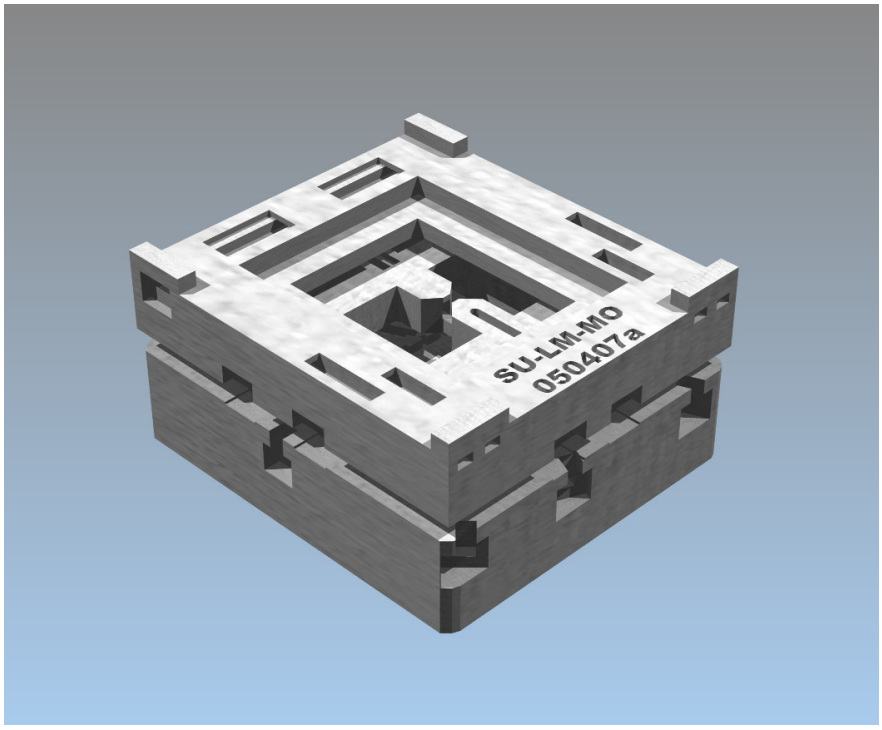

Figure 3.14 3D CAD model of hearing aid microphone package

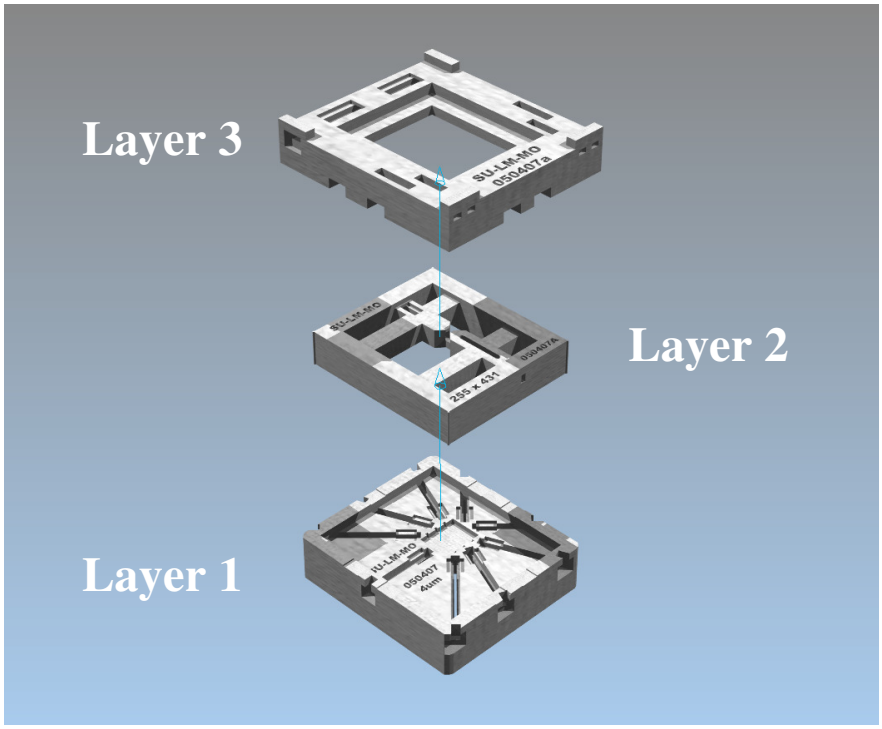

Figure 3.15 Exploded view of hearing aid microphone package

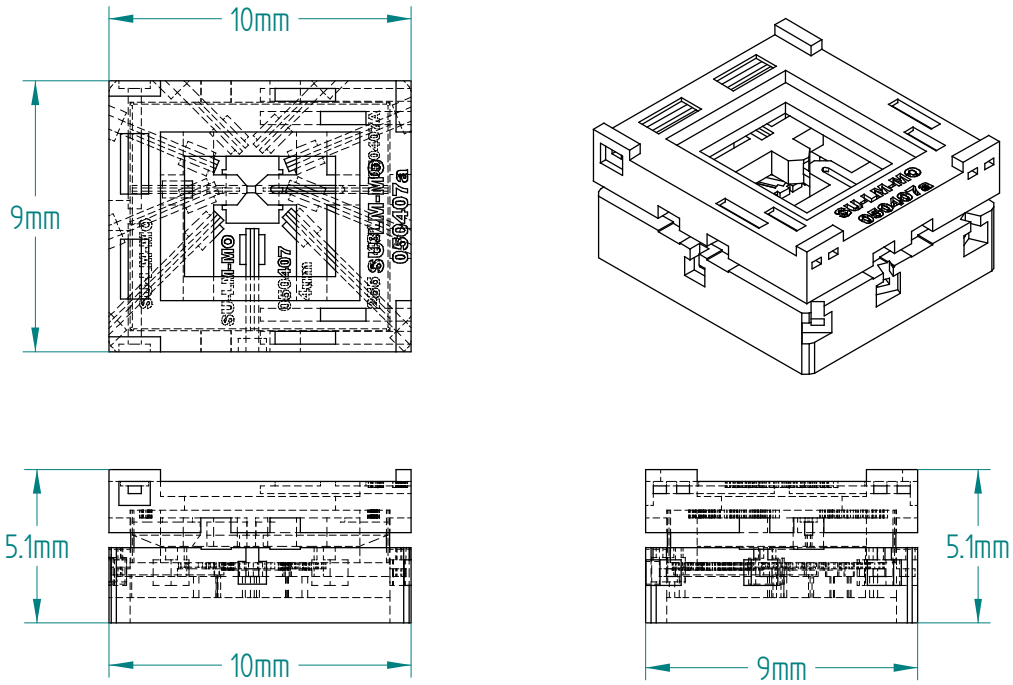

Figure 3.16 Draft views of hearing aid microphone package

Layer 1 – Photodiode Module

The features and dimensions of Layer 1 are illustrated in figure 3.17. A rectangular recess is designed to accurately position the PD Array, which measures 1.5mm x 1.5mm. Nine channels extend from the photodiode recess through the walls of the part. These channels are designed to house the electrical I/O leads for the photodiode chip, which will be installed post-fabrication. The I/O leads have a rectangular cross-section measuring approximately 250µm x 450µm. The lead channels are flared near at the ends bordering the photodiode in order to provide sufficient clearance for the tip of a wire bonder. A slit running along the bottom surface of each of the lead channels allows drainage of excess resin during the fabrication process. These drainage channels also provide relief zones for the overflow of adhesive which will be used to secure the leads in

place. Flared openings at the outside edge of the channels provide additional relief zones for injection of adhesive. A final feature to note is the lip around the top edge of the part. The recess it encompasses is designed to interface with layer 2. The tolerances are designed for a friction fit, providing highly accurate alignment between the photodiode array and VCSEL. The overall dimensions of Layer 1 are indicated in figure 3.18.

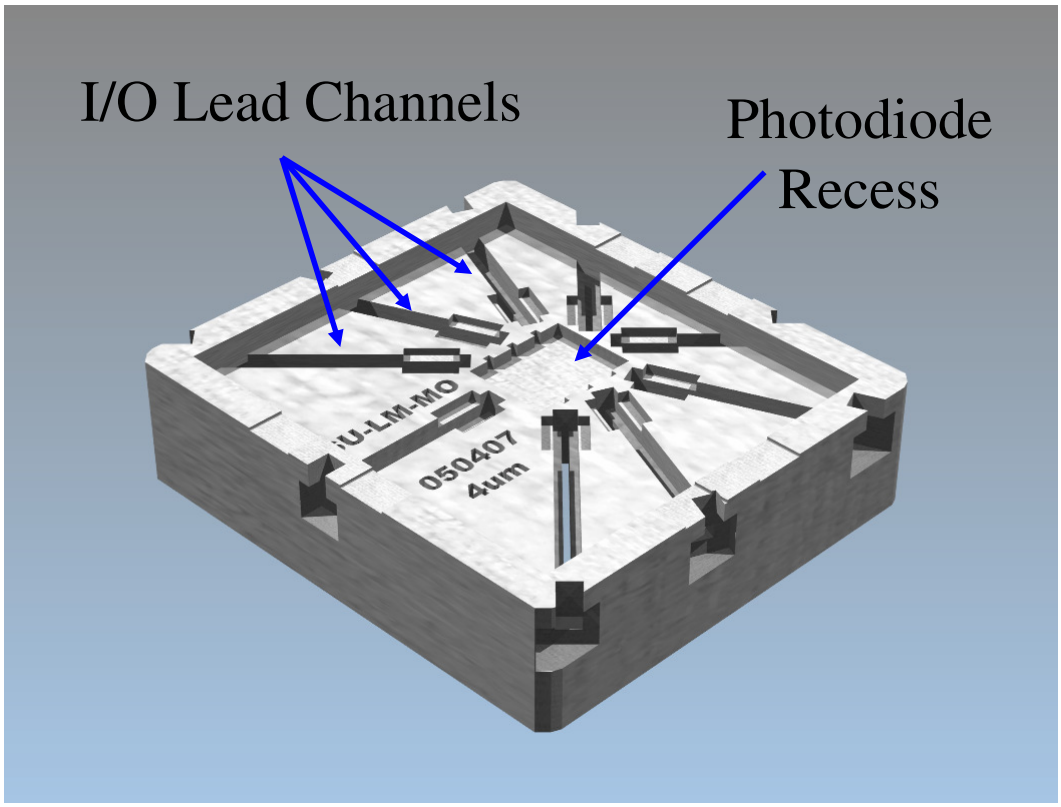

Figure 3.17 CAD model of Layer 1

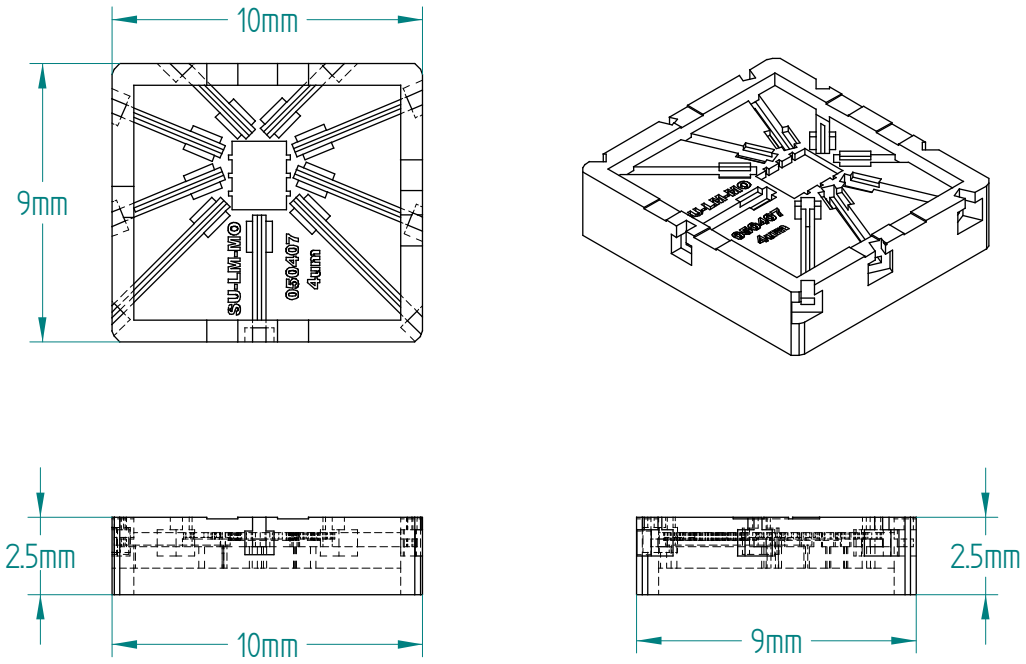

Figure 3.18 Draft views of Layer 1

Layer 2 – VCSEL Module

A 3D model of Layer 2 is shown in figure 3.19. Two challenges complicate the seemingly simple design of this layer. The VCSEL must be suspended over the photodiode array while posing minimal obstruction of the field. This issue is further complicated by the electrical connections that are necessary to operate the VCSEL. The VCSEL requires two electrical connections. The anode pad is located on the top of the chip, requiring a wire bond to the appropriate lead. The cathode pad, on the other hand, is located on the bottom of the substrate. This requires mounting the VCSEL on a conductive surface using a conductive adhesive. This is accomplished by mounting the VCSEL directly on top of a gold-plated lead supported by a thin polymer bridge, which is only as wide as the VCSEL itself. The overall dimensions of layer 2 are labeled in the drafts views illustrated in figure 3.20.

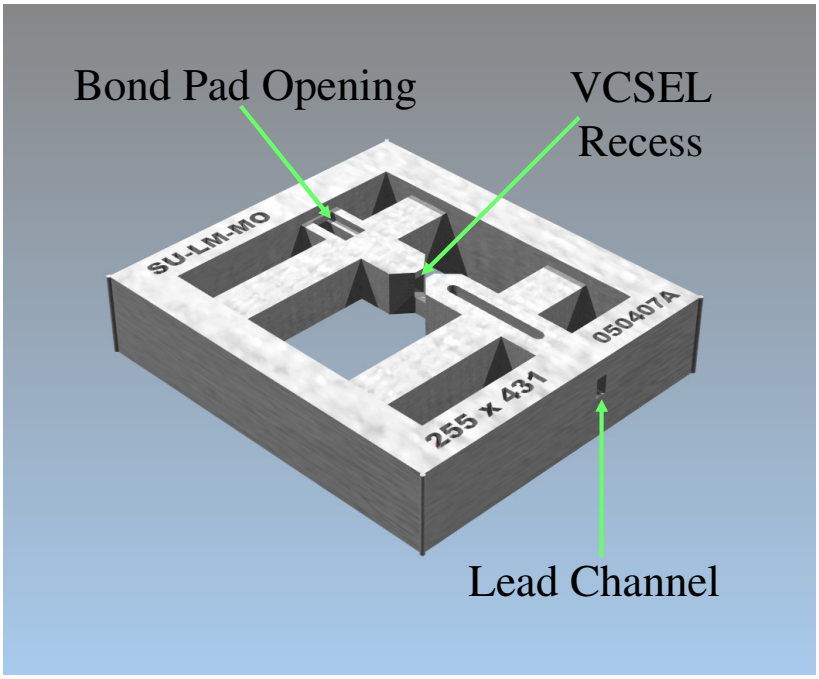

Figure 3.19 CAD model of Layer 2

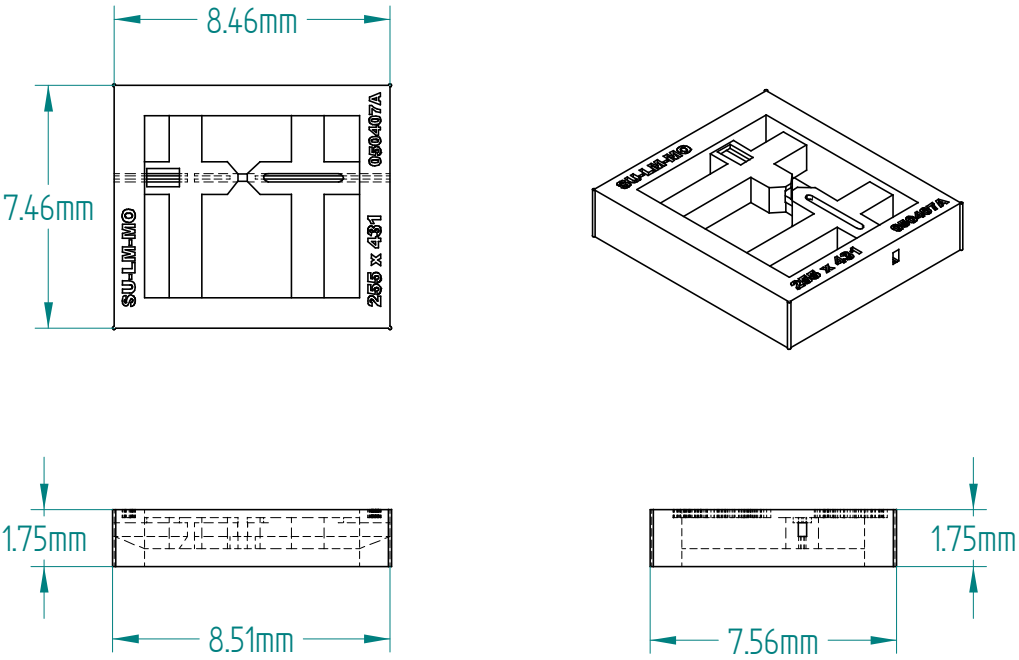

Figure 3.20 Draft views of Layer 2

Layer 3 – Biomimetic Membrane Module

A CAD model of Layer 3 is shown in figure 3.21

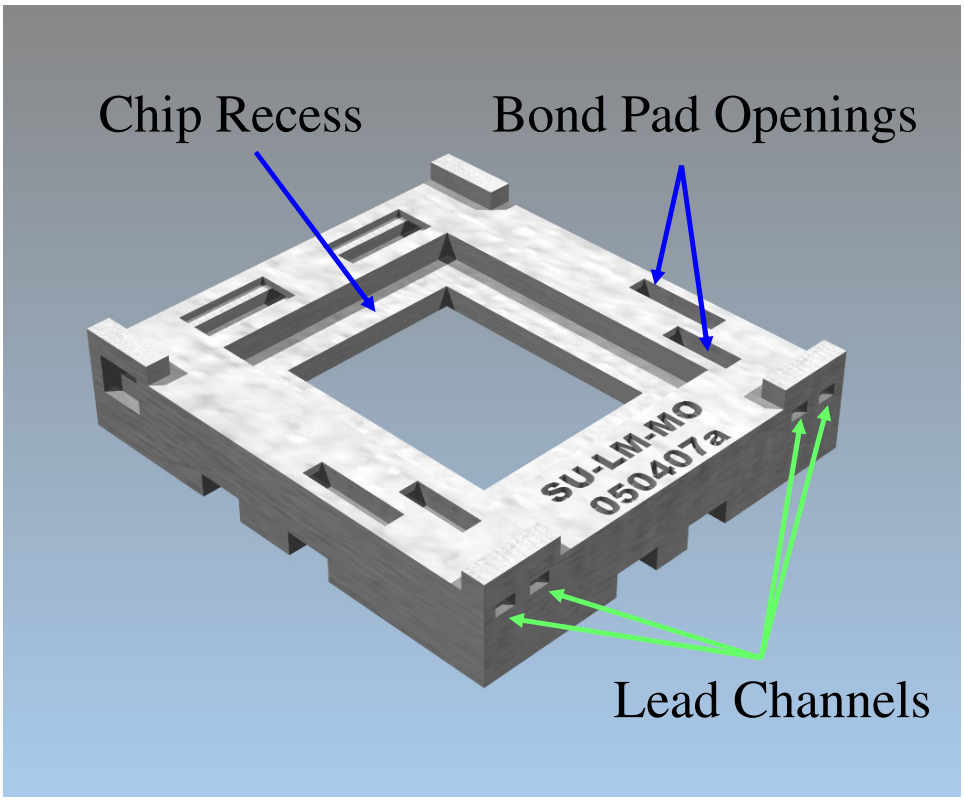

Figure 3.21 CAD model of Layer 3

A recess on the underside of the part is designed to mate with Layer 2. Layer 3 is designed to position the SUNY chip such that the grating on the biomimetic membrane is suspended 1.2mm above the lasing spot of the VCSEL. The rectangular chip recess on the top side of Layer 3 is designed to be significantly larger than the actual chip. This allows for active manual fine tuning of the optical alignment as described in Chapter 4. As with Layers 1 and 2, hollow channels are designed to house the leads that will be used to electrically connect the components of the device. In the case of Layer 3, the electrical leads interface the electrostatic actuation ports. There are a total of six such lead

channels in Layer 3, two for each membrane on the biomimetic chip. Notches along the bottom lip allow clearance for the I/O leads in Layer 2. The rectangular protrusions at the top corners of the part serve as a safety feature as they prevent the fragile MEMS device from contacting the floor or other flat surfaces in the event that device is dropped. The overall dimensions of layer 3 are labeled in the drafts illustrated in figure 3.22.

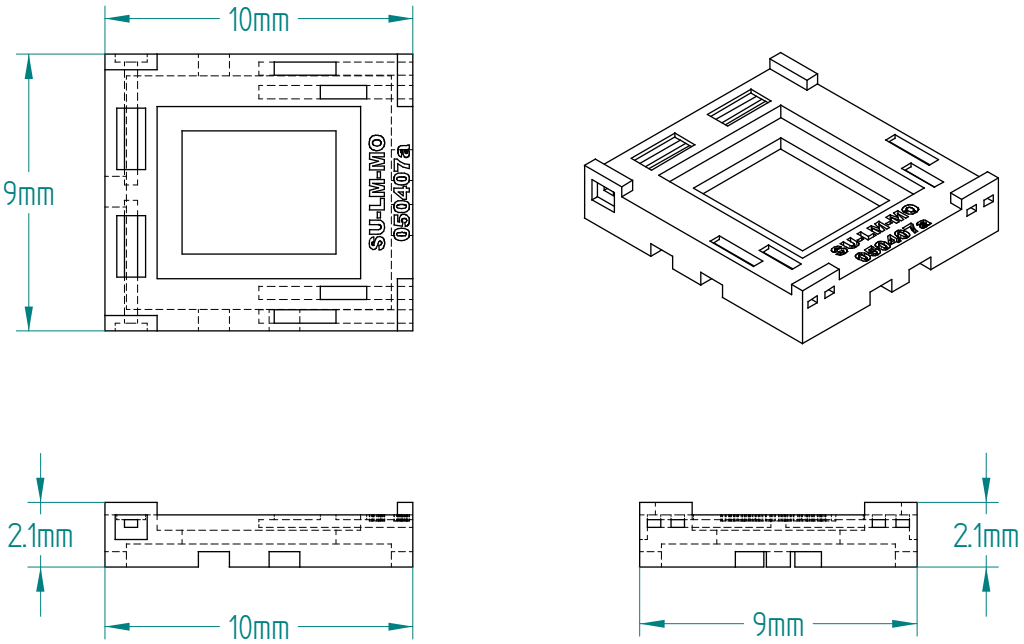

Figure 3.22 Draft views of Layer 3

The digital CAD models of the three package layers presented in this chapter were used to fabricate the parts using a high-resolution SLA machine. The fabrication of the SLA components is presented in the following section.

Fabrication of Microphone Packages

Stereolithography Apparatus (SLA) fabrication was the first industrial rapid prototyping process, and today it remains the most common rapid prototyping method in use. SLA machines form solid 3D objects in a vat of photosensitive liquid resin through photopolymerization, the selective cross-linking of monomers using a laser. Using this technology, polymer models with sub-mm feature sizes can be fabricated [30, 31, 32].

A single SLA machine can fabricate a virtually limitless variety of parts without being re-tooled or reprogrammed. The computer controlled system reads geometric part data directly from a CAD file generated using standard 3D modeling software. Multiple parts can be fabricated simultaneously in batches, similar to modern IC fabrication. As a result, multiple design iterations can be fabricated in a fraction of the time required in conventional machining processes. A number of SLA resins are available which offer varying advantages in terms of mechanical properties, resolution, build speed, and temperature capacity [32].

The SLA fabrication process can be divided into four major stages: File Preparation, Build Process, Cleaning Process, and Post-cure process. These stages are described in detail in the following sections

File preparation

As with conventional machining processes, a solid three dimensional model of the part to be fabricated is created using standard 3D solid modeling software. The CAD model is exported to STL format, the industry standard for SLA fabrication. The STL file is then prepared for fabrication using a proprietary software package supplied by the manufacturer of the SLA machine. This software package allows the operator to position,

scale, replicate, and add supports to the original model. In addition, parameters such as resolution, units, and resin type can be specified here. Finally, the software "slices" the model into layers which will be cured one at a time, beginning at the bottom of the part.

Build Process

A simplified schematic of the build process is shown in figure 3.23

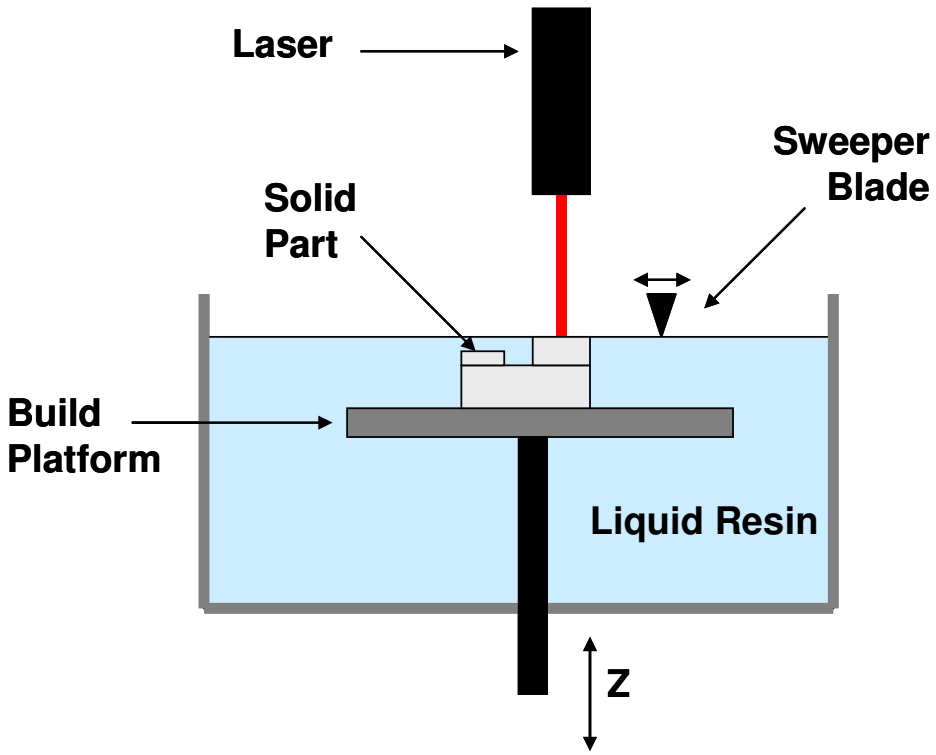

Figure 3.23 Schematic of SLA build process

The part is fabricated on a moving platform suspended in a vat of photosensitive resin. The microphone packages presented in this work were fabricating using RenShape™ SL 5510, a low viscosity resin designed for high resolution fabrication [33]. The elevator controls the vertical position of the platform such that the top layer of the part is maintained at the surface of the resin. The layers are then built on top of a polymer

support lattice anchored to the perforated build platform, beginning with the bottom layer of the part. There are three basic steps for each layer. First, a laser traces the cross-section of the current layer onto the surface of the liquid resin. As a result the resin exposed to the laser is polymerized and becomes solid. After the layer is scanned by the laser, the part is lowered by the thickness of one layer. Finally, a sweeper blade evenly redistributes liquid resin at the surface. The fabrication time depends on the size of the part and the chosen resolution. Taller parts have more layers and generally take more time, as do parts fabricated in high resolution mode. The resolution of the SLA process in the horizontal plane is limited by the spot size of the laser on the surface of the resin. The vertical resolution is limited by the elevator. The microphone packages presented in this work were fabricated using the Viper™ SLA® System manufactured by 3D Systems Corporation. This machine can fabricate parts with a minimum feature size of 150μm and a vertical resolution of 50μm [34].

Cleaning Process

The parts are drained and removed from the build platform. This requires separating the parts from the support lattice. This can be a delicate process, especially as the size of the support structures approach the size of the smaller part features. After the parts are separated they undergo an ultrasonic bath in isopropyl alcohol in order to remove liquid resin residue.

Post-Cure Process

After the parts are cleaned, they undergo a final exposure to UV light in a post-cure apparatus (PCA). This is done in order to ensure full polymerization of the material. Exposure time varies on the size of the parts, power of the PCA, and properties of the

photosensitive polymer. An image of the fabricated components of the hearing aid microphone package is shown in figure 3.24.

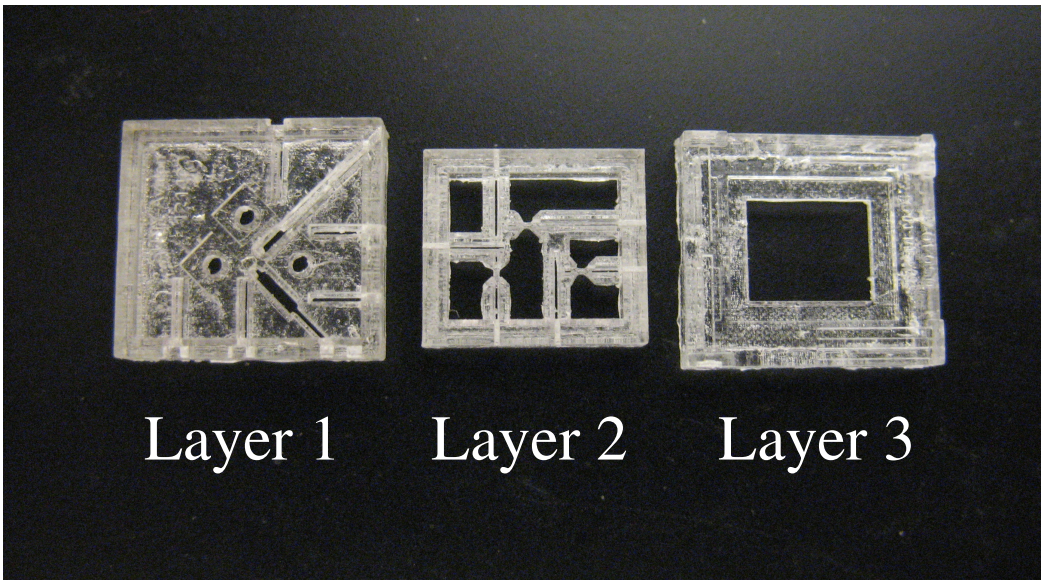

Figure 3.24 Fabricated SLA parts

The cure time for the microphone packages was approximately 30 minutes.

Limitations of SLA Technology

SLA fabrication demonstrates significant advantages in terms of resolution, design flexibility, and fabrication time. Some of the limitations of this technology are also worth noting. While the minimum feature size attainable with SLA fabrication is given by twice the minimum beam spot diameter, the resolution and quality of the model are primarily dependent on the interaction between resin and the laser. This requires precise tailoring of the resin properties and calibration of the machine for a given laser and resin combination. Furthermore, changing the resin in the machine can be time consuming. Optimization of quality and productivity therefore requires that individual

SLA machines be dedicated to a particular resin, potentially diminishing the flexibility offered by this technology in a prototyping environment [31].

The bottom-up nature of the fabrication process also poses challenges. While the potential exists to realize sub-mm resolution and excellent surface quality on the top surfaces of the part., the same is not true of the bottom surfaces of the part where the support structures are attached. In addition, the sides of the parts exhibit stratification due to the nature of the fabrication process. In parts with relatively large feature sizes, the surface quality can be enhanced post-fabrication using techniques such as polishing and sand blasting. If a part contains sub-mm features, the best results are obtained by locating these features on the same side of the part which can then be oriented towards the laser during fabrication in order approach the minimum feature size attainable by the machine.

CHAPTER 4

MICROPHONE ASSEMBLY

The assembly process is a critical and challenging constituent in the development of the integrated biomimetic hearing aid microphone, shown in figure 4.1.

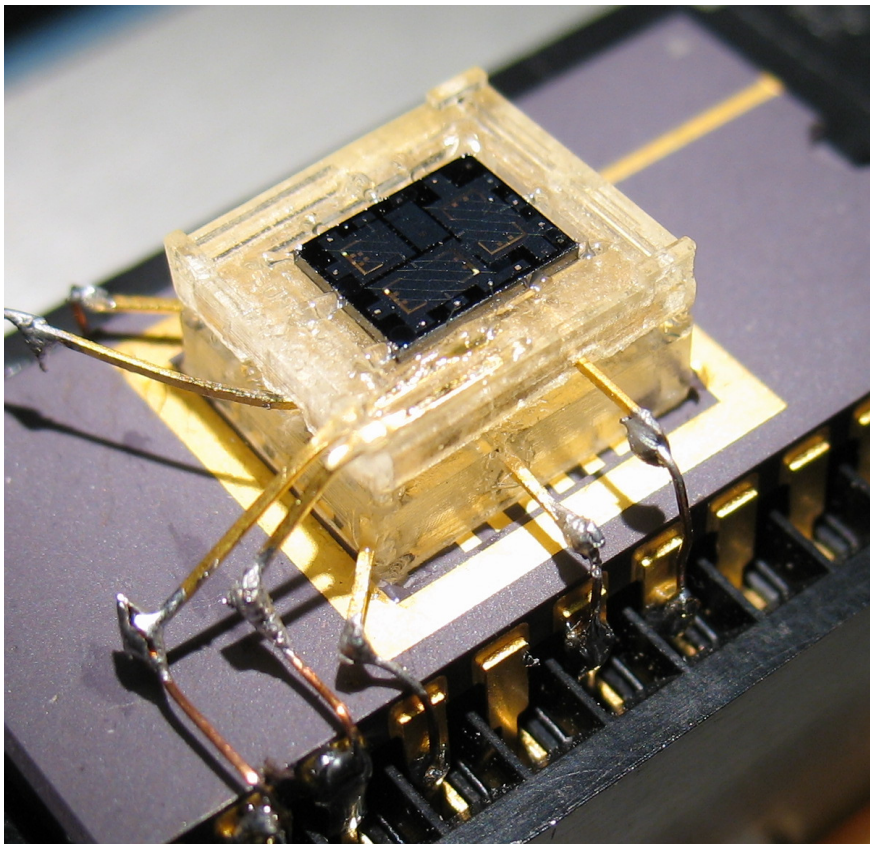

Figure 4.1 Integrated hearing aid microphone

This chapter presents the implementation of the SLA packages in the construction of prototype devices. The assembly methods and process flow are detailed in the following sections.

Assembly Process Overview

The microphone packages consist of three modular layers which are assembled individually and then integrated to form a functioning device. The design and fabrication of these parts was described in detail in Chapter 3.

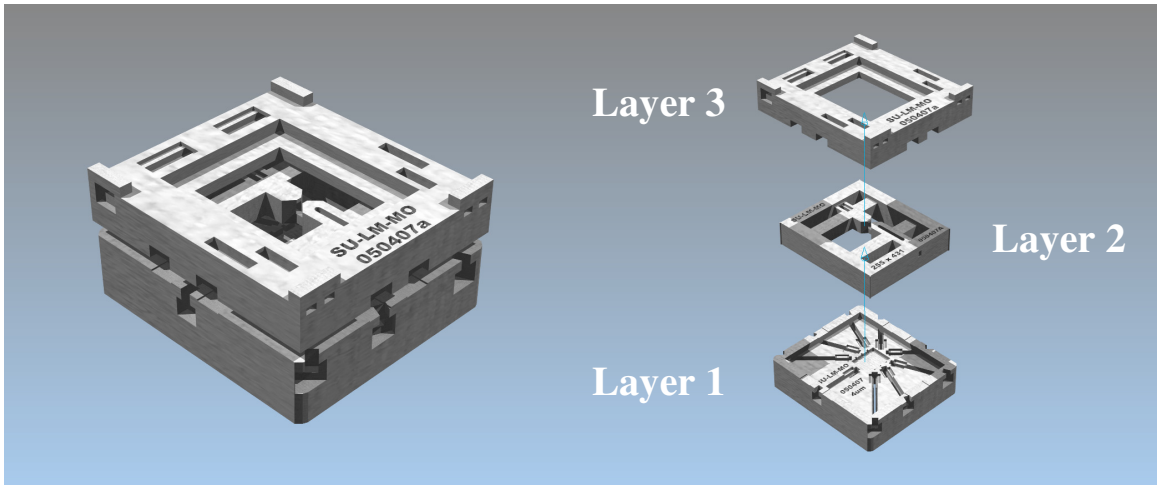

Figure 4.2 3-layer SLA microphone package

The assembly process begins with the bottom layer, labeled "Layer 1" in figure 4.2. This layer houses the photodiode chip and corresponding electrical leads. The next layer (Layer 2) is assembled and mounted on top of Layer 1. Layer 2 houses the VCSEL chip and corresponding electrical leads. The final layer (Layer 3) is mounted on top of Layer 2. Layer 3 houses the membrane chip and corresponding leads for electrostatic actuation. The optoelectronic components are tested for functionality at each stage of the process

Electrical Interconnections

The SLA parts provide both the structure of the package as well as the optical alignment features necessary for accurate alignment of the components. The electrical interconnections are created by harvesting gold-plated leads from a commercially

available chip carrier (figure 4.3) and then implanting these leads into specially designed channels in the SLA parts.

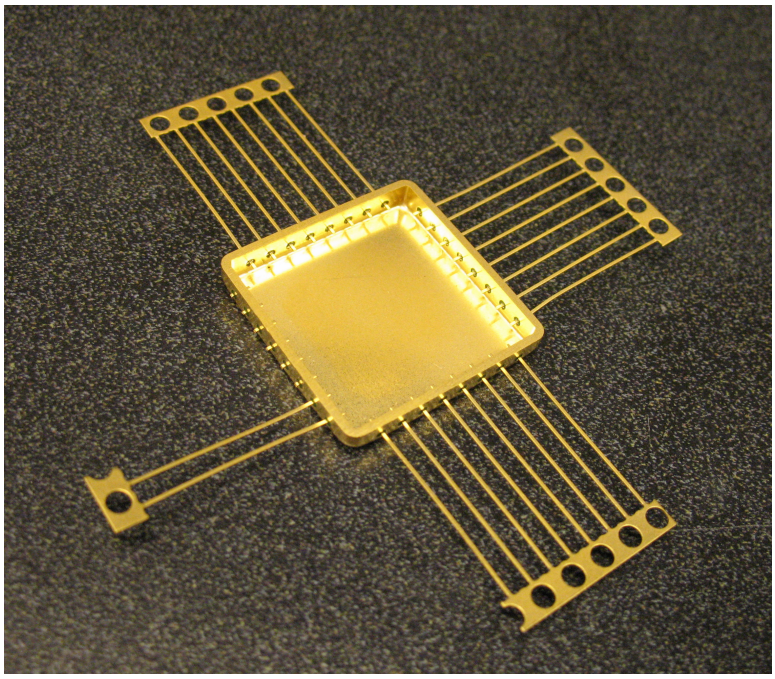

Figure 4.3 Gold-plated chip carrier

The cost of this option is minimal because a single commercial chip carrier provides enough gold leads to make several custom microphone packages. This method provides a great deal of design flexibility, which is highly desirable in the development of a functional prototype. The gold-plated leads provide a flat, conductive surface to which the optoelectronic devices can be connected via wire bonds. These leads are implanted in the SLA material and extend out of the package assembly. External connections are then required to connect the leads to the testing electronics. These connections were initially made with standard insulated hook-up wire, as shown in figure 4.4.

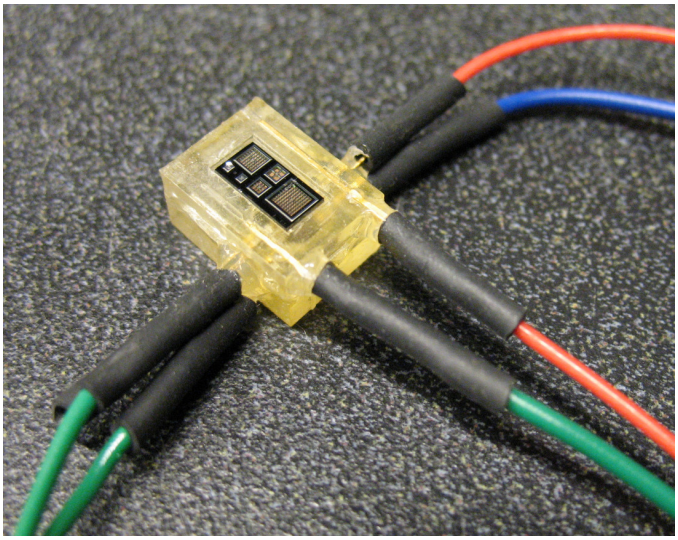

Figure 4.4 I/O Interface implemented in initial devices

The prototype devices implementing this approach eventually failed due to inadequate strain relief at the package interface. Stress placed on the electrical wires while handling/testing the device was transferred to the wire bonds via the gold-plated leads. To resolve this issue, later devices were built upon a standard 14-pin dual inline pin (DIP) carrier, as shown in figure 4.5.

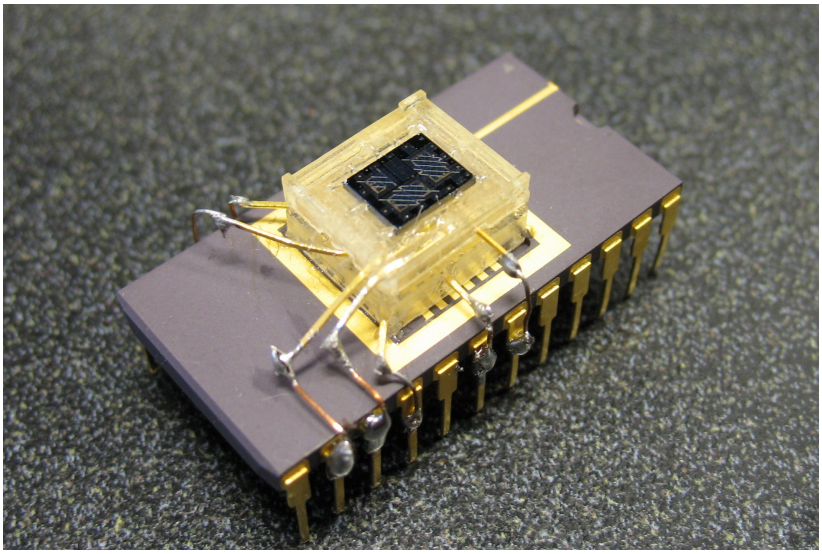

Figure 4.5 Integrated hearing aid microphone package mounted on DIP carrier

The gold-plated leads are connected to the leads on the DIP carrier by soldering thin-gage wire between the two. This effectively isolates the wire bonds from external stresses while providing a convenient platform upon which to build the prototype package. The assembled device can then be quickly connected to the test apparatus using a zero insertion force (ZIF) socket.

Adhesives

The use of adhesives was required for a wide range of applications in the assembly process. These adhesives were used to bond IC/MEMS chips to the SLA parts, secure electrical leads implanted in the SLA parts, electrically connect components, encapsulate wire bonds, and secure the SLA package components together. Three types of adhesives were implemented for these varied applications: Photosensitive UV-cured epoxy, conductive thermoplastic epoxy, and room-temperature-cured conductive epoxy.

Photosensitive UV-cured epoxy was used in applications where a fast, non-conductive bond was required. Because UV epoxy is cured by a short (<20 sec) exposure to UV light, it is ideal for bonding components which require accurate optical alignment. In such situations the epoxy is applied prior to alignment. Once the optical alignment has been verified, the epoxy is cured. Because the cure takes place quickly without the application of heat, the critical alignment of the components is maintained.

UV epoxies exhibiting a range of properties are available. A relatively soft UV epoxy was used in applications requiring a non-permanent bond. Such applications include fastening the photodiode chip and the microphone chip to the SLA package, bonding SLA parts together, and encapsulating wire bonds. The properties of this epoxy make it relatively easy to remove without damaging critical components. This is ideal in

a prototyping environment where components may be recycled multiple times. A stronger UV epoxy was used for permanent non-conductive bonds. This epoxy was used to secure the gold-plated electrical leads embedded in the package and to bond the microphone package to the DIP carrier.

Certain bonding applications required the use of a removable electrically conductive thermoplastic adhesive. When installing VCSELs with cathode connections on the substrate, for example, a conductive thermoplastic epoxy was used to bond the chips to a conductive lead. The curing process for this type of epoxy requires the application of heat for several minutes. This is less than ideal for two reasons. First, the SLA polymer begins to break down under excessive application of heat. Second, heating the assembly reflows any previously cured thermoplastic epoxy in the device, potentially shifting previously aligned components. To minimize damage to the SLA polymer, a low temperature thermoplastic conductive epoxy with a bonding range of 100-150°C was selected. The use of this epoxy was limited to situations that required a removable, electrically conductive bond.

A room temperature-cured conductive epoxy was used for permanent conductive bonds. The process of wire-bonding connections to the IC/MEMS chip can potentially result in damage to the devices and/or delamination of the bond pad. In such situations, the room temperature conductive epoxy was used to connect the ends of a bonding wire to the problematic bonding locations. This epoxy cures in approximately four hours at room temperature. This eliminates the risk of damaging the SLA material or reflowing previously cured components. This proved to be an effective method of electrically connecting certain VCSEL and biomimetic membrane chips.

Implementation of the methods outlined in this overview is presented in the subsequent sections of this chapter. The assembly and testing of each layer is described in detail, along with the integration of the three layers.

Assembly of Layer 1 – Photodiode Module

The microphone assembly process begins with the photodiode layer. The first step in the assembly of Layer 1 (as well as Layers 2 and 3) is to embed the gold-plated leads in the SLA part. The SLA parts have recessed channels that are specifically designed to hold the gold leads securely in place. The leads are secured using UV epoxy applied to the lead/channel interface. A short piece of copper wire is soldered to the end of each lead. The other end of this wire will later be soldered to the DIP carrier to connect the photodiode output signals to the test bed. This wire may be attached prior to installation of the gold lead in order to minimize damage to the epoxy or SLA part due to the high heat involved in the soldering process. A total of seven electrical leads are required for the photodiode module: one ground connection and six connections for the output signals.

The photodiode chip is secured in the appropriate recess in the SLA part using UV epoxy. The photodiode chip is installed after the interconnections in order to minimize the likelihood of damaging the device. Layer 1 is then mounted to a standard 14-pin DIP carrier using UV epoxy. The loose ends of the copper wires attached to the gold-plated leads are soldered to the corresponding pins on the DIP carrier. An image of the photodiode module installed on the DIP carrier is shown in figure 4.6.

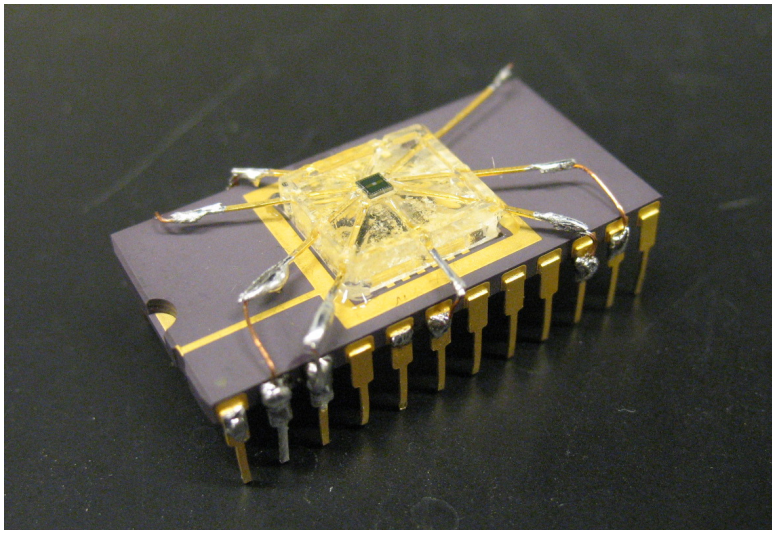

Figure 4.6 Layer 1 mounted on DIP carrier

The bond pads on the photodiode chip are then wire-bonded to the corresponding gold-plated leads. An image of the fully assembled photodiode module is shown in figure 4.7.

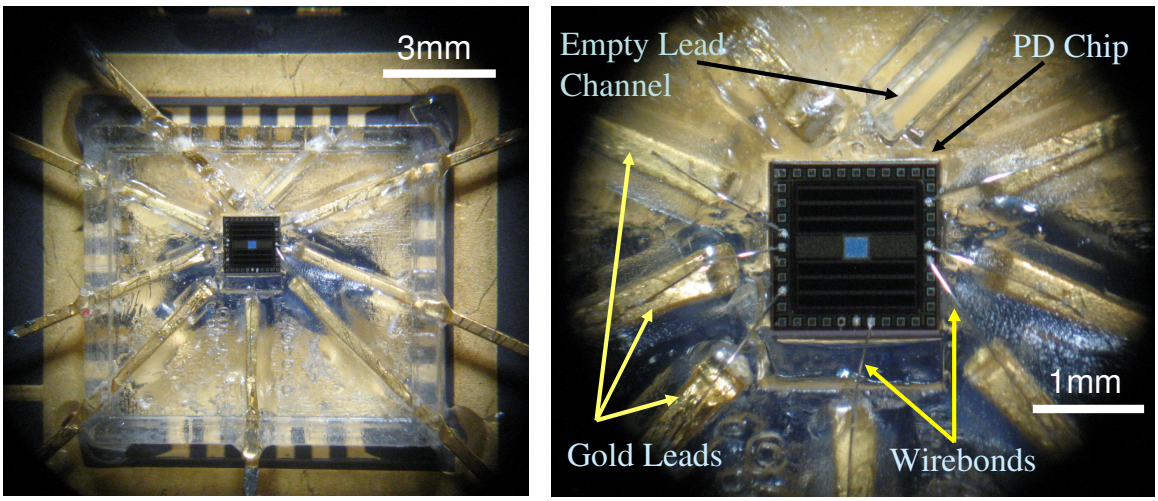

Figure 4.7 Fully assembled photodiode module

Note that the wire bonds are connected *after* the external connections have been soldered to the pins on the DIP package. The connections are made in this order to eliminate the possibility of damaging the wire bonds during the soldering step.

Layer 1 is tested to verify photodiode functionality. The package assembly is inserted into the ZIF socket on the test apparatus, which is described in the following chapter. The output signals are then connected to an oscilloscope via BNC cables. A variable light source is used to illuminate the photodiode cells with varying light intensities. The output of the device is monitored on the oscilloscope to verify that the photodiode assembly is functioning properly. The wire bonds are then encapsulated in UV epoxy.

Assembly of Layer 2 – VCSEL Module

The assembly of Layer 2 poses the greatest challenge of the three layers. Layer 2 houses the VCSEL chip, shown in figure 4.8.

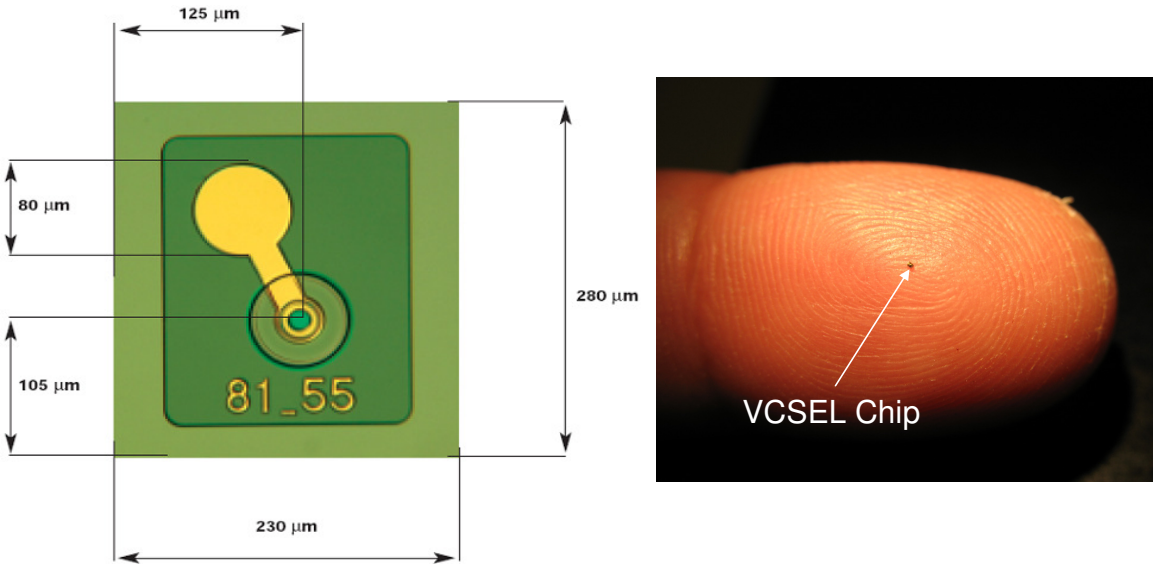

Figure 4.8 VCSEL chip

It is critical that the VCSEL is mounted securely and positioned accurately in order for the device to function properly. This must be done manually using a pair of tweezers.

Wire-bonding the anode pad on the VCSEL chips is also challenging due to the fragile nature of the chip and bond pad metallization.

The electrical leads are installed in Layer 2 in the same manner as Layer 1. Layer 2 requires two leads to power the VCSEL. The anode pad is located on the top of the chip, while cathode pad is located on the bottom of the substrate. The cathode connection is made by bonding the VCSEL directly to the cathode lead using conductive epoxy, as shown in figure 4.9.

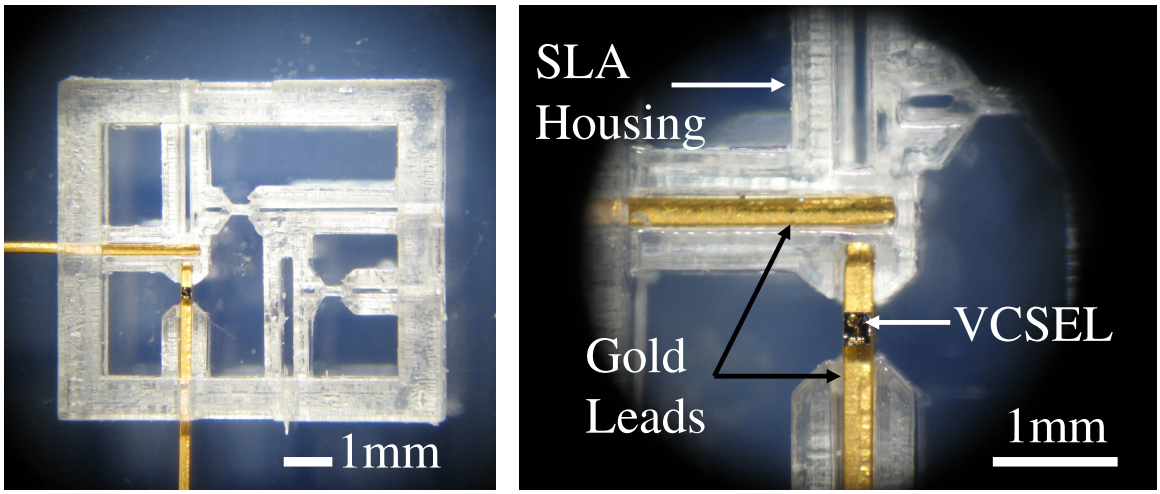

Figure 4.9 VCSEL mounted on gold-plated lead embedded in Layer 2

The gold plating may not be completely uniform in the location that the VCSEL will be mounted. To eliminate any potential misalignment caused by such an aberration, the gold plating can be removed from the part of the lead where the VCSEL will be mounted, thereby exposing the flat copper core. The package is designed to hold the cathode lead securely in the proper orientation. The rigid positioning of these leads is provided by tight tolerances in the lead channels. This ensures that VCSEL can be mounted level relative to the package assembly.

The epoxy is cured by heating Layer 2 on a hotplate. The temperature is slowly increased to the bonding range, and the device is covered with an aluminum box in order to promote uniform heating. The temperature is monitored using a multimeter equipped with a thermocouple. When the temperature reaches the middle of the curing range (125°C), the hotplate is turned off. Heating the SLA polymer above this point may result in deformation and discoloration. The part is left on the hotplate (covered by the aluminum box) until it returns to ambient temperature. This maintains a temperature within the curing range after the power is disconnected, which allows the epoxy sufficient time to cure before the assembly is disturbed. Layer 2 is then inspected under the microscope to verify proper mounting.

The anode pad is wire-bonded to the corresponding gold-plated lead and the wire bond is encapsulated in epoxy, as shown in figure 4.10.

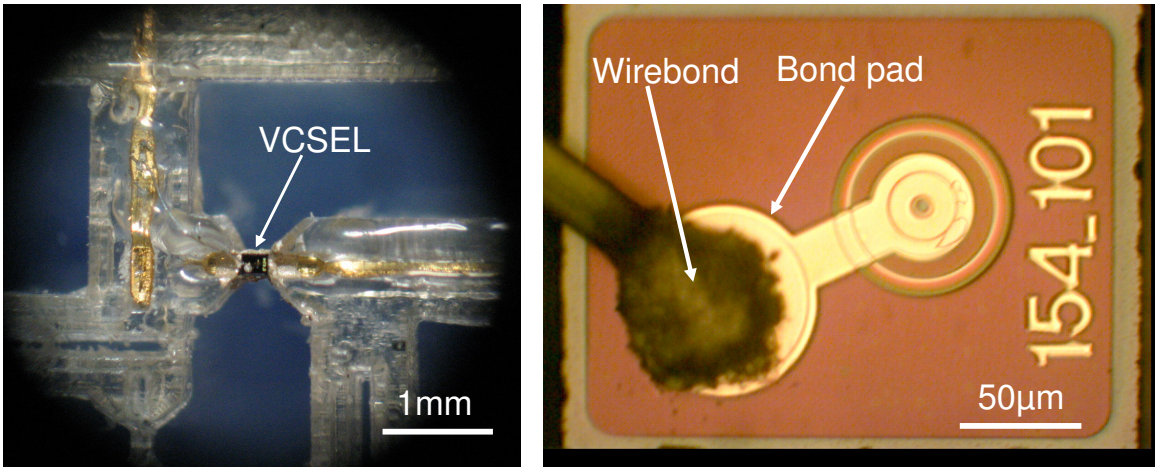

Figure 4.10 Wire-bonded VCSEL

Alternatively, a small amount of conductive epoxy can used to bond the ends of a bond wire to the VCSEL anode pad and corresponding gold-plated lead. This is a useful method when wire-bonding proves difficult.

The VCSEL is tested to verify that the bonding steps were successful and that the device is functional. Due to the optical power of the device, direct viewing of the VCSEL beam can cause vision damage. Furthermore, the VCSEL emits light with a wavelength of 850nm, which renders it invisible to the human eye. These obstacles are circumvented by coupling an infrared CCD camera to a high power microscope. The camera relays live video feed of the sample to a computer screen. The functionality of the VCSEL can then be verified by powering the device under the microscope objective and monitoring the light output on the computer screen. Figure 4.11 shows an infrared image of a VCSEL operating at 0.8mA (left) and near threshold (right).

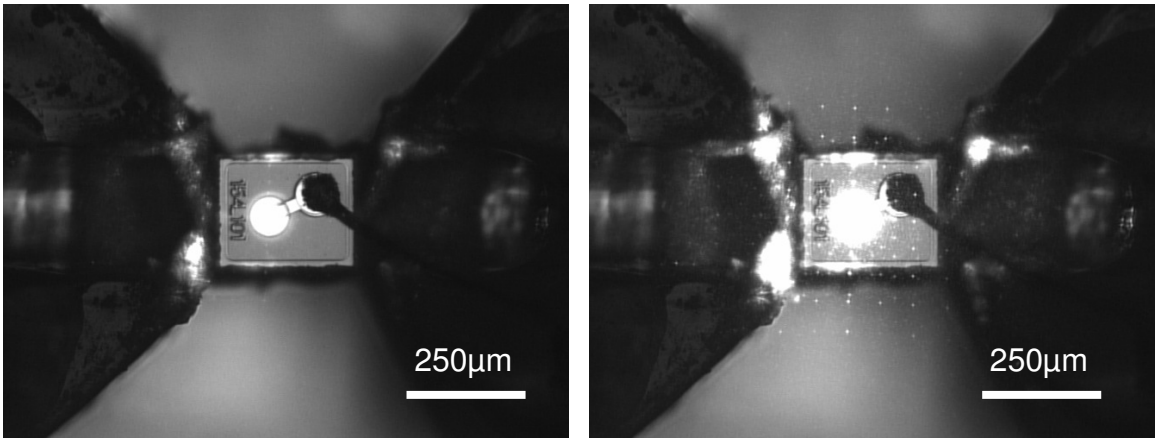

Figure 4.11 Operating VCSEL viewed through infrared camera

Any fluctuations in light intensity indicate that the VCSEL is defective or that one of the two bonds is not secure.

Once the functionality of the VCSEL is verified, the photodiode and VCSEL modules are connected, as shown in figure 4.12.

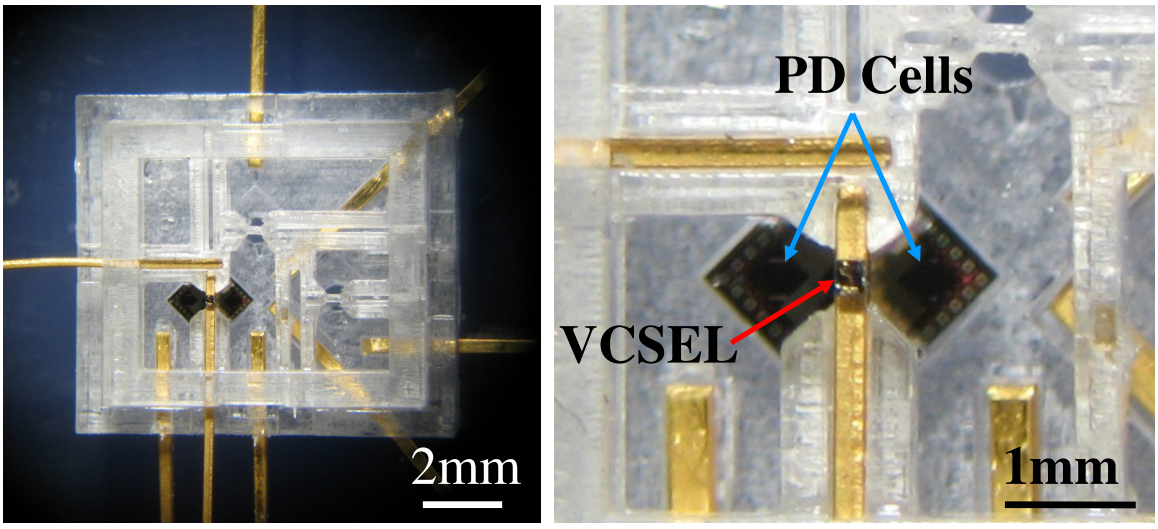

Figure 4.12 VCSEL aligned with photodiode chip

For illustration purposes, this figure shows a package assembly which implements the 3-cell photodiode array described in Chapter 3. UV epoxy is applied at the interface of two layers. The VCSEL is powered on and the alignment of the lasing spot and the photodiode array is verified using the infrared CCD camera coupled to the microscope. If the VCSEL is tilted relative to the package, the beam spot will be noticeably off-center relative to the photodiode array. A properly aligned VCSEL/photodiode assembly is shown in figure 4.13

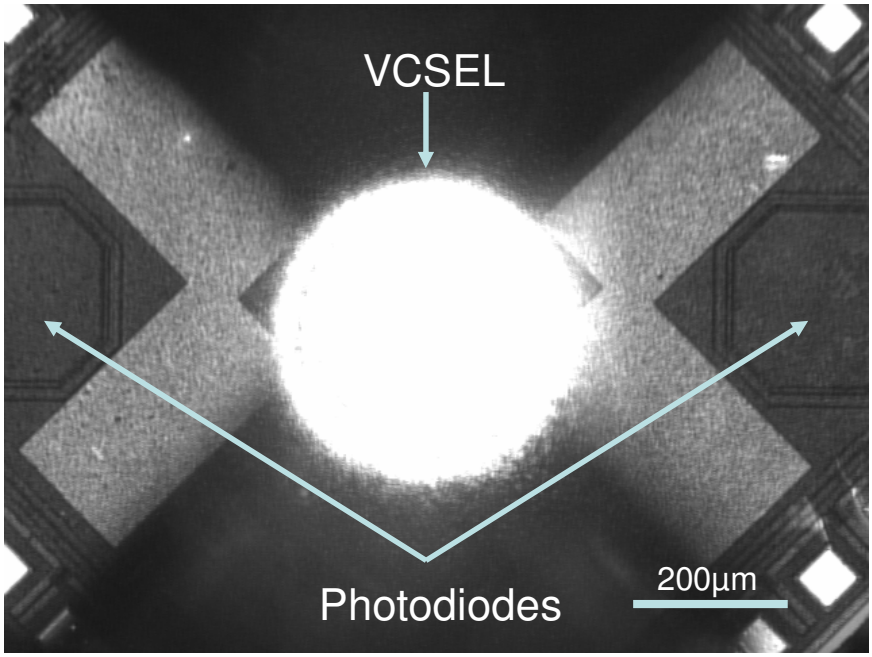

Figure 4.13 Infrared image of operating VCSEL aligned with photodiodes

It is critical to use a microscope with direct line-of-sight to the sample in order to avoid parallax issues. Once the optical alignment is verified, the assembly is exposed to UV light to cure the epoxy and bond the two layers together.

Assembly of Layer 3 – Biomimetic Membrane Module

Layer 3 requires two connections to bias the microphone membrane. The process of embedding the leads into the SLA part (figure 4.14) is identical to Layers 1 and 2. After installing the electrical leads, Layer 3 is mounted to the detection assembly and secured using UV epoxy. The electrical leads are then connected to the appropriate pins on the DIP carrier. As illustrated in figure 4.15, all of the components have been installed at this point except the biomimetic membrane chip.

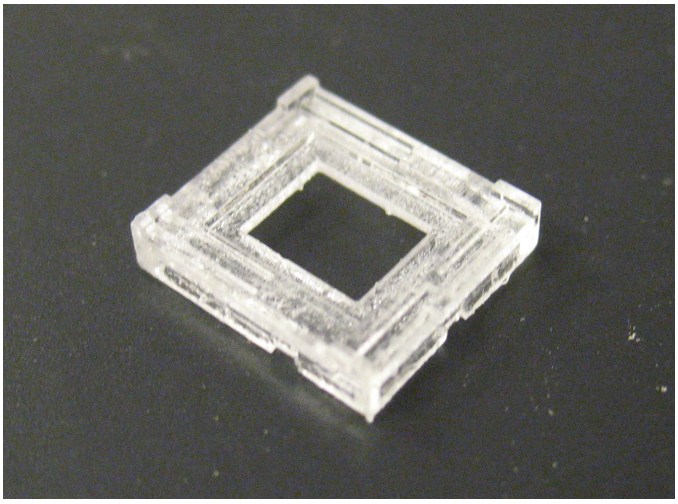

Figure 4.14 Layer 3 of microphone package

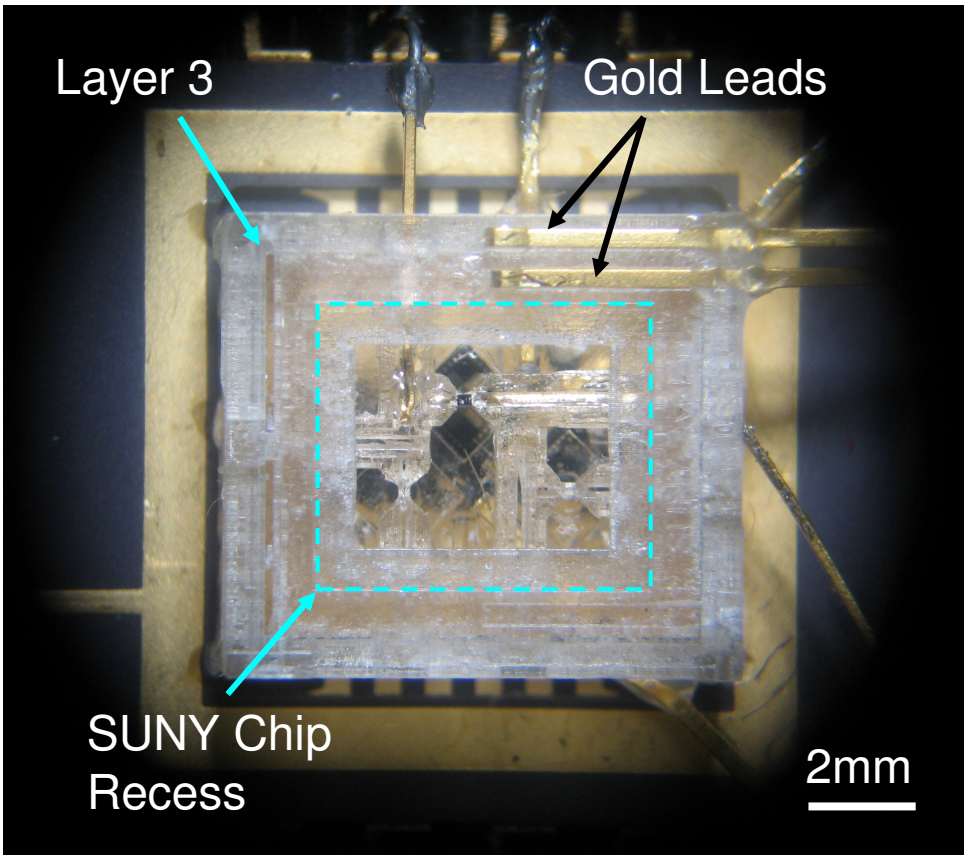

Figure 4.15 Layer 3 mounted on package assembly

Accurate alignment of the biomimetic membrane chip with the detection optoelectronics is critical to the performance of the microphone. The chip must be mounted such that the 100µm wide diffraction grating is precisely aligned with the 300µm wide infrared beam spot illuminated from 1.2mm below. The alignment is performed manually with the aid of the infrared CCD camera coupled to the microscope, as shown in figure 4.16.

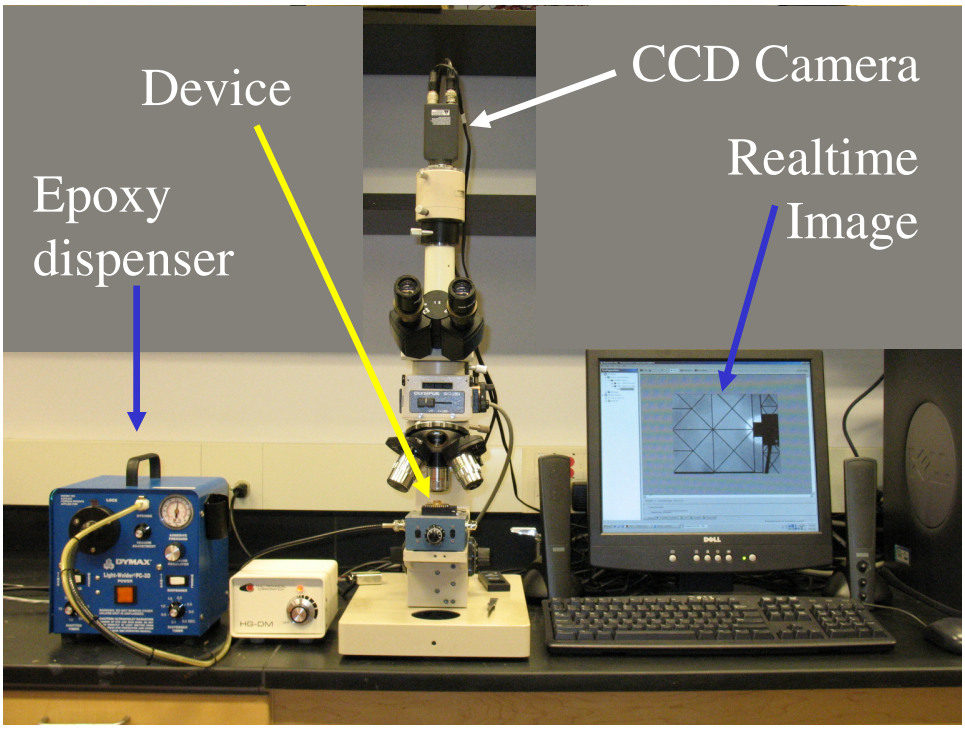

Figure 4.16 Optical alignment setup

UV epoxy is applied at the interface between the chip and the package prior to alignment. The epoxy will be cured once the chip is properly aligned. The VCSEL is powered on, projecting a beam spot onto the bottom of the membrane chip. The microphone membrane is only 1µm thick, which renders it translucent. The VCSEL beam spot can therefore be seen through the membrane. The SUNY chip is manipulated with tweezers

while the process is monitored on the computer screen. In order to optimize the performance of the microphone, a speaker driven at the resonance frequency of the membrane provides an acoustic input which can be used to pinpoint the optimal alignment location. The output signal of the microphone is monitored as the alignment of the biomimetic membrane chip is adjusted. When the diffraction grating and detection optoelectronics are perfectly aligned, the AC amplitude of the photodiode output signal will be maximized and the DC level will be minimized. The package is then exposed to UV light to cure the epoxy and secure the chip in place. An optimally aligned microphone is shown in figure 4.17.

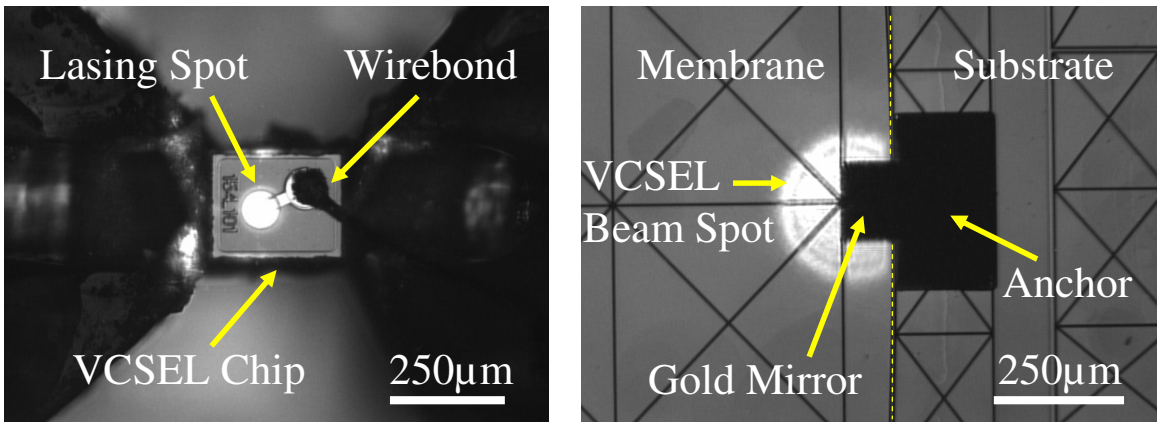

Figure 4.17 Infrared image of properly aligned microphone

The electrical leads are then soldered to the appropriate pin on the DIP carrier.

The final step in the assembly process is to electrically connect the electrostatic ports on the microphone membrane to the corresponding leads in the package. The bond pads on the biomimetic membrane chip are wire-bonded to the appropriate gold leads, as shown in figure 4.18.

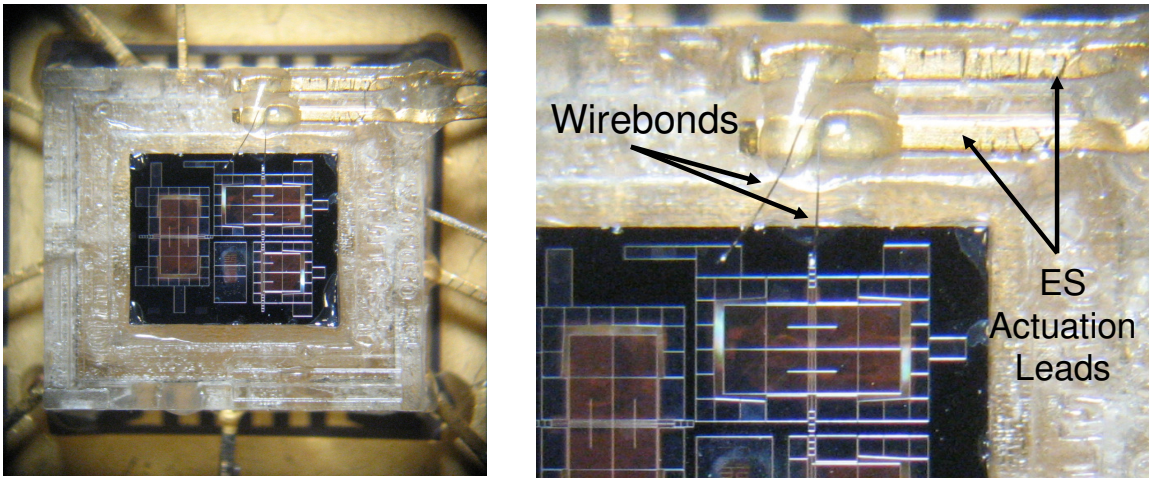

Figure 4.18 Electrostatic actuation ports connected with wire bonds

The device shown in figure 4.18 is a preliminary chip design which implemented an interdigital grating. For the device characterized in this work, the anchor of the gold mirror doubles as the substrate electrode. It is extremely difficult to wire-bond the gold anchor without damaging the device. For this reason the connection is made by manually bonding a wire to the bond pad using conductive epoxy, as shown in figure 4.19.

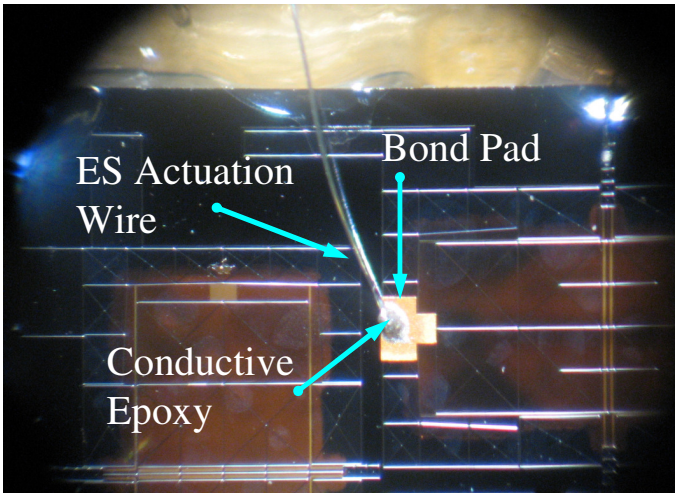

Figure 4.19 Electrostatic actuation wire connected with conducted epoxy

The other end of the wire is secured to the appropriate electrical lead in the same manner. The package is then left to cure undisturbed for at least 4 hours. This completes the assembly of the integrated hearing aid microphone.

Once the device has been fully assembled, tests are performed to verify basic functionality of the integrated microphone. A speaker driven by a function generator is used to produce various audio signals. The VCSEL is powered on, and the amplified output of microphone is monitored on an oscilloscope. The electrostatic bias on the membrane is modulated in order to verify sensitivity tuning capability. Once basic operation has been verified, the wire bonds are encapsulated in UV epoxy. The device is then ready for detailed characterization, as described in the following chapter.

Full Miniaturization

In order to demonstrate the potential for implementation of the integrated microphone in hearing aid applications, the DIP carrier was replaced by a custom designed printed circuit board (PCB) shown in figure 4.20.

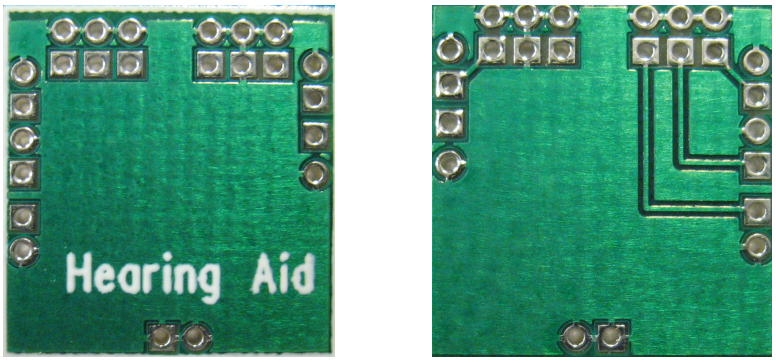

Figure 4.20 PCB for miniaturized hearing aid microphone

This PCB provides connection points for the external I/O pins of the package. These signals are routed to a central location on the perimeter of the PCB. The package is mounted directly on the PCB using UV epoxy. Thin shielded cables are then used to connect the I/O pads to the test bed. The fully miniaturized biomimetic hearing aid microphone is shown in figure 4.21.

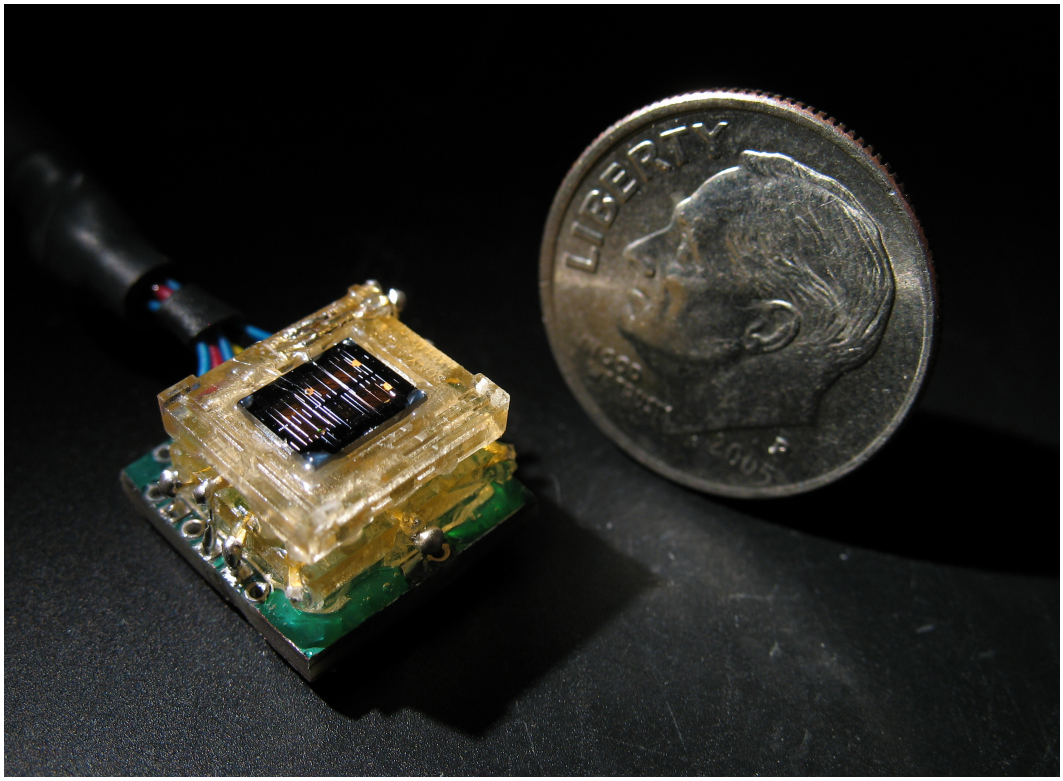

Figure 4.21 Fully miniaturized hearing aid microphone

While the device was not re-characterized in this configuration, it demonstrates the potential for implementation in a standard hearing aid form factor.

CHAPTER 5

DEVICE CHARACTERIZATION

Detailed testing of the integrated hearing aid microphone was conducted in order to characterize the performance of the device. These tests include measurements of optical intensity curves, frequency response, noise floor, and directivity. As with the measurements presented in Chapter 2, the acoustic tests were conducted in an anechoic chamber in order to simulate a free field environment. The experimental methods and results associated with the characterization of the device are presented in this chapter.

Compact Test Bed

A compact test bed was designed and constructed to serve as an interface between the packaged microphones and the various test apparatus. The test bed, shown in figure 5.1, provides a convenient, flexible, robust, and portable platform through which I/O and power connections to the devices can be made.

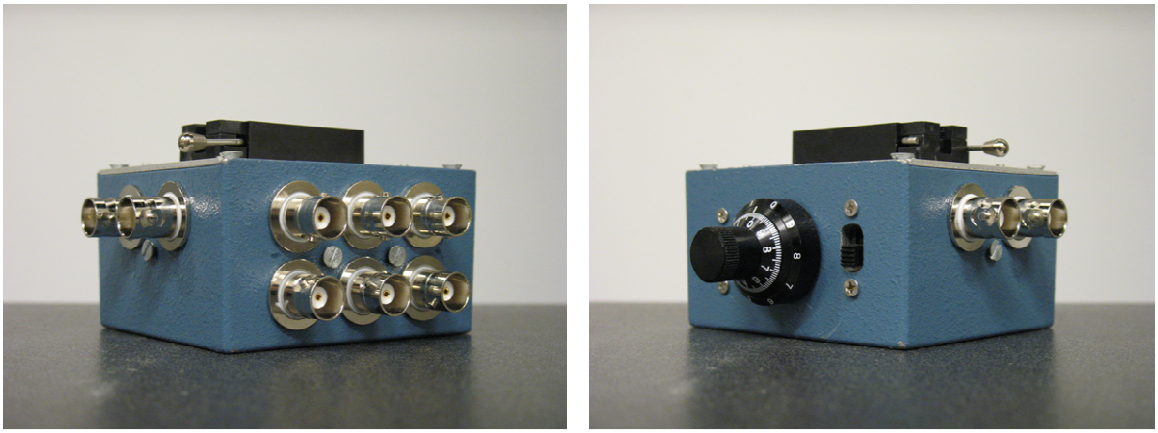

Figure 5.1 Compact test bed for integrated hearing aid microphone

The packaged microphone is connected to the test bed via a Zero Insertion Force (ZIF) socket, as shown in figure 5.2. A schematic representation of the components of the test bed is shown in figure 5.3.

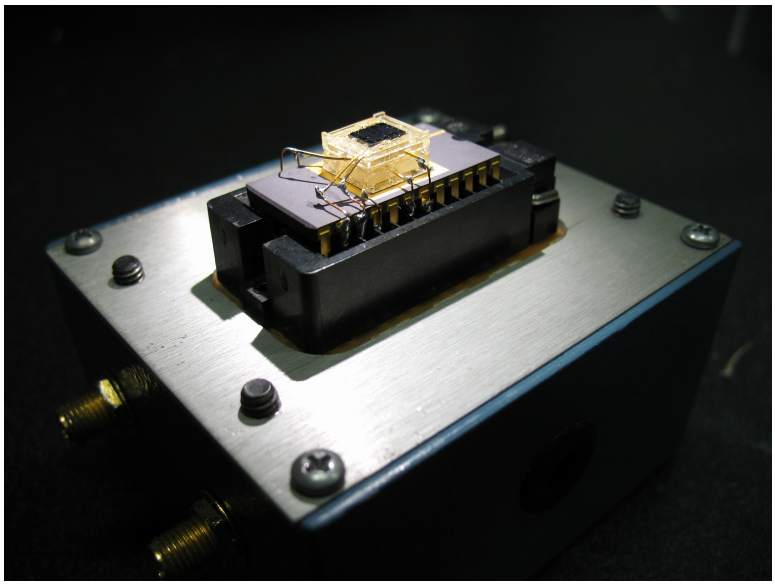

Figure 5.2 Integrated hearing aid microphone connected to test bed via ZIF socket

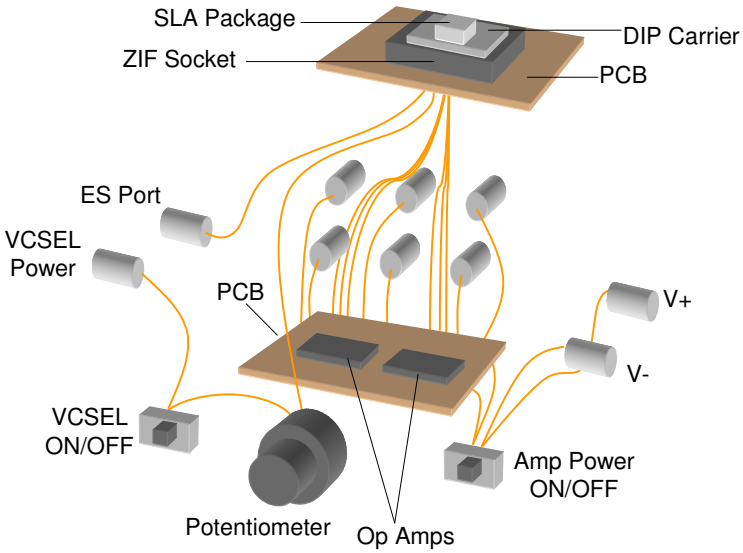

Figure 5.3 Components of microphone test bed

Panel-mount BNC connectors provide connections for the VCSEL power input, electrostatic actuation signal, and six amplified output signals. A precision 10-turn potentiometer regulates the current through the VCSEL, which is powered by a 9V battery. Two standard operational amplifiers are mounted to a second PCB via 14-pin IC sockets. The Op Amps are also powered by 9V batteries. On/Off switches are built in for both the VCSEL and amplifier power. The electrical signals are routed between the various connectors and components within the test bed via shielded cables. The shielded cables, together with the aluminum box, serve to minimize external and internal interference.

Optical Intensity Curves

The experimental setup for measurement of the optical intensity curves is illustrated in figure 5.4.

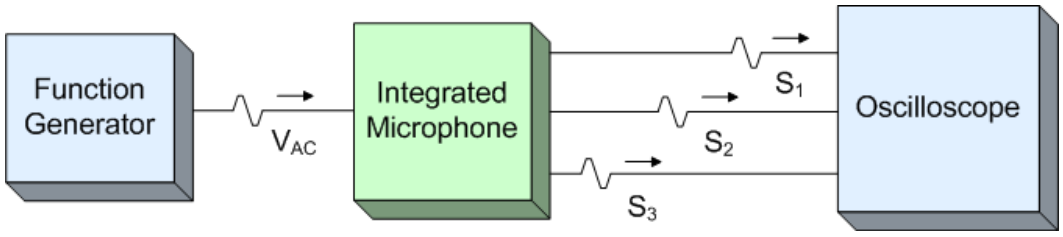

Figure 5.4 Test setup for measurement of optical intensity curves

The optical intensity curves of the integrated hearing aid microphone are measured in a similar manner as those measured using the prototype test bed presented in Chapter 2. A low frequency (10Hz) voltage ramp signal is applied to the electrostatic actuation ports of the microphone using a function generator. The resulting output signals are measured using an oscilloscope and plotted as a function of input voltage. While the integrated

microphone outputs a total of six signals, the quality of the three 0^{th} order signals was very poor due to the obstruction posed by the VCSEL. These signals were therefore not used for characterization. The three photodiodes used to measure the 1^{st} order beam are referred to as PD1, PD2, and PD3. The corresponding signals are denoted S_1, S_2, and S_3, respectively. Intensity curves for the PD1, PD2, and PD3 signals are shown in figures 5.5, 5.6, and 5.7, respectively.

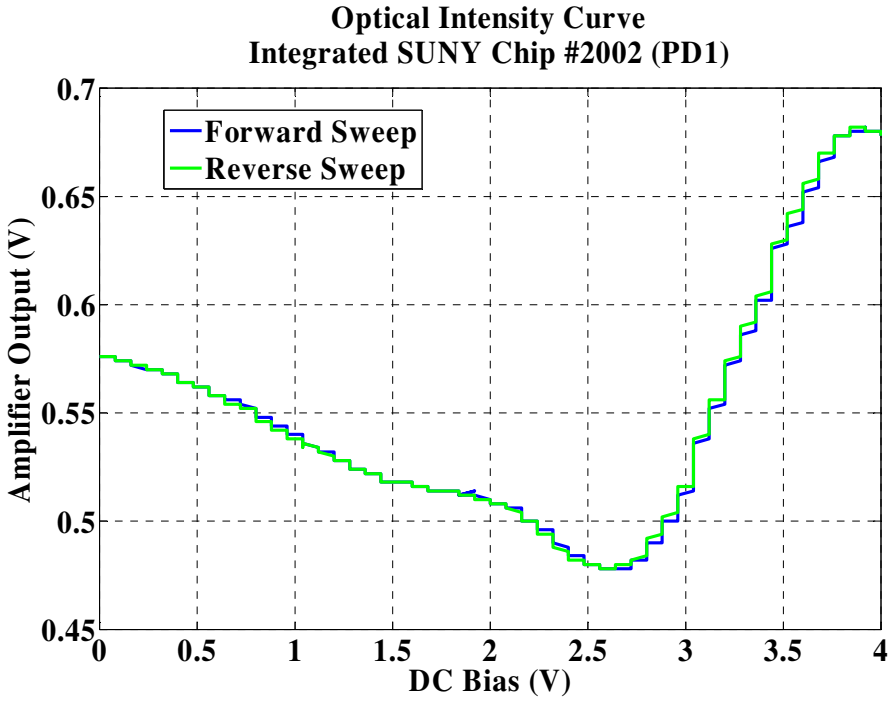

Figure5.5 PD1optical intensity curve

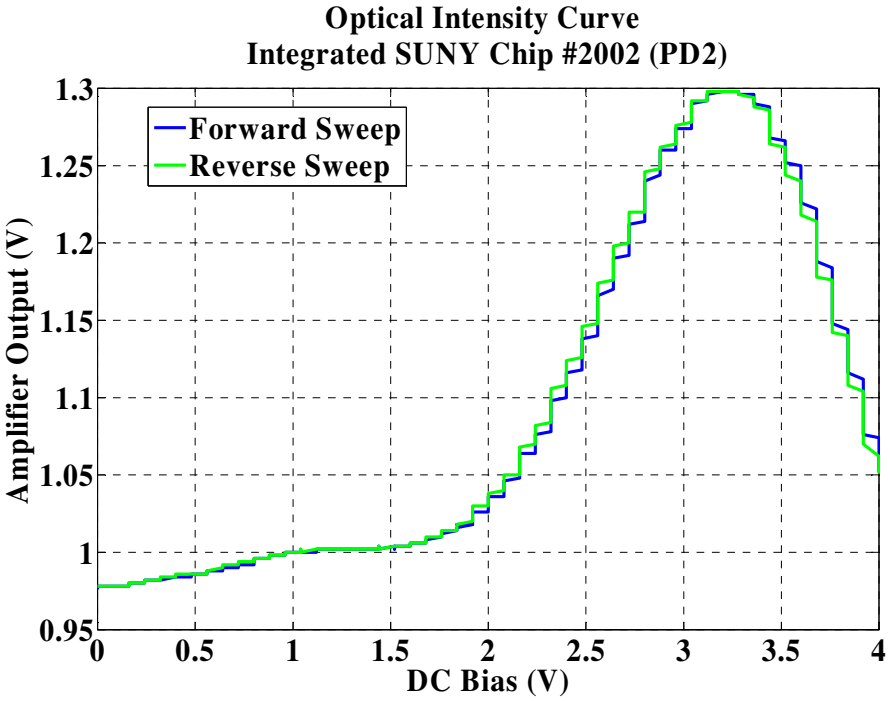

Figure 5.6 PD2 optical intensity curve

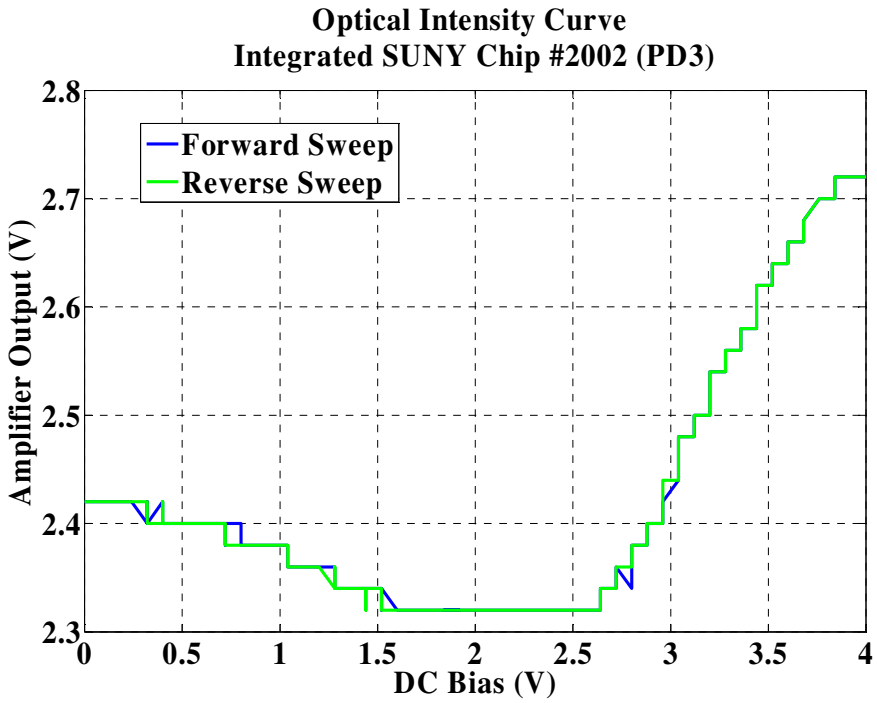

Figure 5.7 PD3 optical intensity curve

There are two noteworthy differences between the theoretical and measured intensity curves. First, the measured intensity curves do not follow the sinusoidal form shown in figure 1.5. The measured curves are obtained as a function of DC bias voltage rather than membrane deflection. There is a non-linear relationship between the applied bias and deflection of the membrane, which is why the measured curves appear distorted. Second, the minimum value of the measured intensity curves is non-zero. This is a result of the divergence of the incident beam which leads to optical losses and overlap of the orders.

The electrical sensitivities and modulation efficiencies for the three output signals are listed in table 5.1.

Table 5.1 Performance metrics for measured signals

	V_{DC}(V)	Vpp(V)	S_e(V/μm)	ηmod(%)	SPL(dBA)
PD1	0.580	0.204	1.508	29.9	36.1
PD2	1.150	0.296	2.188	22.8	35.9
PD3	2.520	0.400	2.957	14.7	>>36dBA

V_{DC} and V_{PP} are the DC and AC signal levels obtained from the optical intensity curves. S_e is the sensitivity as calculated by equation 1.16. η_{mod} is the modulation efficiency calculated by equation 3.6. SPL is the noise sound pressure level, the methods of obtaining which are discussed subsequently. Note that the SPL for PD3 was not calculated due to the significantly higher noise floor relative to the other two channels. It can be assumed that the SPL of PD3 is much greater than 36dBA. The data in table 5.1

verifies the inverse relationship between sensitivity and modulation efficiency as predicted by the optical simulations described in Chapter 3. Furthermore, it was expected that the signal with lowest noise SPL would be measured by PD2, which is indeed the case. This signal is utilized for all subsequent measurements presented this chapter.

Frequency Response

The frequency response to both acoustic and electrostatic actuation was measured in an anechoic test chamber. These frequency response measurements were conducted in a similar manner as those presented in Chapter 2. The test setup for measurement of the electrostatic frequency response is illustrated in figure 5.8

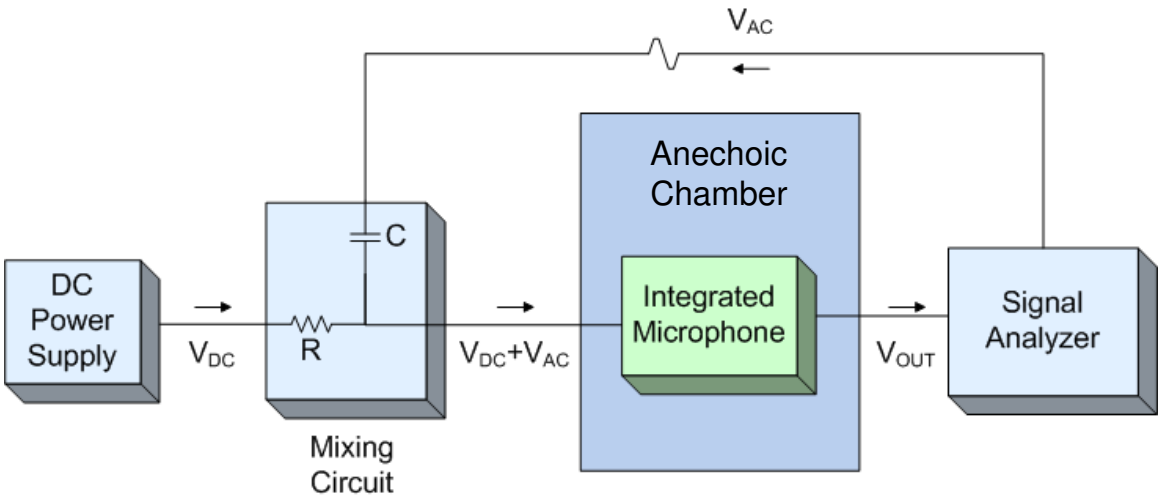

Figure 5.8 Test setup for measurement of electrostatic frequency response

A chirp signal is generated using an SRS dynamic signal analyzer. This signal is combined with the DC bias voltage using a mixing circuit. The combined signal is then applied to the electrostatic actuation ports on the microphone. The resulting microphone

output signal is measured by the signal analyzer which calculates the frequency response, shown in figure 5.9.

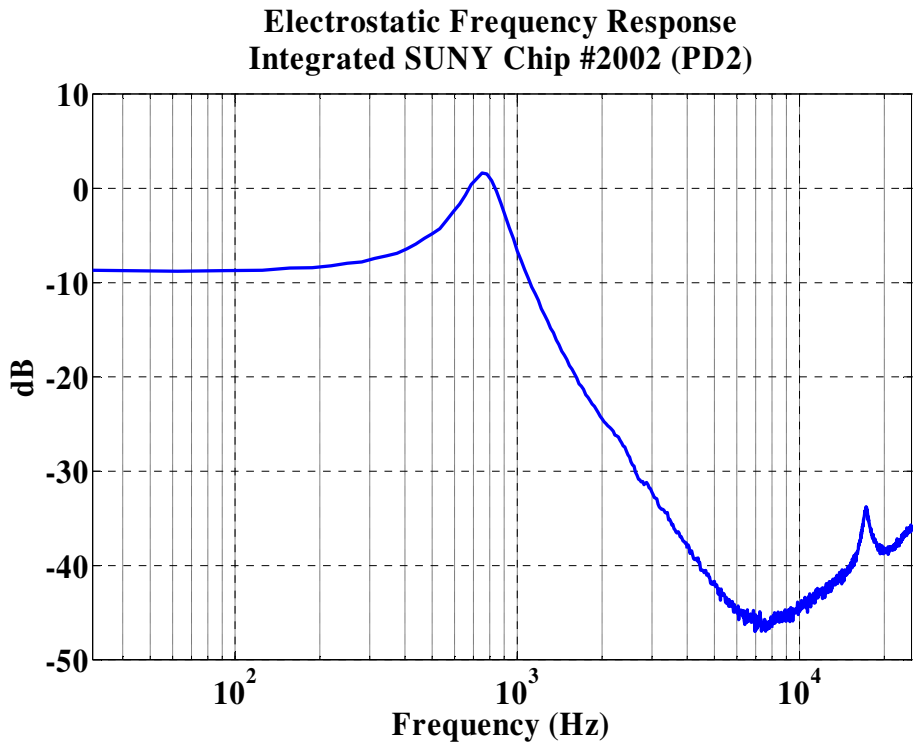

Figure 5.9 Electrostatic frequency response of integrated hearing aid microphone

The rotational and translational mode natural frequencies can be seen at 750Hz and 17220Hz, respectively. These results agree with measurements taken by the fabrication team using a laser vibrometer.

The test setup for measurement of the acoustic frequency response is illustrated in figure 5.10.

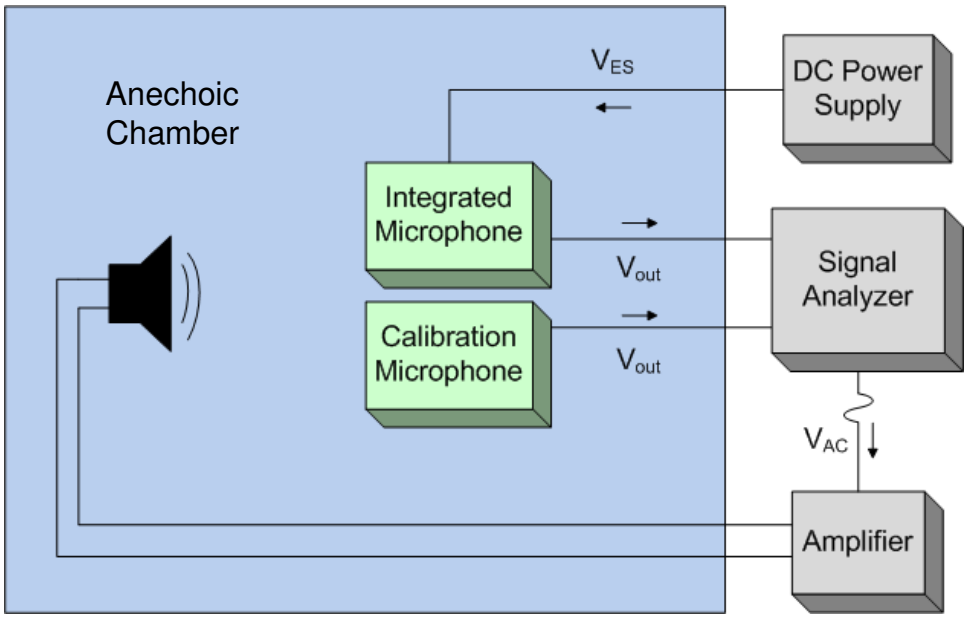

Figure 5.10 Test setup for measurement of acoustic frequency response

A chirp signal is generated using the SRS dynamic signal analyzer. This signal is amplified and fed to a Yamaha NS-6490 3-way speaker. A DC power supply is used to bias the membrane to the point of maximum sensitivity as determined from the optical intensity curves. The output of the microphone is recorded by the signal analyzer. A ½" Larson Davis model 2541 microphone, which has a relatively flat response and a known sensitivity of 0.04V/Pa, is used to measure the acoustic input signal. The data recorded by the integrated SUNY microphone is divided by the Larson Davis calibration data in order to obtain the acoustic frequency response in units of V/Pa, as shown in figure 5.11.

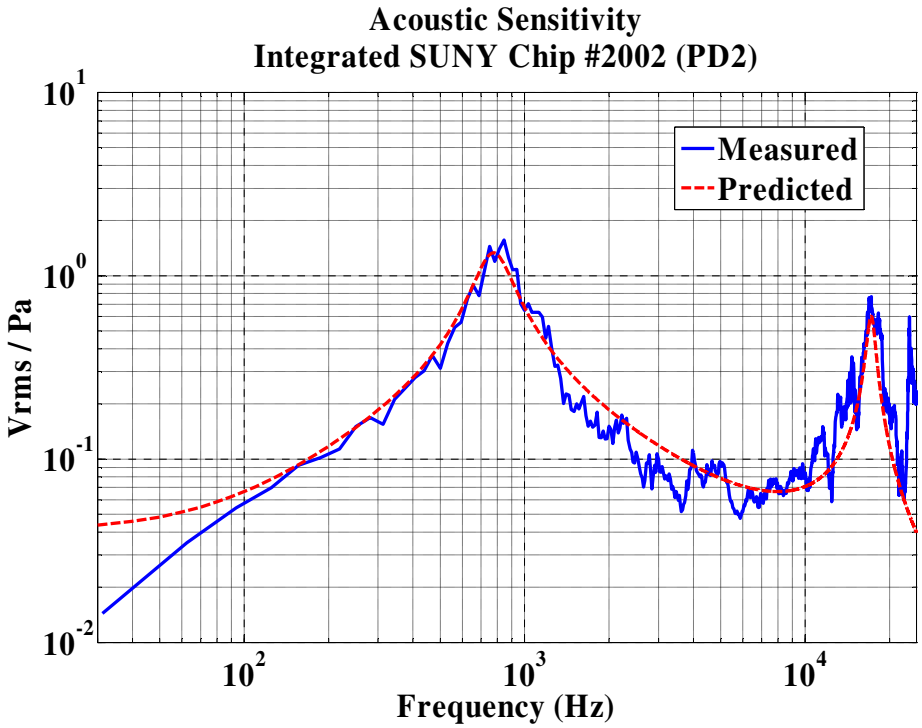

Figure 5.11 Measured and predicted acoustic frequency response of integrated hearing aid microphone

An analytical model which predicts the acoustic response and thermo-mechanical noise spectrum of the SUNY biomimetic membrane was presented in [20]. The acoustic response predicted by this model is shown in figure 5.11 along with the measured data. The measured data shows a close fit to the theoretical response, with a rotational mode natural frequency of 750Hz and a translational mode natural frequency of 17.22kHz. These natural frequencies match those obtained from electrostatic frequency response data and the laser vibrometer measurements. The maximum sensitivity of the device is 1.5V/Pa @ 750Hz, with a minimum sensitivity of 0.05V/Pa across the majority of the audio range.

Noise Performance

Noise measurements are conducted using the same experimental setup as the acoustic frequency response test depicted in figure 5.10. For the noise tests, however, the amplifier, speaker, and calibration microphone are not used. The voltage noise spectrum of the integrated hearing aid microphone is measured in the absence of acoustic input using the SRS signal analyzer. The theoretical voltage noise spectrum is calculated using the analytical model presented in [20]. The measured and predicted noise spectra are shown in figure 5.12.

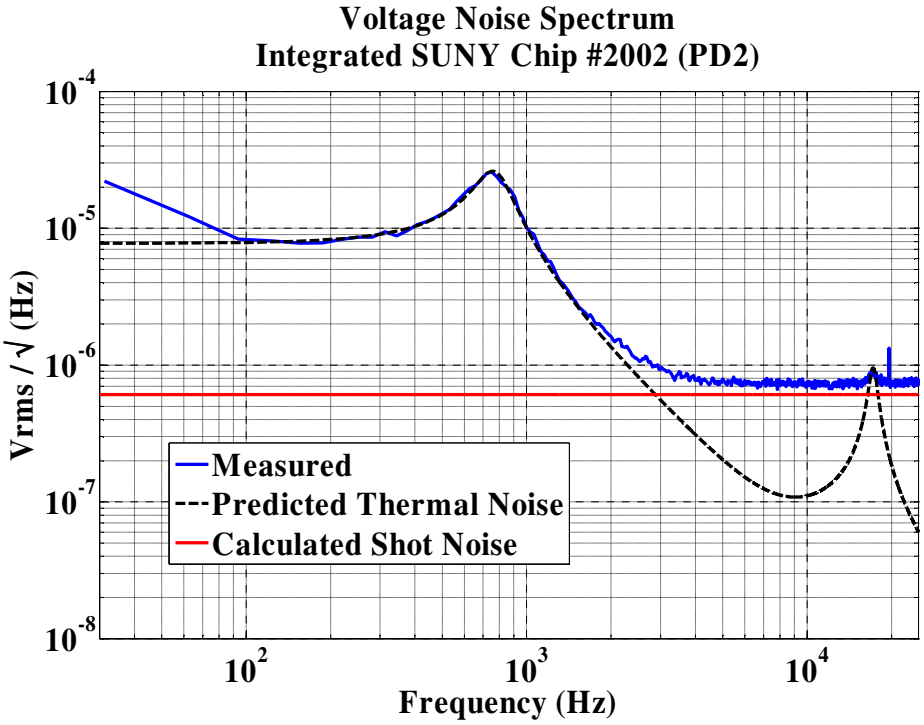

Figure 5.12 Measured and predicted voltage noise spectra of integrated hearing aid microphone

Also shown in this figure is the calculated voltage shot noise, given by

$$V_{shot} = \sqrt{2qR_{fb}V_{DC}} \tag{5.1}$$

where q is the elementary charge (1.6×10^{-19}C), R_{fb} is the TIA gain (1MΩ), and V_{DC} is the DC voltage level obtained from the optical intensity curve in figure 5.6. The measured data shows a close fit to the predicted thermal noise spectrum between 100Hz and 3kHz, indicating that the device is thermal-noise limited in this frequency range. The discrepancy between the measured noise and the predicted thermal noise below 100Hz is attributed to the dominance of 1/f noise at low frequencies. Above 3kHz, the measured data closely approaches the shot noise limit of 6×10^{-7}Vrms/√Hz. The discrepancy between the measured noise floor and the calculated shot noise level is attributed to laser intensity noise.

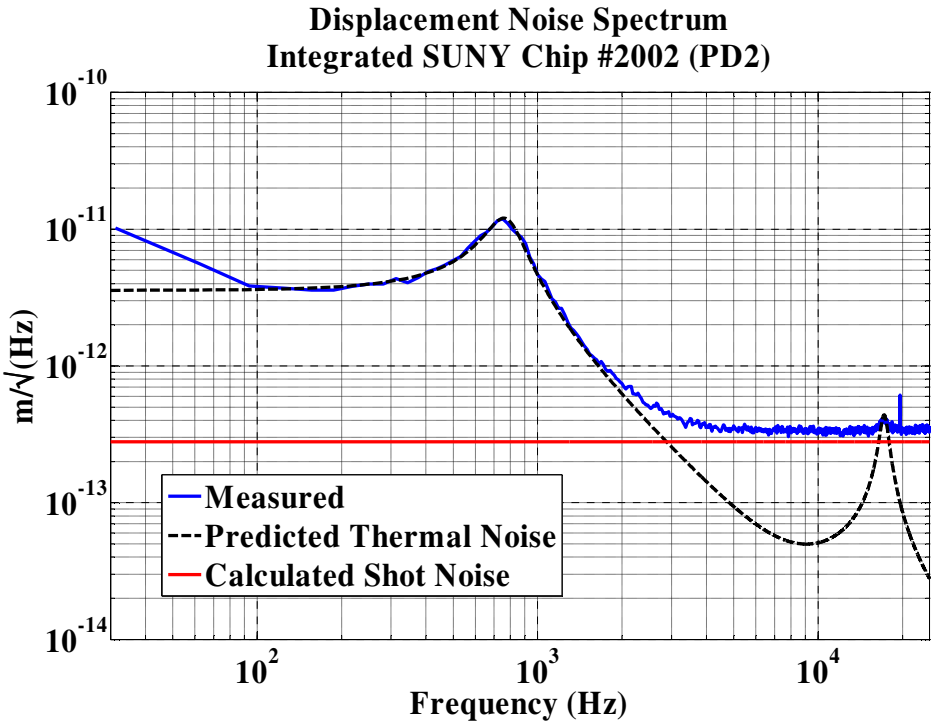

Figure 5.13 Measured and predicted displacement noise spectra of integrated hearing aid microphone

A more useful representation of this data is the equivalent displacement noise spectrum, shown in figure 5.13. This is calculated by dividing the voltage noise spectrum

shown in figure 5.12 by the displacement sensitivity calculated from the optical intensity curves. This data indicates a displacement resolution of 3.5×10^{-13} m/√Hz between 4kHz and 16kHz. This approaches the theoretical shot noise limit of 2.8×10^{-13} m/√Hz calculated by equation 5.1. The displacement noise floor defines the lower limit for the dynamic range of the device. The upper limit is given by λ/4, as derived from the optical intensity curves described in Chapter 1. The VCSELs integrated in this work emit light with a wavelength of 850nm, which corresponds to a maximum detectable signal of 212.5nm. The dynamic range of the microphone is therefore115dB.

To obtain the equivalent pressure noise spectrum of the integrated SUNY microphone, the measured voltage noise spectrum (figure5.12) is divided by the acoustic sensitivity (figure 5.11). The resulting pressure noise spectrum is shown in figure 5.14, along with the theoretical pressure noise spectrum predicted by the analytical model.

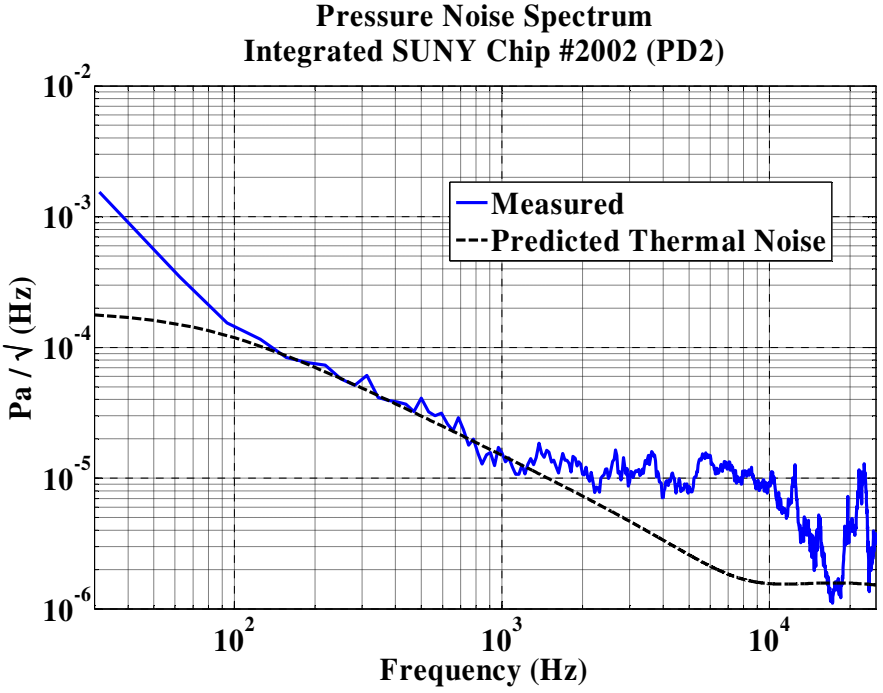

Figure 5.14 Measured and predicted pressure noise spectra of integrated hearing aid microphone

This data indicates a pressure noise floor of 1.6×10^{-5} Pa/√Hz @ 1kHz. In order to calculate the noise sound pressure level (SPL) of the device, the pressure noise spectrum (figure 5.14) is multiplied by the standard A-weighting filter (figure 2.12), which approximates the sensitivity of the human ear. The resulting A-weighted pressure noise power spectrum is shown in figure 5.15.

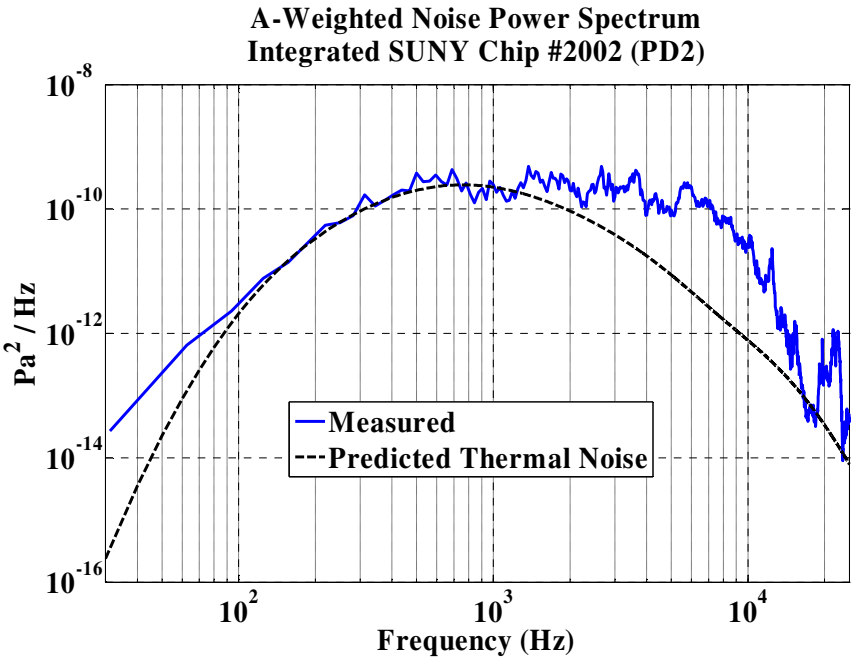

Figure 5.15 Measured and predicted A-weighted noise power spectra of integrated hearing aid microphone

The SPL of the microphone is calculated by integration of the A-weighted noise power spectrum. The measured noise SPL of the fully integrated microphone (chip # 2002) is 35.9dBA. The predicted thermal Noise SPL of the integrated microphone is 30.3dBA. The discrepancy between the measured and predicted values is attributed to the dominance of 1/f noise below 100Hz and laser intensity noise above 3kHz.

Directivity

A variation of the *free field method* described in Chapter 1 was implemented in order to characterize the directivity of the integrated hearing aid microphone. Rather than rotating the acoustic source about the microphone, the source is held in a fixed location while the microphone is rotated about its vertical axis, as illustrated in figure 5.16

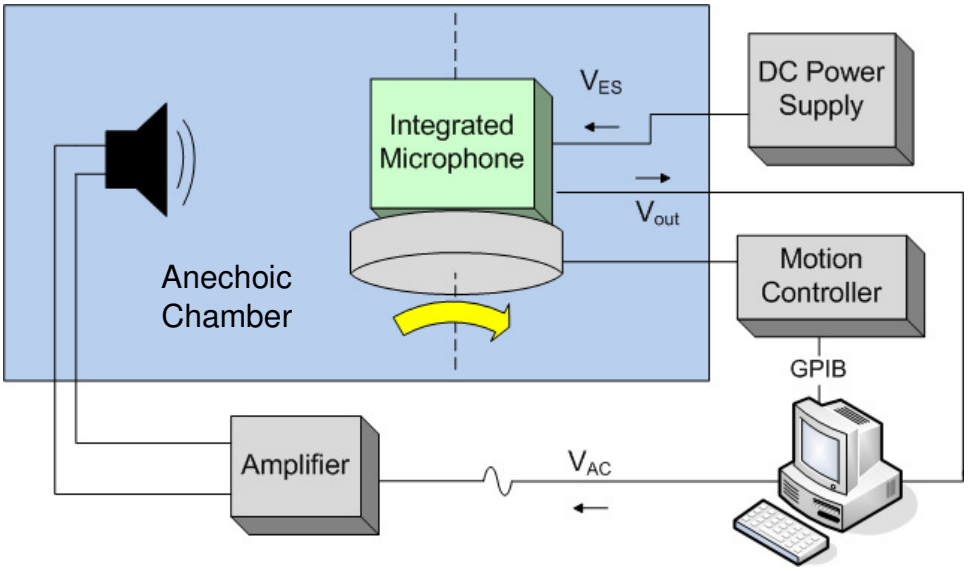

Figure 5.16 Test setup for directivity measurements

The acoustic signal is generated by driving a speaker with a pure sinusoid at a fixed amplitude and frequency. The microphone is rotated in increments using a precision rotation stage and the response is recorded at each interval. This greatly simplifies the equipment required to measure the directivity in a plane of interest. The relative signal amplitudes measured at each interval are plotted in a Spatial Directivity Pattern. Because the SDP varies with frequency, the test is repeated for several frequencies ranging from 50Hz to 5kHz. The results are shown in figures 5.17 through 5.27.

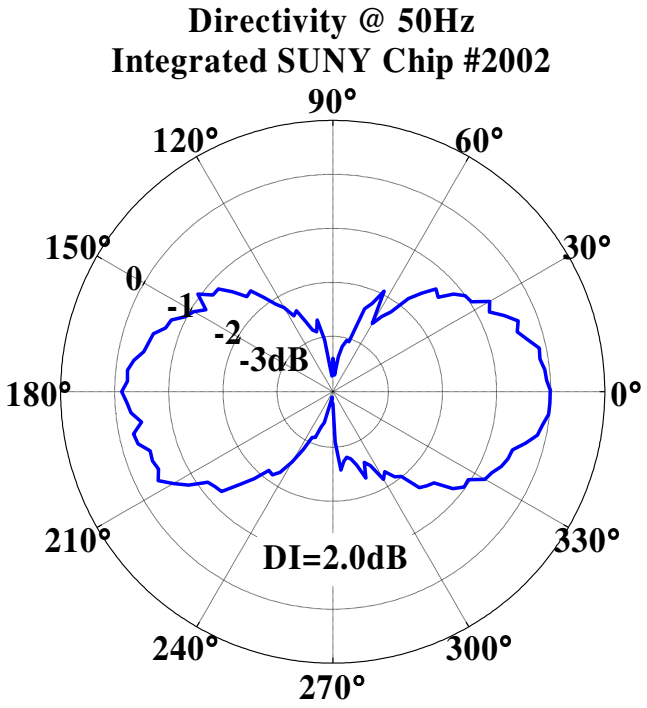

Figure 5.17 Directivity pattern of integrated hearing aid microphone @ 50Hz

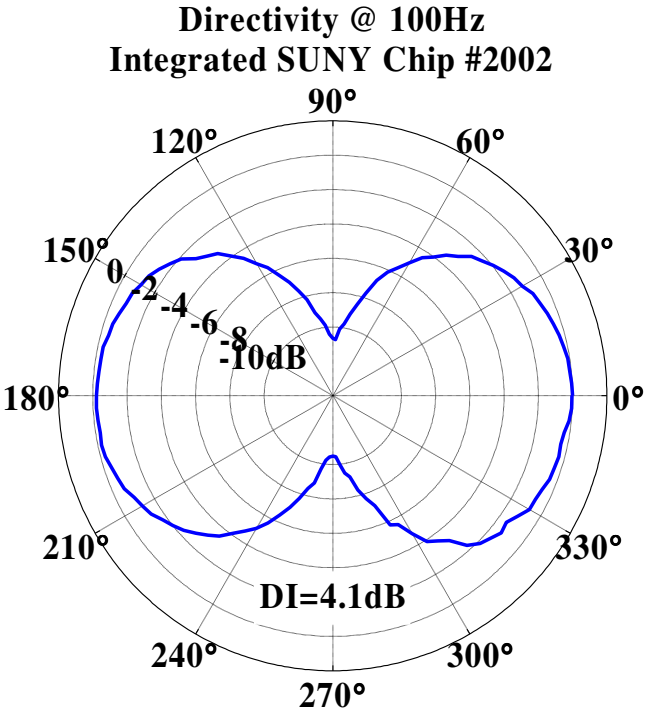

Figure 5.18 Directivity pattern of integrated hearing aid microphone @ 100Hz

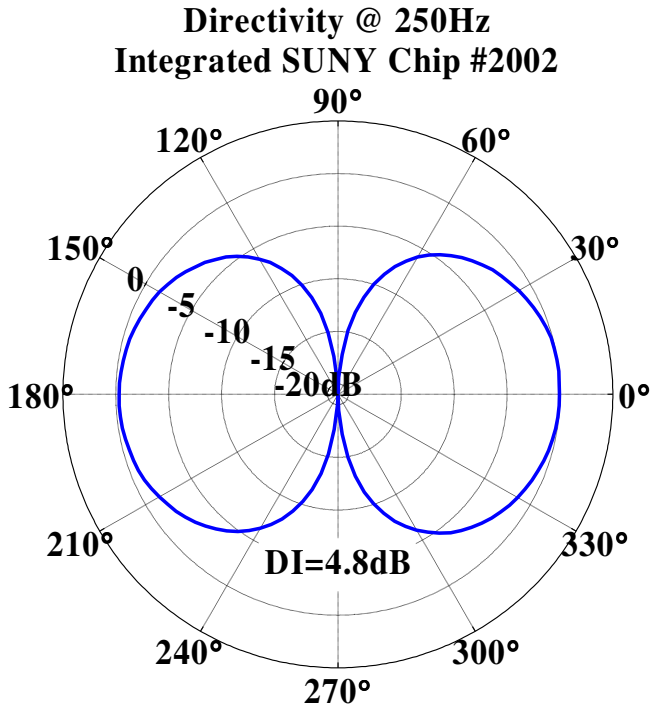

Figure 5.19 Directivity pattern of integrated hearing aid microphone @ 250Hz

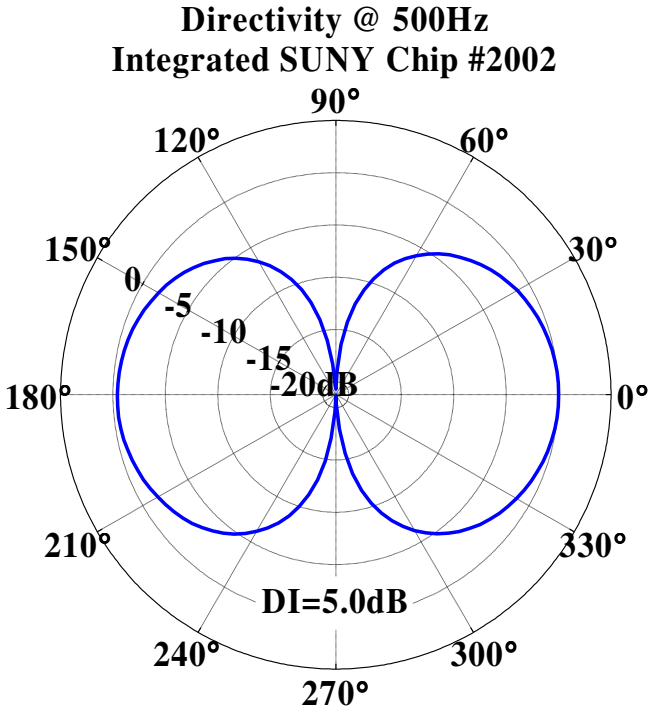

Figure 5.20 Directivity pattern of integrated hearing aid microphone @ 500Hz

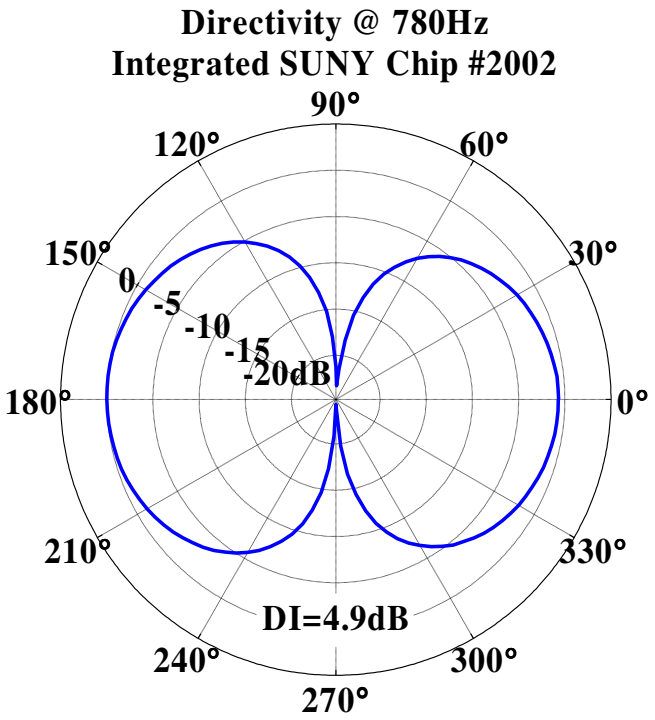

Figure 5.21 Directivity pattern of integrated hearing aid microphone @ 780Hz

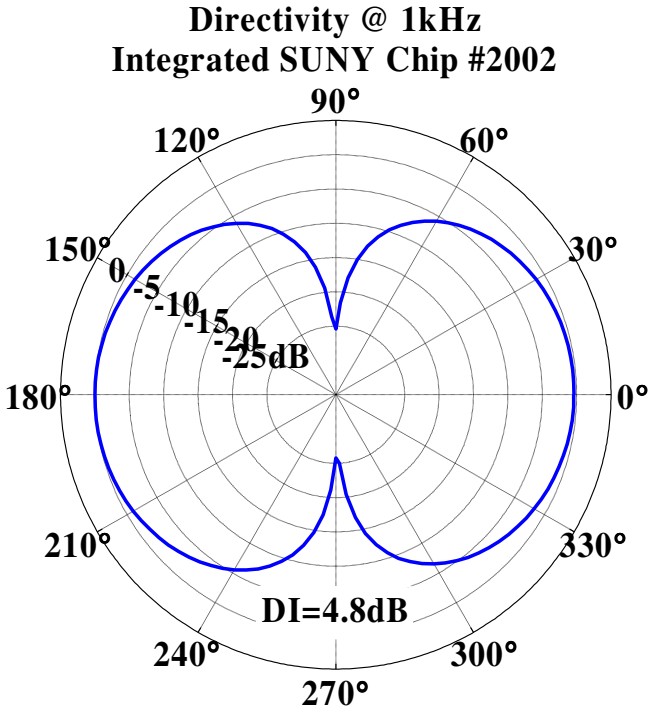

Figure 5.22 Directivity pattern of integrated hearing aid microphone @ 1kHz

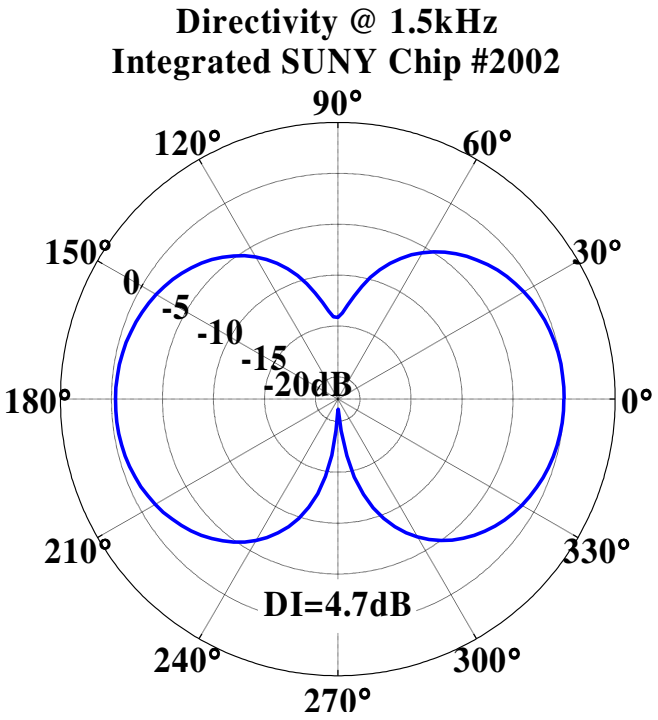

Figure 5.23 Directivity pattern of integrated hearing aid microphone @ 1.5kHz

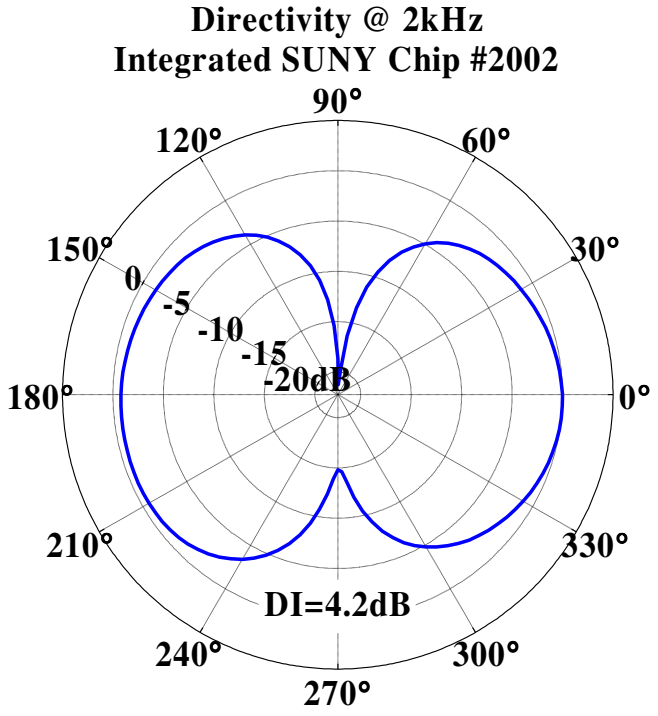

Figure 5.24 Directivity pattern of integrated hearing aid microphone @ 2kHz

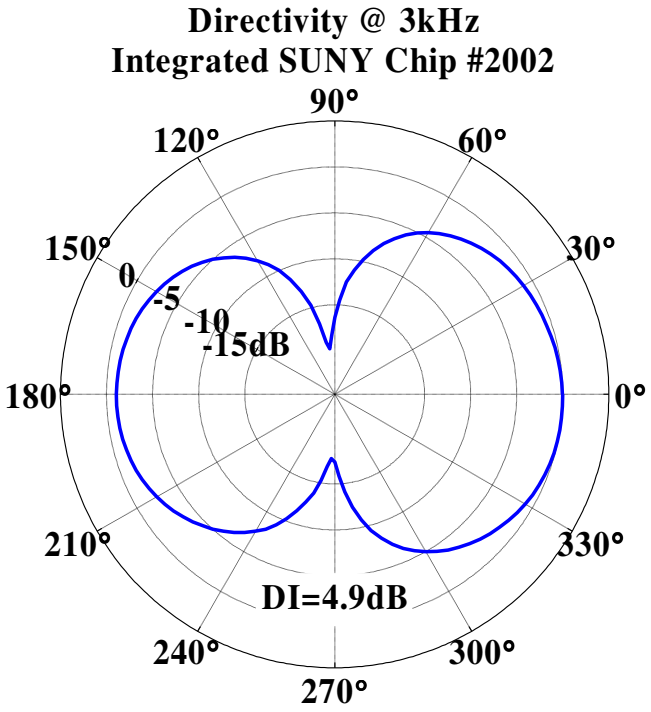

Figure 5.25 Directivity pattern of integrated hearing aid microphone @ 3kHz

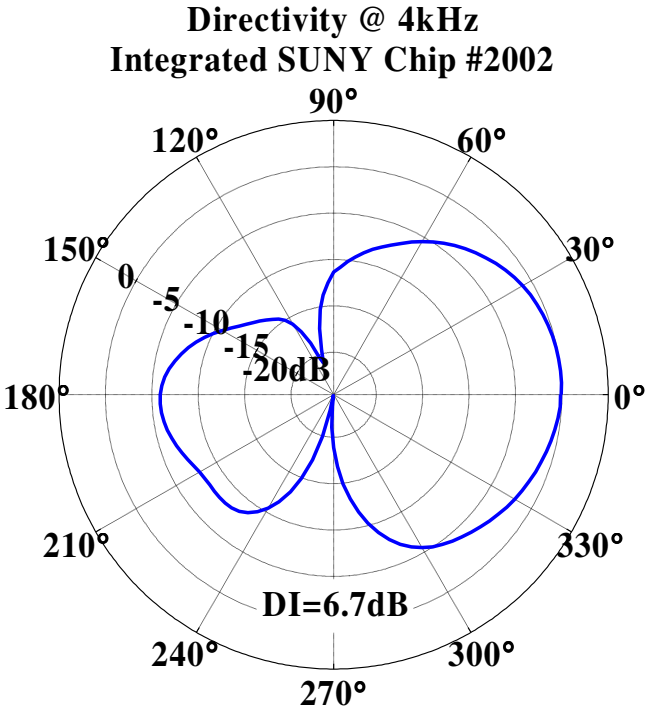

Figure 5.26 Directivity pattern of integrated hearing aid microphone @ 4kHz

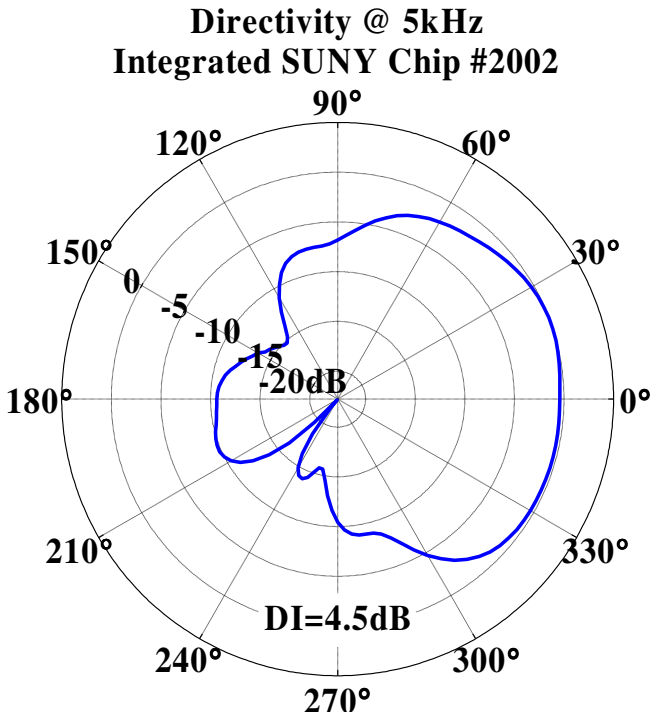

Figure 5.27 Directivity pattern of integrated hearing aid microphone @ 5kHz

The integrated hearing aid microphone exhibits excellent directivity patterns between 250Hz and 1 kHz, with directional attenuation exceeding 25dB @ 1kHz. Above this range the directivity begins to suffer as the wavelength of the audio signal approaches the size of the microphone test box, resulting in disruption of the field due to diffraction and scattering. This results in the asymmetry and deformation of the directivity patterns at higher frequencies.

For the modified free field method used in this work, the directivity index (DI) is defined in the voltage domain by equation 5.2

$$DI(f) = 10\log_{10}\left[\frac{2}{\int_{\theta=0}^{\pi}\left(\frac{V_{rms}(f,\theta)}{V_{ax}(f)}\right)^2 \sin(\theta)d\theta}\right] \tag{5.2}$$

In this expression f is the frequency of interest, θ is the angle of rotation of the microphone relative to the source, V_{rms} is the voltage output measured as a function of frequency and angle of incidence, and V_{ax} is the on-axis response (i.e. the response when θ=0). For the discrete data measured in this work, the integral in the denominator of equation 5.2 is replaced with a summation, as given by equation 5.3.

$$DI(f) = 10\log_{10}\left[\frac{2}{\sum_{m=1}^{\pi/\Delta\theta}\frac{V_{rms}^2(f,\theta_m)}{V_{ax}^2(f)}\sin(\theta_m)\Delta\theta}\right] \tag{5.3}$$

As noted in Chapter 1, the DI for an ideal dipole microphone is 4.8dB. The DI of the integrated hearing aid microphone at each measured frequency is listed in table 5.2. This data indicates that the integrated hearing aid microphone exhibits nearly ideal dipole directivity indices between 250Hz and 1.5kHz. This is a significant result for a hearing aid microphone with a noise floor of 35.9dBA.

Table 5.2 Directivity Index of integrated hearing aid microphone at various frequencies

Frequency (Hz)	Directivity Index (dB)
50	2.0
100	4.1
250	4.8
500	5.0
780	4.9
1000	4.8
1500	4.7
2000	4.2
3000	4.9
4000	6.7
5000	4.5

Discussion of Results

The electrical sensitivities and modulation efficiencies for the 1st order signals follow the trends predicted by the optical simulations presented in Chapter 3. The lowest noise SPL (and hence greatest SNR) was measured by PD2, validating the design of the hearing aid microphone package.

Hearing aids typically require a microphone with an electrical sensitivity on the order of 30mV/Pa in order to provide sufficient signal in the measurement range [2]. The sensitivity of the integrated biomimetic microphone exceeds this value for all

frequencies in the audio spectrum above 100Hz. While the shape of the acoustic response is far from ideal, the decoupled electrostatic actuation capability can be utilized to employ a force-feedback control loop in order to effectively suppress the resonances of the device and realize a flat frequency response across the audio range [35].

The directivity data was presented in units of dB as this allows direct reading of off-axis suppression. In order to compare with the directivity pattern of an ideal 1st order dipole, the directivity data can be normalized and plotted in a linear manner, as shown in figure 5.28.

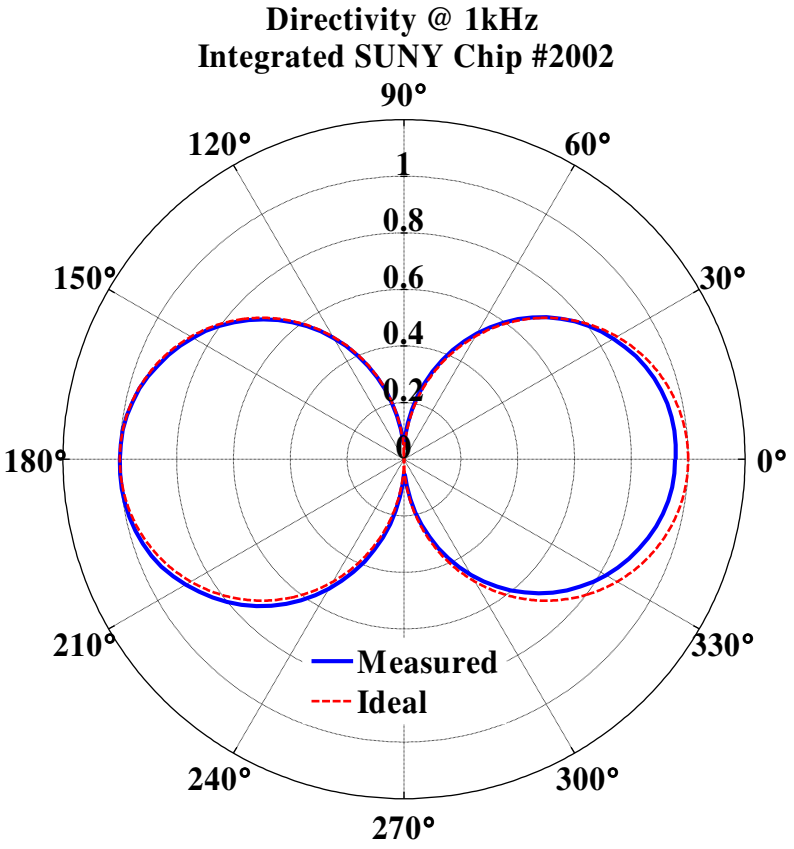

Figure 5.28 Linear directivity pattern of integrated hearing aid microphone @ 1kHz

This data shows a nearly ideal directivity pattern at 1kHz, confirming the 1st order directional response of the integrated hearing aid microphone.

The noise level is the most important selling point for hearing aid microphones [2]. The noise SPL of the integrated hearing aid microphone is 35.9dBA. Direct comparison with existing technologies requires a relative measure of SPL between directional and omnidirectional microphones. As discussed in Chapter 1, a directional response can be achieved by combining the signal from two adjacent omnidirectional microphones. While this technique achieves a directional response, differencing the signals in this way reduces the sensitivity of the device while at the same time combining the noise. Equation 5.4 calculates the effective noise spectrum that would be produced by combining the signals of two omnidirectional microphones in order to realize a directional transducer [20].

$$S_{dd}^{N}(\omega) = 2\left(\frac{c}{\omega d_0}\right)^2 S_{oo}^{N}(\omega) \tag{5.4}$$

S^{N}_{oo} is the noise spectrum of a single omnidirectional microphone, S^{N}_{dd} is the combined noise spectrum of the omnidirectional pair, ω is the frequency, d_0 is the port spacing, and c is the speed of sound in air. As an example, consider the noise spectra in figure 5.29. The pressure noise spectrum of a single omnidirectional Larson Davis ½" microphone is shown in red. This translates to a noise SPL of 16.3dBA. For the purpose of comparison, equation 5.4 is applied to the Larson Davis noise spectrum. The port spacing is set to 2mm, as this is the equivalent port spacing for the biomimetic microphone. This results in the pressure noise spectrum for the Larson Davis pair, which corresponds to a noise SPL of 49.6dBA.

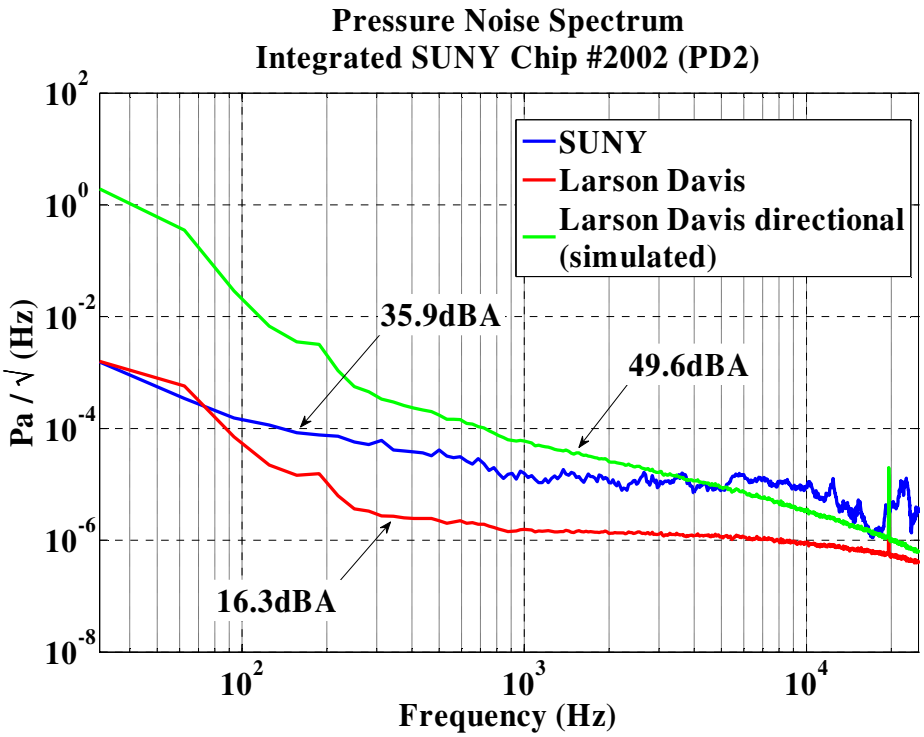

Figure 5.29 Pressure noise spectrum of integrated hearing aid microphone compared with that of capacitive microphone technology

In comparison, the integrated biomimetic microphone exhibits a noise SPL of 35.9dBA. In light of its 1st order dipole directivity patterns, the microphone developed in this work far outperforms conventional hearing aid microphone technology. This is a clear illustration the advantage of the biomimetic diaphragm structure coupled with the interferometric displacement detection architecture.

CHAPTER 6

CONCLUSIONS

The primary goal of this project was to integrate a biomimetic MEMS microphone membrane with a microscale optoelectronic detection mechanism in order to realize a low noise directional hearing aid microphone. This goal was achieved by the design, fabrication, and implementation of Multi-Chip Module optoelectronic package fabricated using high resolution SLA fabrication technology.

Characterization of the integrated microphone was described in detail, including measurements of dynamic response, sensitivity, noise floor and directivity. A displacement resolution of 3.5×10^{-13} m/√Hz was measured between 4kHz and 16kHz in an anechoic test chamber, corresponding to a dynamic range of 115dB. Using an analytical model combined with experimental data, the device was shown to be limited by thermal noise between 100Hz - 4kHz. The total noise SPL of the device is 35.9dBA. Unlike omnidirectional microphones with comparable noise levels, the device developed in this work exhibits first order dipole directivity patterns between 250Hz-1kHz, with an ideal Directivity Index of 4.8dB @ 1kHz and directional attenuation exceeding 25dB. With these results the optoelectronic package presented in this work demonstrates the viability of the integrated optical biomimetic microphone in compact, low power applications, specifically directional hearing aids.

Recommendations for Future Work

The noise SPL of the hearing aid microphone presented in this work is primarily limited by the dominance of the thermal noise of the membrane structure, the reduction of which requires modification of the mechanical design of the biomimetic membrane. Room for improvement of the optical detection architecture also exists. While the noise spectrum of the integrated biomimetic microphone approaches the shot noise limit, the full displacement sensitivity offered by the interferometric displacement architecture was not realized due to laser intensity noise related to the overlap of the diverging orders. The prototype test bed detailed in Chapter 2 implemented a collimated light source focused with lenses. This resulted in a noise SPL of 30.2dBA, which is a close match to simulated thermal noise level of 30.3dBA presented in Chapter 5. This data suggests that implementation of a microfabricated lens can potentially lead to the realization of shot-noise limited detection in the integrated biomimetic microphone.

In addition to minimizing noise, the addition of a lens would significantly improve the power efficiency of the device. One of the major constraints on a hearing aid microphone is total power consumption. These devices are typically powered by a small button cell battery supplying a voltage around 1V [2]. In order to be commercially viable the microphone must consume as little power as possible. In an optical microphone utilizing interferometric displacement detection, one of the major drains on battery power is the light source, i.e. the VCSEL. Under continuous wave operation the VCSEL consumes roughly 2mW of power. The *Light Power Efficiency* of the optical detection architecture is quantified in equation 6.1.

$$\eta_{LP} = \frac{\left(\frac{VDC}{RG}\right)}{PVCSEL} \tag{6.1}$$

In this equation V_{DC} is the DC signal offset (obtained from the optical intensity curves), R is the photodiode responsivity, G is the trans-impedance amplifier gain, and P_{VCSEL} is the VCSEL output power. Equation 6.1 calculates the percentage of the incident light power which is ultimately captured by a particular photodiode. As calculated from figure 5.3, $\eta_{LP} = 0.18\%$. This indicates that there is significant loss of light at the grating and photodiode planes. At these locations the beam spot has diverged to an area which is much larger than the footprint of both the diffraction grating and photodiodes. As a result, only a small percentage of the light emitted by the laser is ultimately converted into a usable signal and captured by the photodiode. This suggests that the optical detection architecture can function on a fraction of the power by increasing the percentage of the incident light that is captured by the photodiodes. A focused beam with a low divergence angle would minimize the light that is lost at both of these stages, significantly increasing the light power efficiency.

It must be noted, however, that the VCSEL requires a minimum current and voltage in order to operate beyond threshold. These minimum values impose a lower limit on the power consumption of the device under continuous wave operation. One way to reduce the power consumption below this limit is to drive the VCSEL with a pulsed signal. In this way, the VCSEL consumes significantly less power, based on the duty cycle at which it is driven. As long as the frequency of the pulsed signal satisfies the Nyquist criterion, the microphone can capture the desired audio signal without

aliasing. The upper limit of the audio band is 20kHz; therefore, the VCSEL must be pulsed above 40kHz in order to avoid aliasing within the audio range.

A final recommendation concerns the acoustic frequency response of the integrated hearing aid microphone. Ideally, the microphone should exhibit a flat response across the audio range. This is certainly not the case as evident from the measured data. As discussed in Chapter 5, the decoupled electrostatic actuation capability can be utilized to employ a force-feedback control loop in order to tailor the shape of frequency response of the device. This ability demonstrates yet another benefit of the optical detection architecture implemented in the integrated hearing aid microphone.

REFERENCES

[1] S. Kochkin, "MarkeTrak VII: Hearing loss population top 31 million people," *The Hearing Review,* Vol. 12, pp. 16-29, 2005.

[2] S. Bouwstra, T. Storgaard-Larsen, P. R. Scheeper, J. Ole Gullov, J. Bay, M. Mullenborg, and P. Rombach, "Silicon microphones—a Danish perspective," *J. Micromech. Microeng.,* Vol. 8, pp. 64–68, 1998.

[3] Arthur Schaub, *Digital Hearing Aids*. New York: Thieme Medical Publishers, 2008.

[4] M. Kompis and N. Diller, "Noise reduction for hearing aids: Combining directional microphones with an adaptive beamformer," *J. Acoust. Soc. Am.*, Vol. 96, 1994.

[5] S. Kochkin. "MarkeTrak VII: Customer satisfaction with hearing instruments in the digital age," *The Hearing Journal,* Vol. 58, pp. 30-43, 2005.

[6] Gary W. Elko, Flavio Pardo, Daniel Lopez, David Bishop, and Peter Gammel, "Capacitive MEMS Microphones," *Bell Labs Technical Journal,* 10(3), pp. 187–198, 2005.

[7] John Eargle. *The Microphone Book.* Oxford: Elsevier, 2004.

[8] M. J. Madou, *Fundamentals of Microfabrication: The Science of Miniaturization, 2nd ed.* Boca Raton, FL: CRC Press, 2002.

[9] M. Gayford, *Microphone Engineering Handbook.* Oxford: Focal Press, 1994.

[10] P. R. Scheeper, A. G. H. v. d. Donk, W. Olthuis, and P. Bergveld, "A review of silicon microphones," *Sensors and Actuators A*, Vol. 44, pp. 1-11, 1994.

[11] S. D. Senturia, *Microsystems Design.* New York, NY: Springer, 2001.

[12] N. Bilaniuk, "Optical microphone transduction techniques," *Applied Acoustics*, Vol. 50, pp. 35-63, 1997.

[13] Hecht, J., "Victorian experiments and optical communications," *IEEE Spectrum,* Vol. 22, pp. 69-73, 1985.

[14] N. A. Hall, *Micromachined Broadband Acoustic Transducer with Integrated Optical Displacement Detection*, Ph.D. thesis, Georgia Institute of Technology, 2004.

[15] N. A. Hall, B. Bicen, M. K. Jeelani, W. Lee, S. Qureshi, F. L. Degertekin, and M. Okandan, "Micromachined microphones with diffraction-based optical displacement detection," *The Journal of the Acoustical Society of America*, vol. 118, pp. 3000-3009, 2005.

[16] C. Garcia, *Packaging and Characterization of MEMS Optical Microphones,* M.S. Thesis, Georgia Institute of Technology, 2007.

[17] Thompson, Stephen C., "Tutorial on Microphone Technologies for Directional Hearing Aids," *The Hearing Journal*, Vol. 56, pp.14-21, 2003.

[18] Malcolm J. Crocker, *Handbook of Acoustics*. Wiley, John & Sons, Inc., 1998

[19] R. N. Miles, D. Robert, and R. R. Hoy, "Mechanically coupled ears for directional hearing in the parasitoid fly ormia ochracea," *The Journal of the Acoustical Society of America*, Vol. 98, pp. 3059-3070, 1995.

[20] R. N. Miles, Q. Su, W. Cui, M. Shetye, F. L. Degertekin, B. Bicen, C. Garcia, S. Jones, and N. Hall. "A low-noise differential microphone inspired by the ears of the parasitoid fly Ormia ochracea," *Journal of the Acoustical Society of America, J. Acoust. Soc. Am.*, Vol. 125**,** pp. 2013-2026, 2009

[21] S. Mohan, M.E. Lockwood, M.L. Kramer, and D.L. Jones. "Localization of multiple acoustic sources with small arrays using a coherence test," *J. Acoust. Soc. Am.,* Vol. 123, pp. 2136–2147, 2008.

[22] Dittberner, Andrew B. "Quantifying Microphone Directivity," *The Hearing Journal*, Vol. 56, pp.22-29, 2003.

[23] Brinkman K, Goydke H: Random incidence and diffuse field calibration. In Wong GSK, Embleton TFW, eds.,*AIP Handbook of Condenser Microphones: Theory, Calibration and Measurements.* New York: American Institute of Physics, 1995: 120-144.

[24] Beranek LL. *Acoustics*. New York: McGraw-Hill Electrical and Electronic Engineering Series, McGraw Hill, 1954.

[25] ULN Series Diode Laser Module, Coherent Photonics Group, Auburn, CA

[26] VCSEL Model AVAP-850SM, Avalon Photonics Ltd., Zurich, Switzerland

[27] VCSEL Model no. VCC85A1G-IS, Lasermate Group Inc., Pomona, CA, 91768.

[28] K. Lizuka, *Engineering Optics Second Edition.* Berlin, Germany: Springer, 1987.

[29] Goodman, *Introduction to Fourier Optics*, 1988.

[30] Theodore R. Kucklick, *The Medical Device R&D Handbook.* Taylor & Francis, Inc., 2005.

[31] Andreas Gebhardt, *Rapid Prototyping.* Hanser-Gardner Publications, 2003.

[32] Kenneth G Cooper, *Rapid Prototyping Technology.* Taylor & Francis, Inc., 2001.

[33] RenShape™ SL5510, Vantico A&T US, Inc., Lansing, MI 48823.

[34] SLA Viper, 3D Systems Corporation, Rock Hill, SC.

[35] N. A. Hall, M. Okandan, R. Littress, D. Serkland, G. Keeler, K. Peterson, B. Bicen, C. Garcia, and F. L. Degertekin, "Micromachined accelerometers with optical read-out and electrostatic actuation for self-tuning, self dynamic characterization, and force-feedback modalities*," Journal of Microelectromechanical Systems*, Vol.17, pp. 37-44, 2008.